

THIS REPORT HAS BEEN DELIMITED
AND CLEARED FOR PUBLIC RELEASE
UNDER DOD DIRECTIVE 5200.20 AND
NO RESTRICTIONS ARE IMPOSED UPON
ITS USE AND DISCLOSURE.

DISTRIBUTION STATEMENT A

APPROVED FOR PUBLIC RELEASE;
DISTRIBUTION UNLIMITED.

UNCLASSIFIED

AD **143 261**

*Reproduced
by the*

ARMED SERVICES TECHNICAL INFORMATION AGENCY
ARLINGTON HALL STATION
ARLINGTON 12, VIRGINIA



UNCLASSIFIED

NOTICE: When government or other drawings, specifications or other data are used for any purpose other than in connection with a definitely related government procurement operation, the U. S. Government thereby incurs no responsibility, nor any obligation whatsoever; and the fact that the Government may have formulated, furnished, or in any way supplied the said drawings, specifications, or other data is not to be regarded by implication or otherwise as in any manner licensing the holder or any other person or corporation, or conveying any rights or permission to manufacture, use or sell any patented invention that may in any way be related thereto.

Dr. Littleton

143261

FILE COPY
LOAN ONLY

OSRD 6246
NDRC A-368

NAVORD REPORT 9-47

COPY NO.

FILE COPY

PHOTOGRAPHY OF UNDERWATER EXPLOSIONS, I.



This Document
Reproduced From
Best Available Copy

AD-143261

A BUREAU OF ORDNANCE PUBLICATION

24 MARCH 1947

NAVY DEPARTMENT
BUREAU OF ORDNANCE
WASHINGTON, D.C.

Vice Admiral G.F. Hussey, Jr., USN
Chief of the Bureau of Ordnance

Captain K.H. Noble, USN
Assistant Chief of Bureau for
Research

Captain S.H. Crittenden, Jr., USN
Ammunition and Explosives

Dr. Stephen Brunauer
High Explosives and
Amphibious Munitions

NAVORD Report 9-47
(OSRD 6246; NDRC A-368)

PHOTOGRAPHY OF UNDERWATER EXPLOSIONS, I

by

J.E. Eldridge, P.M. Fye, and R.W. Spitzer

Investigation Group: J.E. Eldridge, P.M. Fye, R.R. Halverson,
J.D. Klicker, P. Newmark, E.L. Patterson, R.S. Price, and
R.W. Spitzer

The Underwater Explosives Research Laboratory
Woods Hole Oceanographic Institution
Woods Hole, Massachusetts

24 MARCH 1947

NAVY DEPARTMENT
BUREAU OF ORDNANCE
WASHINGTON, D.C.

24 March 1947

NAVORD Report 9-47

PHOTOGRAPHY OF UNDERWATER EXPLOSIONS, I

1. This report discusses in detail methods and apparatus used in obtaining pictures of underwater explosions in the open ocean where the size of charge is limited chiefly by the transparency of the water rather than by the strength of a tank or the ruggedness of the apparatus.

2. The work described in this report was begun under OSRD Contract OER-569 with the Woods Hole Oceanographic Institution and pertains to the project designated by the Navy Department Liaison Officer as NO-223. It was completed as part of Task A assigned under Bureau of Ordnance Contract NORD-9500.

3. The interpretations are those of the authors and do not necessarily represent the views of the Bureau of Ordnance.

4. This report does not supersede any existing publication.

G. F. RUSSEY, Jr.
Vice Admiral, U.S. Navy
Chief of the Bureau of Ordnance

K. H. Noble
Captain, U. S. Navy
Assistant Chief of Bureau
for Research.
Acting.

Table of Contents

<u>Abstract</u>		<u>Page</u>
<u>Section</u>		
I. INTRODUCTION		1
II. EXPERIMENTAL METHODS AND EQUIPMENT		1
1. Methods of flash photography		1
(a) General information		1
(b) Water transparency		1
(c) Cameras for flash photography		2
(i) Argus C-3		2
(ii) Kodak "35"		2
(iii) UERL camera		2
(iv) Automatic photography		2
(d) Light sources		2
(j) Glass enclosed flash charges for depths down to 20 feet		7
(ii) Conical flash charges for depths down to 10 feet		7
(iii) Flash charges for depths down to 600 feet		10
(iv) Other sources		10
(e) Underwater equipment		10
(f) Firing devices		10
2. Methods of motion picture photography		10
(a) Cameras for motion picture photography		10
(i) Eastman high speed camera		10
(ii) Jerome camera		15
(iii) Victor camera		15
(b) Associated equipment for underwater photography		15
(i) Underwater gear		15
(c) Light sources		15
(i) Photoflash lamps		15
(ii) Mercury arc		15
(d) Timers		15
(e) Power supply for cameras		15
III. RESULTS OF EXPERIMENTS		20
1. Cavitation		20
(a) Minimum tension necessary to cause cavitation		20
(b) Criterion for cavitation in front of steel diaphragm		20
(c) Cavitation from objects other than plane surfaces		26
(d) Disappearance of cavitation		26
(e) Cavitation caused by oblique reflection of shock waves from air-water interfaces		26
2. Investigation of the effect of shape of charge and point of detonation on shock wave and bubble		35

Table of Contents (Continued)

	Page
3. Pressure and time-constant measurements of shock waves by optical distortion	43
(a) Spherical shock wave; charge not on the optical axis; charge in grid plane	43
(i) Peak pressure	43
(ii) Time-constants	47
(iii) Summary and remarks	48
(b) Spherical shock wave; charge on the optical axis; charge in grid plane	48
(c) Non-spherical shock wave; charge on the optical axis; charge in grid plane	48
(d) Spherical shock wave; charge on the optical axis; charge in front of grid plane	48
4. Cylinder damage	51
(a) Introduction	51
(b) Still pictures	51
(c) Slow speed movies	51
(d) High speed movies	51
5. Miscellaneous experiments	51
(a) Mach effect	51
(b) Shock wave from 300 lb. charge	51
(c) Pressure of shock wave determined from shock wave velocity	57
(d) Experiments showing that the apparent position of the shock wave coincides closely with its actual position	57
(e) Luminosity of charges exploded underwater	60

APPENDIX

I. Theory of pressure in front of an air-backed free plate accelerated by a shock wave	61
II. Theory of peak pressure and time constant determination for shock waves by the method of optical distortion	66
1. Grid in plane of center of charge; charge off to the side; spherical shock wave	66
(a) Peak pressure determination	66
(i) Technique of measurement	72
(b) Calculation procedure for time constant (exponential decay constant with distance behind front)	72
(c) Calculation procedure for time constant (exponential decay constant with time behind front)	74
(d) Possible errors	76
(e) Sample calculation of time constant	77
2. Grid in same plane with charge; charge directly in front of camera; spherical shock wave	80
3. Grid in same plane with charge; charge directly in front of camera; non-spherical shock wave	82

Table of Contents (Continued)

	Page
4. Grid behind shock wave; charge directly in front of camera; spherical shock wave	84
III. Circuit diagrams of camera timers	87
1. Timer for high speed camera	87
2. Timer for Jerome camera	87
IV. Gaskets and stuffing boxes for camera cases	90

List of Figures

<u>Figure</u>	<u>Page</u>
1. Argus C-3 camera and case	3
2. Kodak "35" and case	4
3. Kodak "35" in case	5
4. Modified Kodak "35"	6
5. Various types of flash charges prepared at UERL	8
6. Plaster of paris molds for casting spherical pentolite flash charges	9
7. Glass-enclosed spherical flash charge; a cross-sectional view	9
8. Conical pentolite flash charge; a cross-sectional view	9
9. Flash charge for deep water; a cross-sectional view	11
10. Diagram of apparatus for underwater photography	11
11. Steps in lowering equipment for single shot photograph of charge damaging diaphragm	12
12. Eastman high speed camera	13
13. High speed camera and "Explosion Proof" case	14
14. Jerome camera showing shock mounts	16
15. Rig for high speed photography of cylinders	17
16. Side elevation of apparatus used for photographing cylinder	18
17. Firing circuit diagram	18
18. Rotating commutator switch for firing photoflash lamps in sequence	19
19 - 22. Cavitation produced by weak shock waves	21
23 - 28. Cavitation from circular diaphragms fixed at the edges	22
29. Target simulating free plate	23
30 - 33. Cavitation from "free" plates	25
34 - 35. Cavitation about collapsing cylinders	28
36. Piezoelectric gauge	28
37. Momentum Gauge	28
38. Steel Block	28
39 - 43. Spontaneous disappearance of cavitation at various times after impact of shock wave	29
44 - 49. Destruction of cavitation by shock waves	30
50. Sketch showing experimental arrangement for Figs. 51-56	31
51 - 56. Oblique reflection of shock waves from water-air interface (6 in. diameter)	32
57 - 60. Cavitation produced by oblique reflection of shock waves from water-air interfaces	34
61 - 64. Schematic diagrams of Figs. 57, 58, 59, and 60	34
65 - 67. Spheres, 2 5/8 in. diam., detonated at center	36
68 - 73. Cones, 3 1/2 in. equilateral, detonated at center	36
74 - 80. Cones, 3 1/2 in. equilateral	37
74 - 80. Cylinders, 2 1/2 in. diam., 2 1/2 in. long	38
81 - 86. Cylinders, 1 3/4 in. diam., 3 1/2 in. long	39
87 - 93. Cylinders, 1 7/16 in. diam., 5 7/8 in. long	40
94 - 100. Cylinders, 1 1/8 in. diam., 9 in. long	41
101 - 104. Miscellaneous photographs	42
105. Bubble radius vs. shock-wave radius for 1/2 lb. cast pentolite (spherical charge)	44
106. Ratios of long axis to short axis of shock waves from asymmetric cylinders vs. shock-wave radius (in charge radii) for spherical charge of same weight and after same time	44
107. Typical example of optical distortion photograph. Film 418 - 250 gm tetryl at 14.9 in.	46
108. P_{av} vs. $ R - r_{av}$ (250 gm tetryl at 14.9 in.)	45
109. P_{av} vs. $ R - r_{av}$ (250 gm tetryl at 14.4 in.)	45
110. P_{av} vs. $ R - r_{av}$ (250 gm tetryl at 14.4 in.)	45
111. P_{av} vs. $ R - r_{av}$ for shock waves produced by two charges of ca. 364 gm TNT at a value of R of 16 in.	49

List of Figures (Continued)

<u>Figure</u>		
	<u>Page</u>	
112. Spherical shock wave; charge on the optical axis; charge in grid plane	50	
113. Spherical shock wave; charge on the optical axis; charge in front of grid plane	50	
114A - 116B Damage to cylinders before and after calculated time of bubble pulse	52	
117. Cylinder No. SD - 47-29C	53	
118. Schematic view, from camera position, of arrangement for Fig. 123	54	
119 - 122. Intersecting shock waves	55	
123. Shock wave from 300 lb. charge 65 ft. from camera	56	
124. Shock wave photographed at two positions by double exposure technique	56	
125.	57	
126.	58	
127.	58	
128.	58	
129 - 130. Photographs from which agreement between true and apparent shock-wave positions is obtained	59	
131. Pressure before accelerated free plate ($\beta = 83$)	62	
132. Pressure before accelerated free plate ($\beta = 4$)	64	
133. Experimental arrangement for optical distortion study	67	
134. Plan view of "Optical Plane"	69	
135. ϕ vs ψ obtained by integration beyond the point of total reflection	79	
136. Second experimental arrangement for determination of peak pressure by optical distortion	81	
137. Third experimental arrangement for determination of peak pressure by optical distortion	83	
138. Fourth experimental arrangement for determination of peak pressure by optical distortion	85	
139. Timer for high-speed camera	88	
140. Neon bulb timer for Jerome camera	89	
141. Stuffing box for insulated lead-in	91	
142. Single wire lead-in	91	

List of Tables

<u>Table</u>		<u>Page</u>
I.	Cavitation data for steel plates in UERL diaphragm gage	24
II.	Summary of results of studies of cavitation from simulated free plates	27
III.	Experimental conditions applying to the photographs of Figs. 39 - 49	27
IV.	Data of experiments on oblique reflection of shock waves from water-air interfaces	31
V.	Data of experiments on oblique reflection of shock waves from 20 in. by 10 in. water-air interface, and from ocean surface	33
VI.	Results in the evaluation of time constant	47
VII.	Coefficients of a and b in $n(p) = n_0 + ap - bp^2$ for pure water	71
VIII.	Constants necessary for Eq. (II-15)	77
IX.	Results of integration for ϕ as a function of ψ . Value of ϕ_g as obtained in calculation for p_{av} is 0.4078 radians (point 22, film 536)	78
X.	Results of integration for ϕ beyond point of total reflection. Value of ϕ_g as obtained in calculation for p_{av} is 0.4078 radians (point 22, film 536)	78
XI.	Results in the evaluation of time constant	80

Reproduced From
Best Available Copy

NOTATION OF MAJOR SYMBOLS

		<u>Page*</u>
a and b	pressure coefficients of index of refraction for water	70
c	velocity of sound in water	21
D _r	a distance $r' - r$	47
m	mass per unit area of the plate, $\rho_s a$	21
n _{av}	average index of refraction of that section of the shock wave being investigated	43
n _o	index of refraction of sea water at zero pressure	68
p	pressure at a distance x and at a time t	20
p _{av}	average pressure of that section of the shock wave being investigated	43
p _o	peak pressure of original shock front	20
p/p _o		20
r	true radial distance from center of charge to intersection of a pair of grid lines in the optical distortion discussion, also	47
x	radial distance from center of plate to diffracted shock front in cavitation theory	63
r'	apparent radial distance from center of charge to intersection of a pair of grid lines	47
r _{av}	an average radius vector $\frac{ R + (r' - D_r)}{2}$	43
r _b	radius of bubble or particle	20
R	inside radius of pipe and/or radius of the diaphragm (or "plate")	21
R	shock wave radius	43
R _c	radius of cavitation region	21
R _o	outside radius of pipe	21
R _p	radius of steel plate	21
σ	interfacial tension between water and the particles	20
t	time measured from the time the original wave strikes the plate	61
t _c	time corresponding to x _c (calculated)	21
t _s	interval of time between impact of shock wave on plate and time of photograph	26
T	t/θ	63
u	instantaneous velocity of the plate	61

*Page where symbol is first used

NOTATION OF MAJOR SYMBOLS (Continued)

		<u>Page</u>
x	the distance of any point measured positively out into the water from the initial position of the plate	61
x_c	farthest perpendicular distance of cavitation from plate	21
\bar{x}	$x/c\theta$, i.e. distance in units of $c\theta$	20
\bar{x}_c	$x_c/c\theta$	21
α	weight-distance exponent for peak pressure	75
α	$P_{max} = \text{constant} \propto (W^{1/3}/R)^{\alpha}$	75
β	θ/θ_1 , $c\theta/m$	21
θ	time constant of shock wave	21
θ_c	cavitation time	21
θ_r	exponential decay constant of shock wave with respect to distance	47
θ_t	exponential decay constant of shock wave with respect to time	47
θ_1	$m/\rho c$	21
ν	n_{av}/n_0	68
ρ	density of water	21
τ	interval of time between impact of shock wave on plate and beginning of diffracted shock wave from the edge	63

I. INTRODUCTION

Interesting photographs of underwater explosions in model tanks have been obtained by many investigators. Their experiments suffered almost universally from the drawback that it was impossible to shoot charges larger than a gram or even a tenth of a gram. A technique has been developed at UERL of shooting in the open ocean so that the charge size is limited essentially only by the transparency of the water rather than by the strength of tank.

This report discusses in detail the methods and apparatus used in obtaining the pictures and the results of some two years of experimentation. It indicates the usefulness of photographic techniques for studying underwater explosions.

II. EXPERIMENTAL METHODS AND EQUIPMENT

Two main types of picture have been taken; the flash photograph, in which a single picture of approximately one microsecond exposure was obtained, and the motion picture, which usually gave three or four to several hundred pictures in a single experiment. These latter pictures were taken at speeds up to 2500 per second and corresponding exposures down to 100 microseconds. The two methods will be taken up in detail.

1. Methods of flash photography

(a) General information. -- In taking short exposures of rapidly changing phenomena, the shutter of the still camera was opened, the explosion initiated, a short duration flash of light emitted, and the shutter closed. During the winter months, it was found possible to work in daylight by actuating the instantaneous shutter mechanism, set at 1/100 second, with a solenoid and synchronizing the explosion electrically. When the sun was brighter, however, this method caused a general fogging even at 1/200 second, and it was found necessary to work at night. This simplified the problem of synchronization inasmuch as it was possible to set the shutter on bulb, open it with the solenoid, fire the charge, and close the shutter.

In experiments in which it was necessary to "stop" shock waves, the light source was an explosive flash charge (Section II, 1, (d)). The delay between the time of detonation of the subject charge and the flash charge was obtained by the proper length of Ensign-Bickford Primacord whose detonation velocity is 0.248 inches per microsecond.

It is possible to obtain multiple exposures on a single plate by firing several flash charges in sequence, using primacord timing.

When extreme speed was not necessary, the flash charge was replaced by a photo-flash bulb or Eastman Kodatron Speedlamp.

(b) Water transparency. -- One of the important variables in underwater photography in the open sea (near land at least) is the transparency of the water. Not only does the total amount of transmitted light from a constant light source decrease at lower transparency, but, since the lower transmission is due to turbidity, image sharpness decreases even if the proper exposure is made. To take this into account, a crude transparency measure is made by dropping a white disk eight inches in diameter through the water until it disappears from view. The depth of this disappearance is recorded as the "Secchi disk reading." ^{1/} As a rough rule of thumb, it may be stated that fairly good pictures can be taken with object-to-camera distances up to half the Secchi disk reading.

^{1/} Progress Report on Underwater Photography, by D.E. Kirkpatrick, J.L. Worzel, M. Ewing, NDRC Section C-4 (Division 6.1), May 4, 1942.

For most single flash photographs, Eastman Contrast Process Ortho film was used and developed in D-11. Typical lens openings with a 250 gm explosive flash charge at 8 ft. from the camera varied from f/3.5 to f/8 depending on water conditions.

(c) Cameras for flash photography. -- A variety of cameras were used for flash photography with approximately equal success. In order to keep the size of the equipment at a minimum, 35 mm still cameras were used.

(i) Argus C-3. Figure 1 shows the Argus C-3 camera and its water and explosion-proof case. This camera has an internal synchronizer which was sometimes used to set off explosions when the shutter was at its maximum opening. The case was constructed from 6 1/2 in. O.D. by 3/4 in. thick steel pipe and the window is of 1 in. thick "tempered" glass having a 2 1/8 in. diameter for the unsupported area. The case and window have successfully withstood the explosion of a 300 pound charge 50 ft. away, both charge and camera case being at a depth of 40 ft.

(ii) Kodak "35". Figures 2 and 3 show a Kodak "35" and case. This case which was made from a pipe coupling, has also survived the explosion of a 300 pound charge at 50 ft. The camera was later modified as shown in Figure 4 which shows a much smaller homemade camera using the lens and shutter of the Kodak 35. A smaller case would obviously have been built for this camera.

(iii) UERL camera. In the early stages of this work it was considered that commercial cameras might not be rugged enough for the work we were doing, and a camera with laboratory designation "Brute" was constructed. The "Brute" camera consisted merely of a solid brass cylinder with a heavy spring-driven rotary shutter, a hole for the lens, and another for the film. The camera also contained a "foolproof" synchronizer for firing the charge which consisted of a contact made by the shutter at any desired time in its travel. By using an SSS seismographic cap (No. 3) which explodes within a millisecond of the time the circuit is closed, the synchronizer could be set to close the circuit when the shutter was barely opened and the timing would then automatically be right.

Subsequent experience showed that the commercial shutters were sufficiently rugged so long as they were not immersed in sea water, and the "Brute" camera was rarely used.

The cameras were all mounted on rubber as a matter of principle.

(iv) Automatic photography. One photograph was obtained by means of an automatic rig. A charge was detonated which activated a pressure switch. The pressure switch closed a solenoid circuit which tripped the camera shutter. As the shutter opened, a synchronizing switch fired a cap in the flash charge. The battery required was enclosed in the camera case. The resulting photographic image is not reproduced. This method can be used in experiments in which external connections with the camera are undesirable or impossible.

(d) Light sources. -- Still close-up photography of explosion phenomena requires exposures of the order of a μ sec and a light source of about a million candle-power. A satisfactory source of light was developed by the Explosives Research Laboratory at Bruceton, Pennsylvania, utilizing a spherical cast explosive charge of pentolite mounted concentrically in a round bottom glass flask; the space between the charge and flask being filled with argon at atmospheric pressure. Duration and intensity of the light increased respectively with the thickness and area of the argon layer.

2/ The Flash Photography of Detonating Explosives to May 1, 1943, Explosives Research Laboratory, Bruceton, OSRD Report 1488.

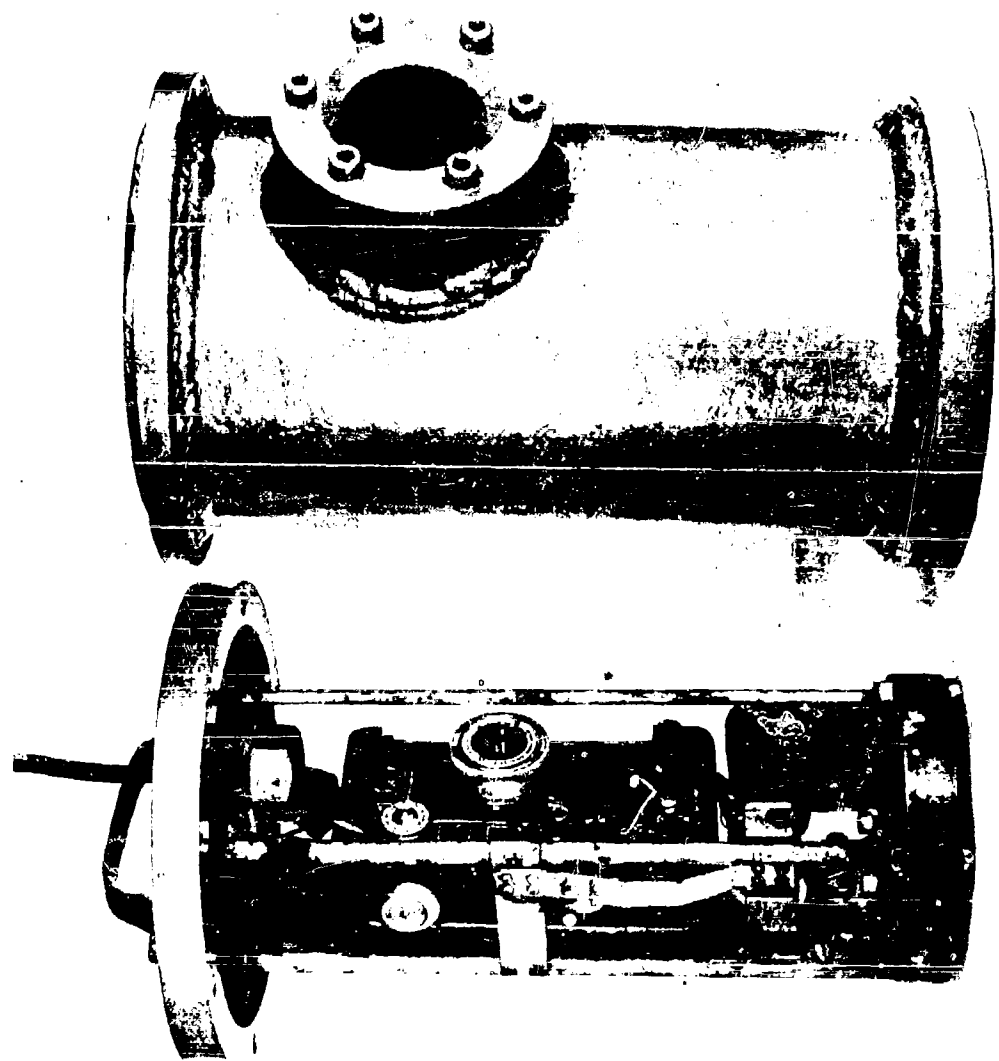


FIG. 1. Argus C-3 camera and case.

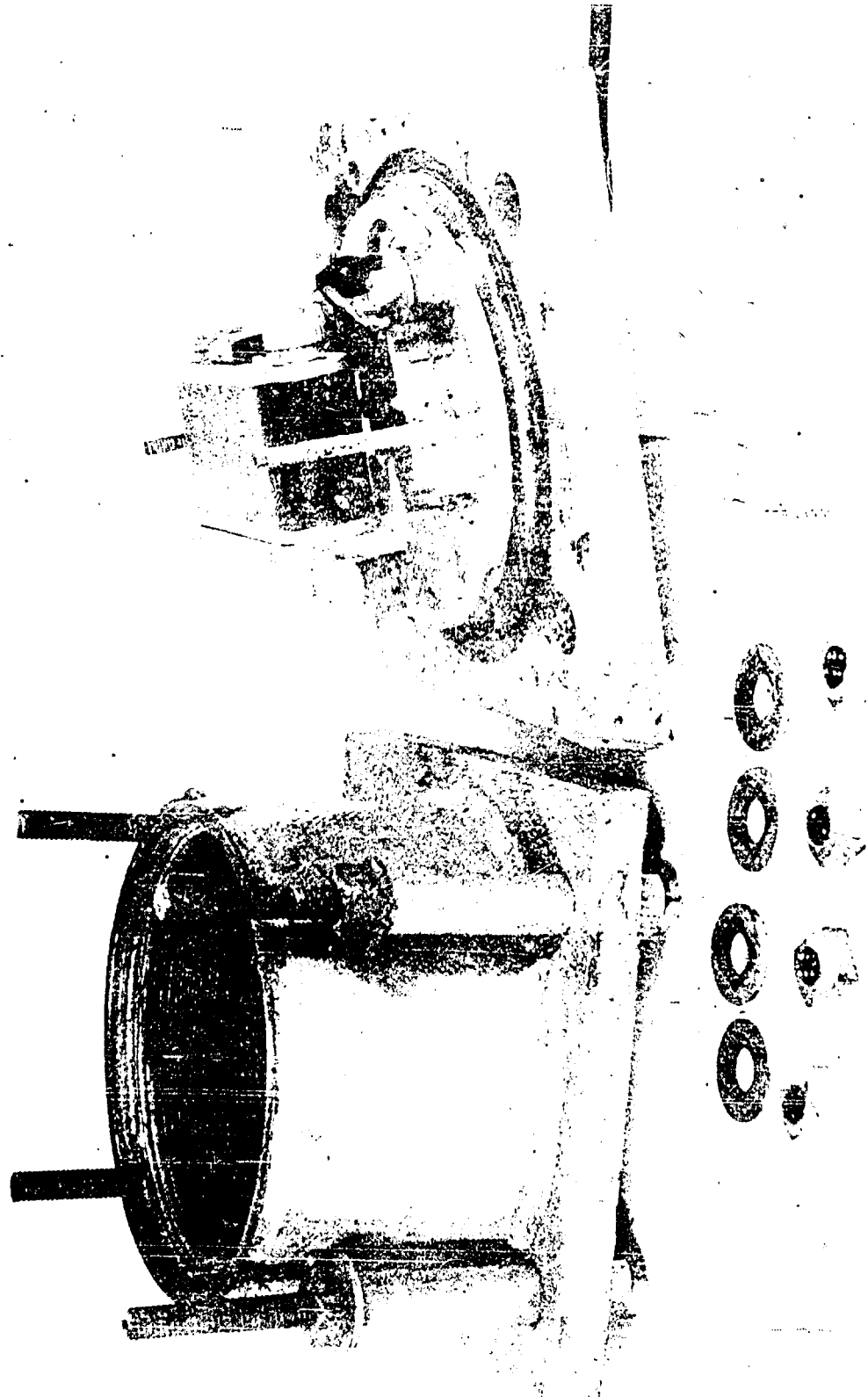


FIG. 2. Kodak "35" and case.

15518

This Document
Reproduced From
Best Available Copy

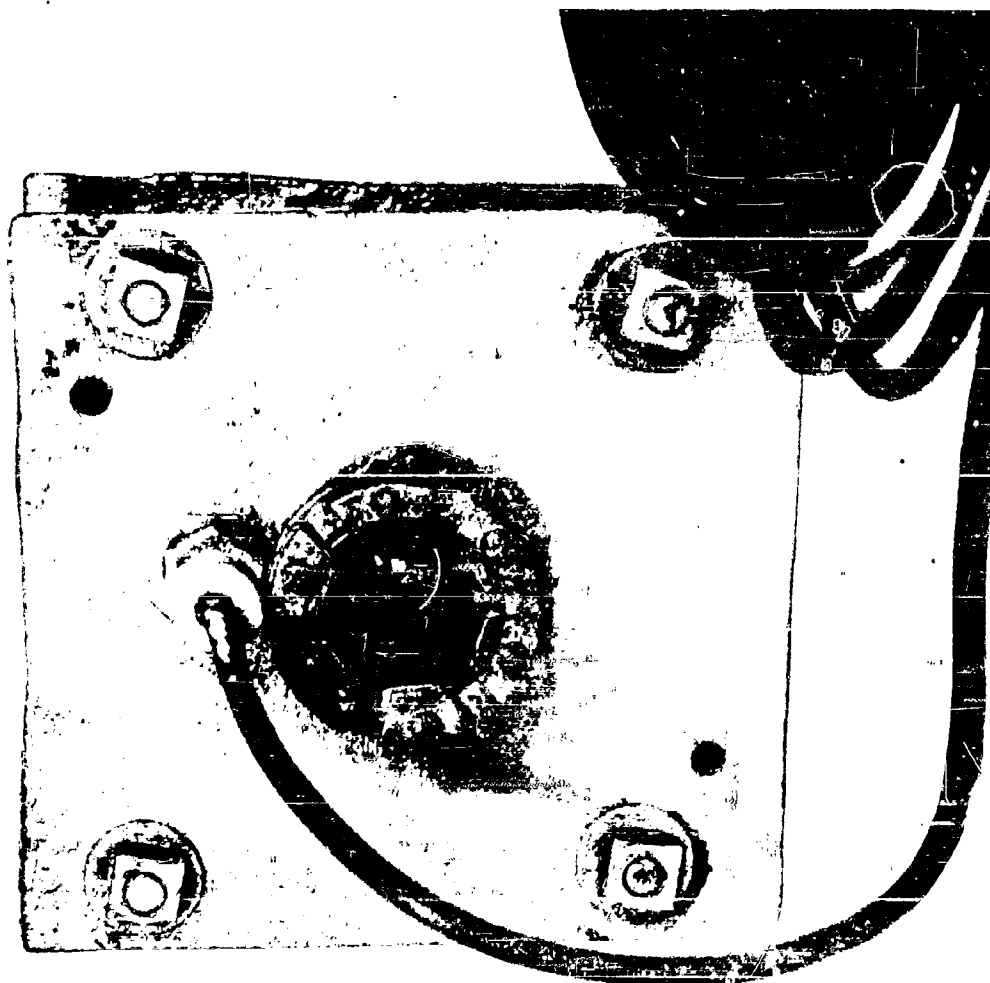


FIG. 3. Zoddak "35" in case.

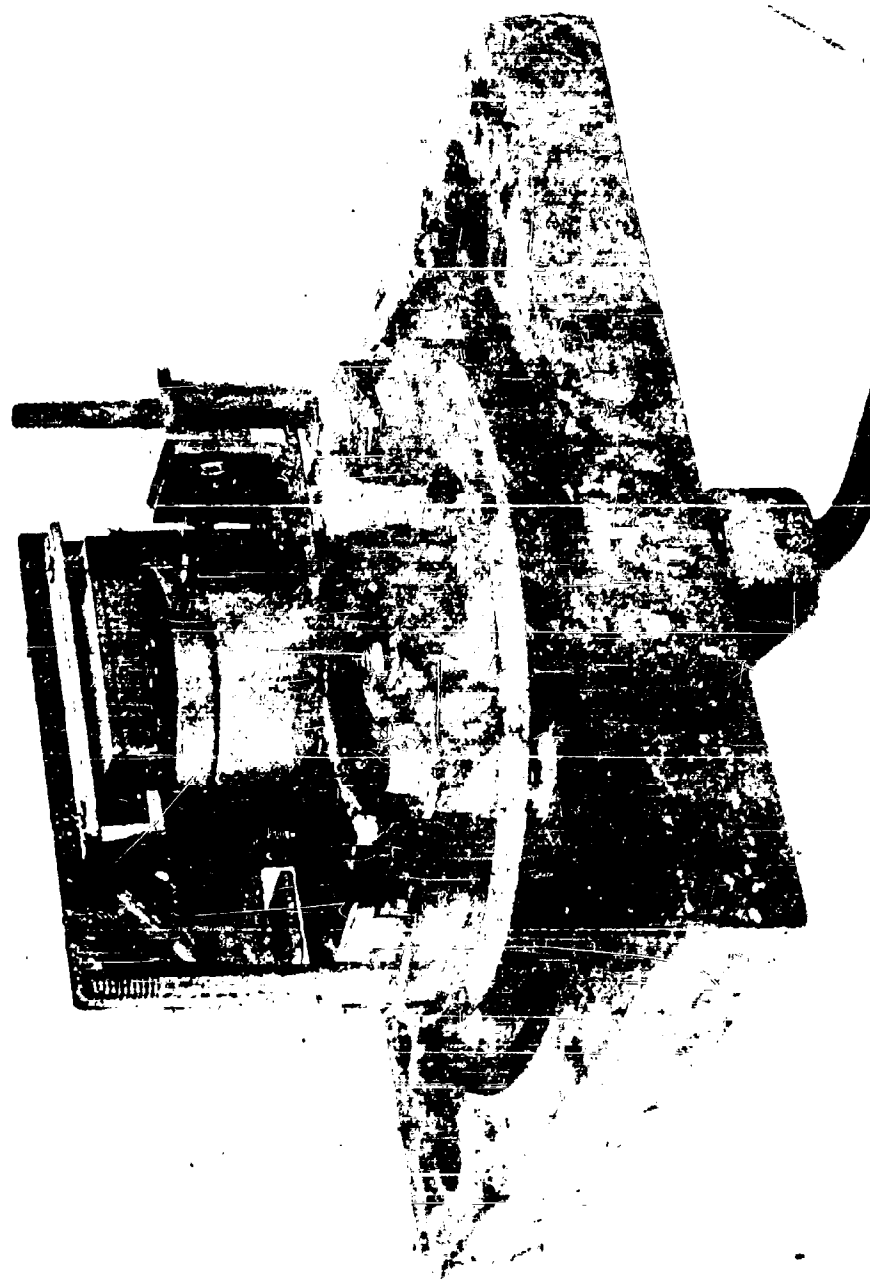


Fig. 4. Modified Kodak "35".

Argon-surrounded flash charges were adapted at UERL ^{3/} for use underwater and proved satisfactory. By using conical rather than spherical charges it was possible to produce a given amount of useful light with less explosive. The amount of light emitted by the charges was about halved if the gas layer was air instead of argon. Tests were conducted with charges coated with mercurous chloride and sodium chloride (because of their emission spectra), but the results were erratic. The various types of flash charge prepared at UERL are illustrated in Figure 5.

(i) Glass enclosed flash charges for depths down to 20 feet. Since this type of flash charge was used most, its fabrication will be discussed in some detail. A primacord fuze is cut to the desired length and one end rolled tightly in a $2 \times 2 \times 1/32$ in. sheet of lead with $1/8$ in. of primacord projecting beyond the lead (see 1C of Figure 5). The function of the lead is to prevent detonation except that starting from the center of the sphere. To obtain maximum charge density and to minimize segregation, all of the air should be driven out of the molten pentolite and the mix should be as cool as possible when poured. The charge is cast in a well-greased (e.g. petroleum jelly) plaster of paris mold (Figure 6) with the exposed end of primacord fuze in the center. The half molds are set over one another on their rims with the fuze in the groove provided and with the filling hole on top. Molten explosive is poured in up to the base of the filling hole and as the mix cools and shrinks, more is added to keep the level constant. When solid, the charge is easily removed by taking apart the molds. Molds may be cooled, regreased, and used again many times.

Charges may also be cast as two hemispheres. One hemisphere is cast with the primacord fuze in place and is removed from the mold when the explosive solidifies. Molten explosive is poured into the second mold up to the level of the fuze groove and the first half (with fuze) is placed on top. ^{4/} The completed charge is easily removed from the mold when the second half solidifies.

The charge is next mounted in the round bottom glass flask which has been split into two halves (see 1B, 1C of Figure 5) by the hot wire technique familiar to glassblowers. Rubber tape is wrapped around the lead covered primacord fuze to provide a snug fit in the neck of the flask and to center the charge. There is a $3/16$ in. space between the charge and the wall of the flask. A small chip of glass is removed from one of the split edges of the flask to provide a filling hole for the gas. The split halves of the flask are glued together with transparent tygon-paint or Duco cement and the region over the seam is painted twice with the cement for waterproofing. Plaster of paris is poured into the neck of the flask to fix the charge in position, aid in waterproofing and minimize the leakage of gas. Bostik cement (a heavy-bodied rubber compound) or vaseline is placed over the plaster of paris to waterproof completely the mouth of the flask. Just before shooting, the charge is placed in a steel (for safety) vacuum desiccator, the air evacuated through the filling hole and argon allowed to flow in an atmospheric pressure. The filling hole is then resealed with a piece of scotch tape and Bostik.

(ii) Conical flash charges for depths down to 10 feet. Only a part of the light distributed by the spherical type flash charge described above is used in illuminating the field of view of the camera. The lighting efficiency may be improved by using a reflector behind the flash charge. However, there was little loss in light when the spherical charge was replaced by a conical

^{3/} Preparation of Charges for the Study of Explosion Phenomena at UERL, by P. Newmark and E. L. Paterson, NDRC Report A-381 (OSRD 6259); also The Preparation and Testing of High-Intensity, Short Duration Underwater Flares, by E. L. Patterson, NDRC Report A-382 (OSRD 6260).

^{4/} While this technique leads to some cavitation at the center of the cold charge, it was found in practice to make little or no difference for this purpose if the precautions noted above were taken.

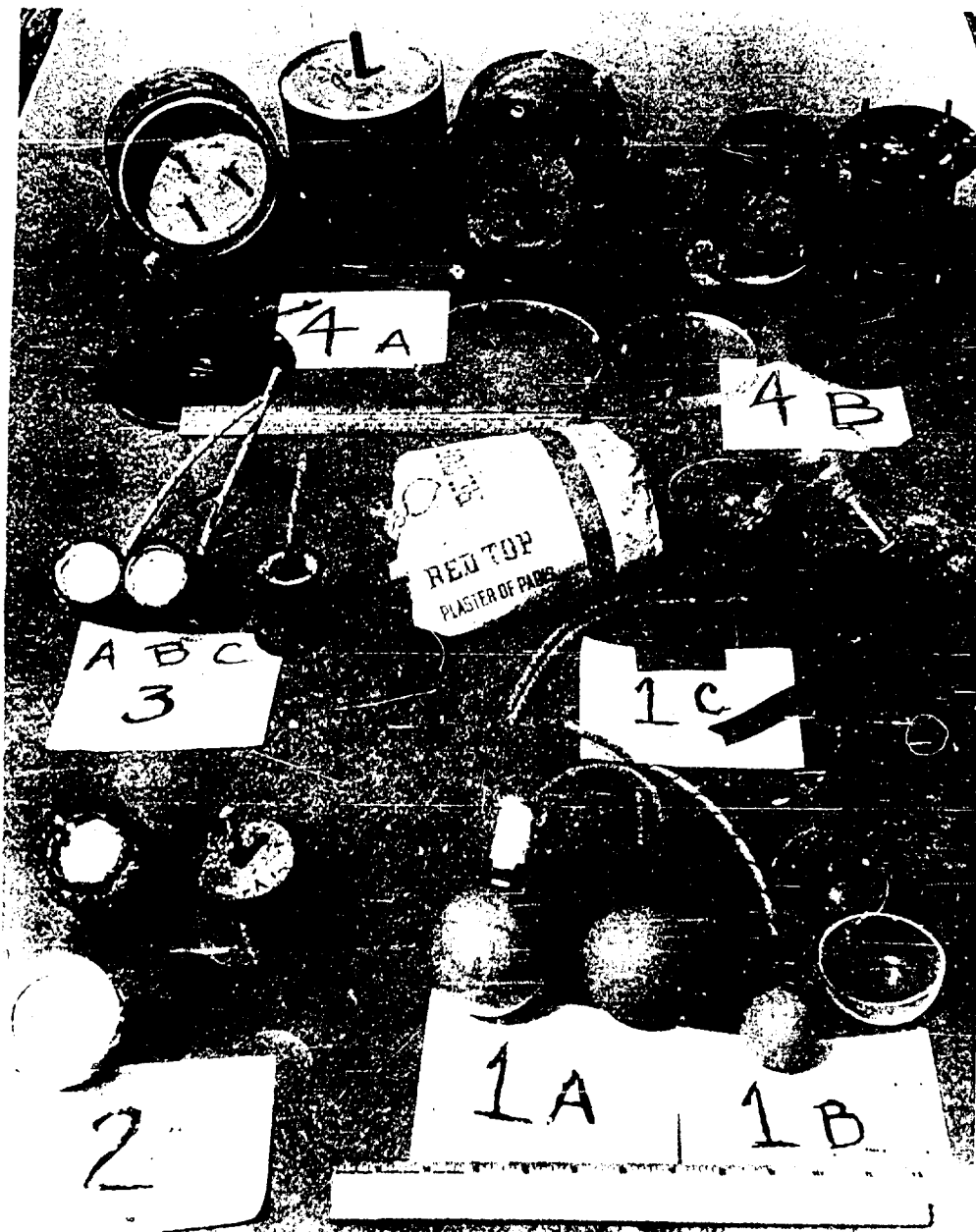


Fig. 5. Various types of flash charges prepared at UERL.

Data for Figure 5 - Various types of flash charges prepared at UERL.

- 1A 250 gm spherical pentolite flash charge - glass-cased and uncased. (See Figure 7).
- 1B 75 gm spherical pentolite flash charge - uncased.
- 1C Materials: primacord, 1/32 in. lead sheet, rubber tape, plaster of paris, and split flask (200 ml round bottom).
- 2 Conical flash charges. (see Figure 8).
- 3 Cylindrical tetryl flash charges (salt coated).
- 4 Flash charges for deep water. (see Figure 9).

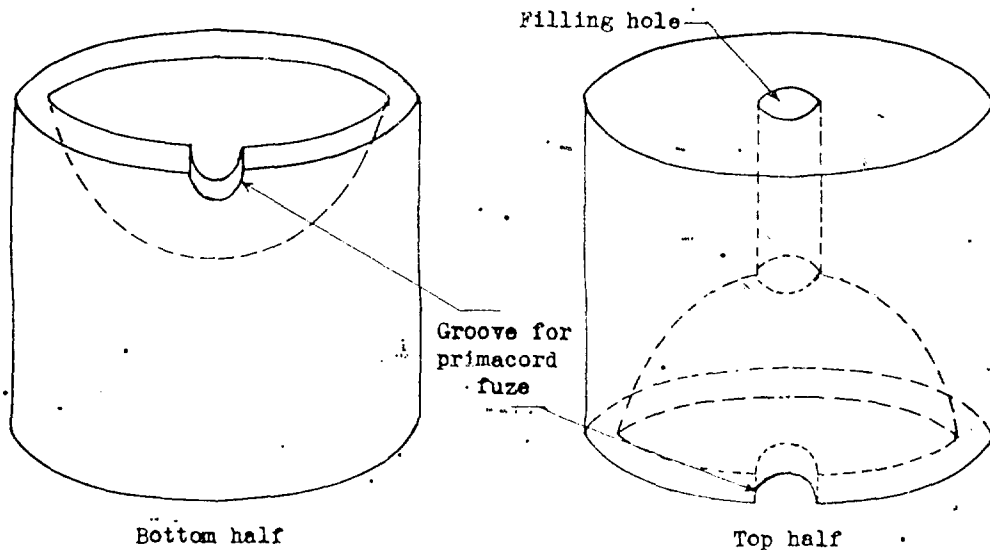


Fig. 6. Plaster of paris molds for casting spherical pentolite flash charges.

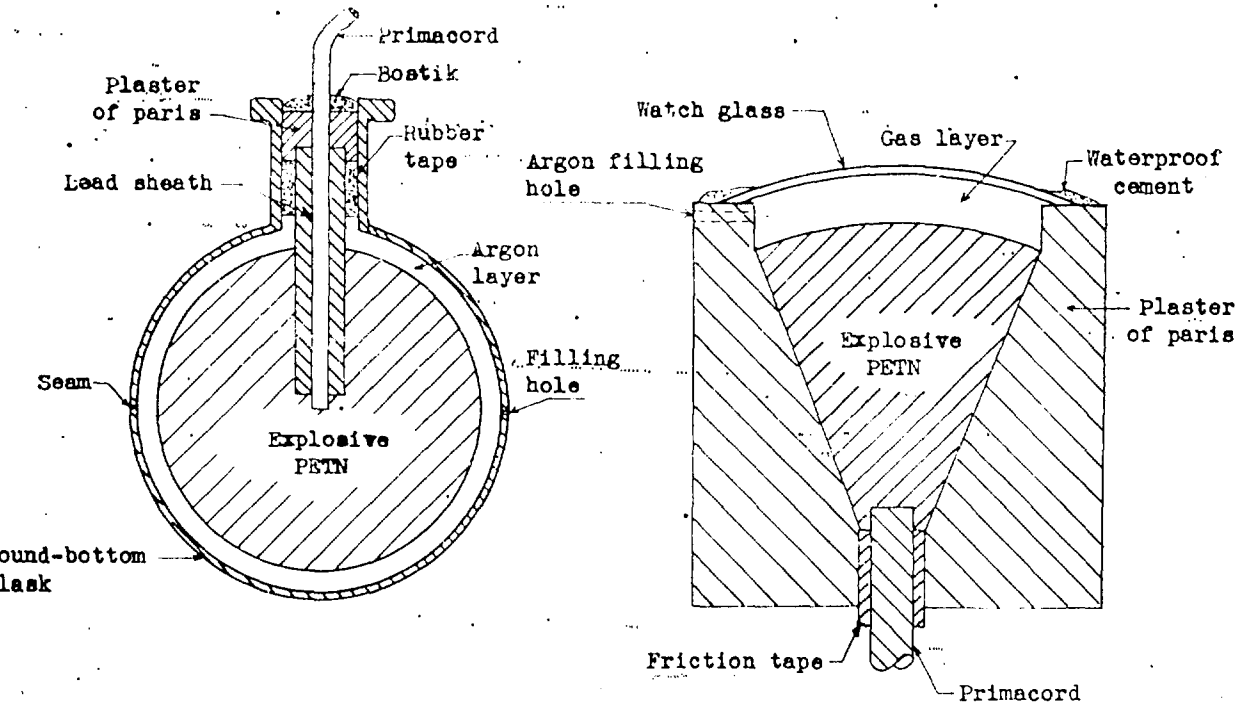


Fig. 7. Glass-enclosed spherical flash charge; a cross-sectional view.

Fig. 8. Conical pentolite flash charge; a cross-sectional view.

charge which was actually a sector of a sphere. (See 2 of Figure 5). The fabrication is indicated by Figure 8. The advantage of this form was that about one-seventh the amount of explosive (~ 40 gm) was required which permitted the use of flash charges in areas where half-pound charges were too large.

(iii) Flash charges for depths down to 600 feet. The construction of a flash charge which would be waterproof in deep water and would not collapse under the hydrostatic pressure was accomplished by casting the pentolite in a tin can and using a thick (1/4 to 1/2 in.) disk of lucite for a window; Figure 9 shows the details. Photographs of this type of charge are given in Figure 5 (4a, 4b). The window is clamped against a rubber gasket and a 1/32 in. hole is drilled in the window for an argon filling hole. This hole was later closed with a tapered plug of wood and Bostik. A metal tube, closed at one end and soldered to the base of the tin can, projected into the explosive to comprise the detonator well. The charge was detonated by inserting primacord into the open end of a non-electric blasting cap, wrapping the junction carefully with rubber tape, inserting the blasting cap into the detonator well, and initiating the primacord.

(iv) Other sources. Some single pictures of damage to model structures were taken with a #22 photoflash lamp or with a gas-filled Kodatron flash tube. Both of these lamps had to be protected from the explosion by a metal case with lucite window. The usual explosive flash charge technique was not employed in this instance because the final damage to the model would have been affected by the explosion of the flash charge.

(e) Underwater equipment. -- Figure 10 shows a sketch and Figure 11 photographs of a typical experimental set-up for underwater photography. The majority of experiments were carried out in rings of this sort. While the circular shape is not the most convenient for the suspension of miscellaneous objects, it is generally less subject to destruction from the explosions. Lightweight objects, such as paper diffusing screens, were stayed from the ring by light line, while cameras, gauges, and other heavy gear were fastened directly to the ring or to sturdy auxiliary structures bolted or welded to the ring.

(f) Firing devices. -- The flash charge and the target charge were generally fired a short time apart by connecting them with primacord. Since it was sometimes undesirable to have primacord extending between the two charges, a method was developed for simultaneously firing two charges which were separated in space. The method was to discharge a 40 microfarad condenser, charged to 600 - 1000 volts, through two No. 8 SGS seismographic caps connected in series. Under these conditions the caps detonated within a few microseconds of each other. Primacord was still necessary to obtain delays, but more control was obtainable over the geometrical configuration of the primacord since it was no longer necessary to have a continuous length between the two charges. Furthermore, this eliminated the necessity of having primacord in the field of view when photographing exploding charges.

2. Methods of motion picture photography.

Relatively slow phenomena, such as bubble growth and structural damage, can be photographed successfully using motion picture technique. We have used two conventional movie cameras and an Eastman High Speed camera, all of which require a continuous light source. For pictures in which a total duration of only 100 milliseconds is required, such as studies of damage from a 25 gm charge at 600 ft. depth, a single #31 photoflash lamp has been used. For longer durations it is possible to use several photoflash lamps tripped in series.

Eastman Super XX film or its equivalent has been used in all underwater movies.

(a) Cameras for motion picture photography. --

(i) Eastman high speed camera. Figure 12 shows the Eastman high speed electrically driven 16 mm camera with attached Lord vibration mounts. The mounts slide into the tracks shown inside the case, (Figure 13) and shock mounts

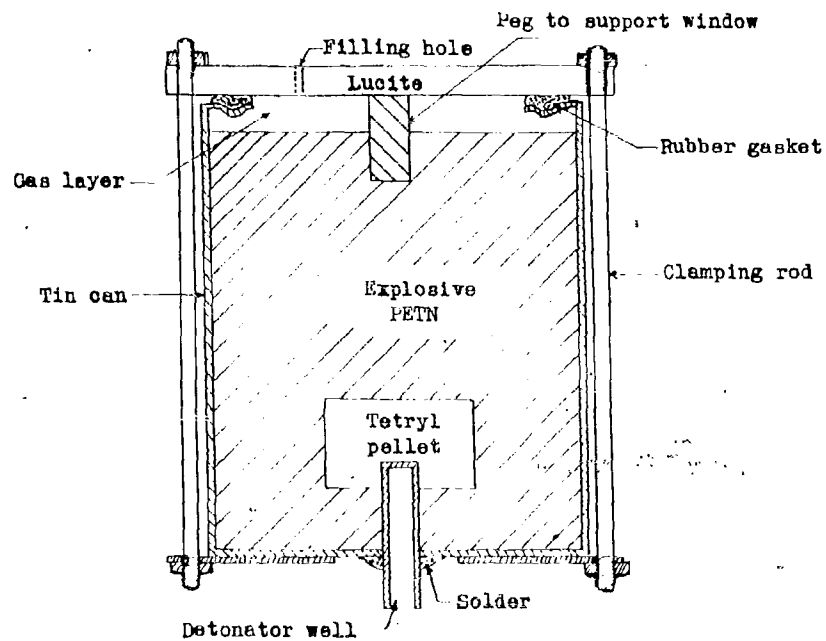
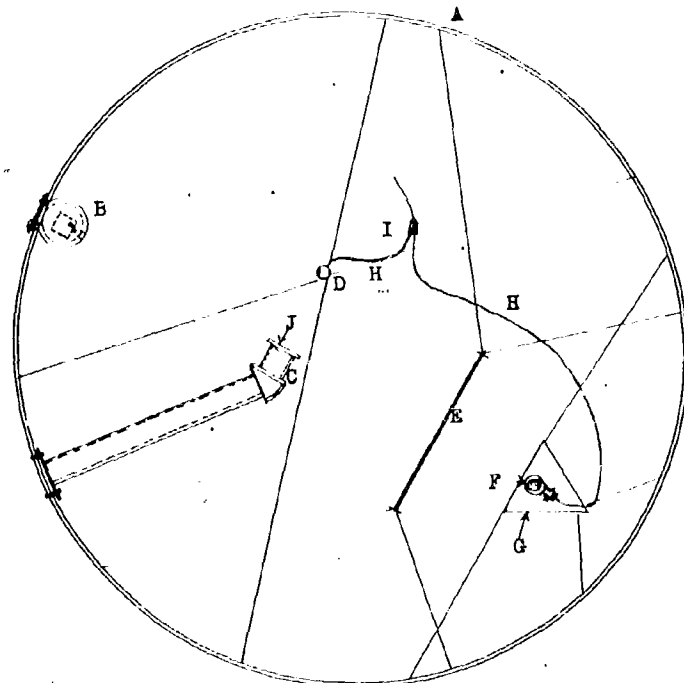
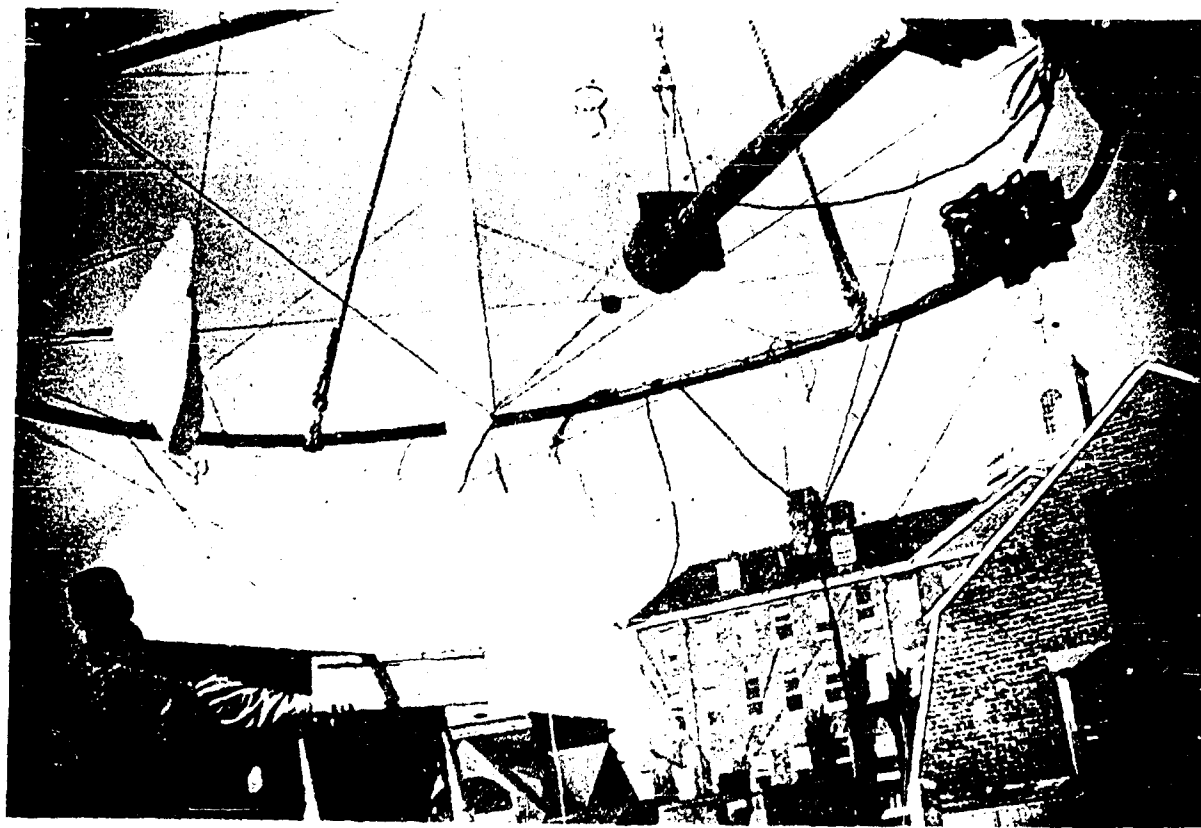


Fig. 9. Flash charge for deep water; a cross-sectional view.

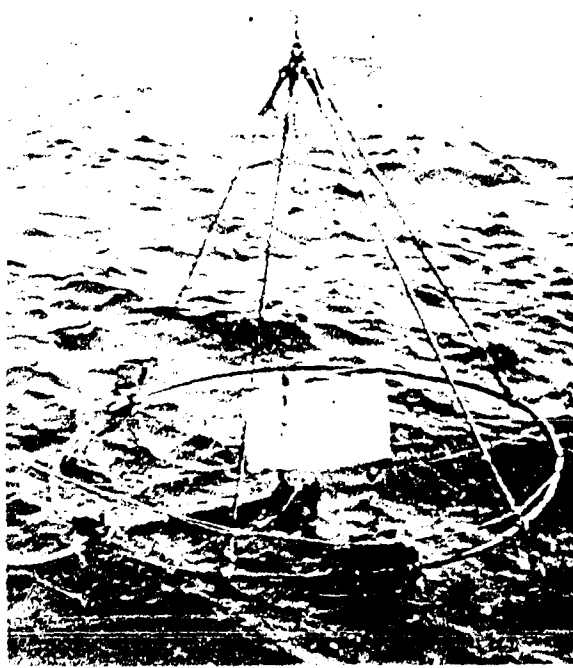


A. Ring - 9 ft diameter	F. Flash charge
B. Camera	G. Reflector
C. Gauge	H. Primacord
D. Damaging charge	I. Cap - No. 8
E. Diffusing screen	J. Diaphragm

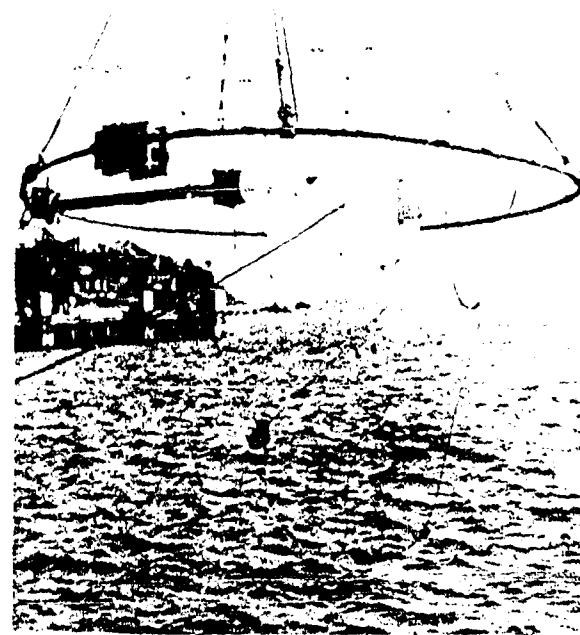
Fig. 10. Diagram of apparatus for underwater photography.



Close-up, showing camera, charge, diaphragm, diffusing screen, and flash charge reflector



Apparatus just entering water



Ring swung out over water preliminary to lowering

Fig II. Steps in lowering equipment for single shot photograph of charge damaging diaphragm.

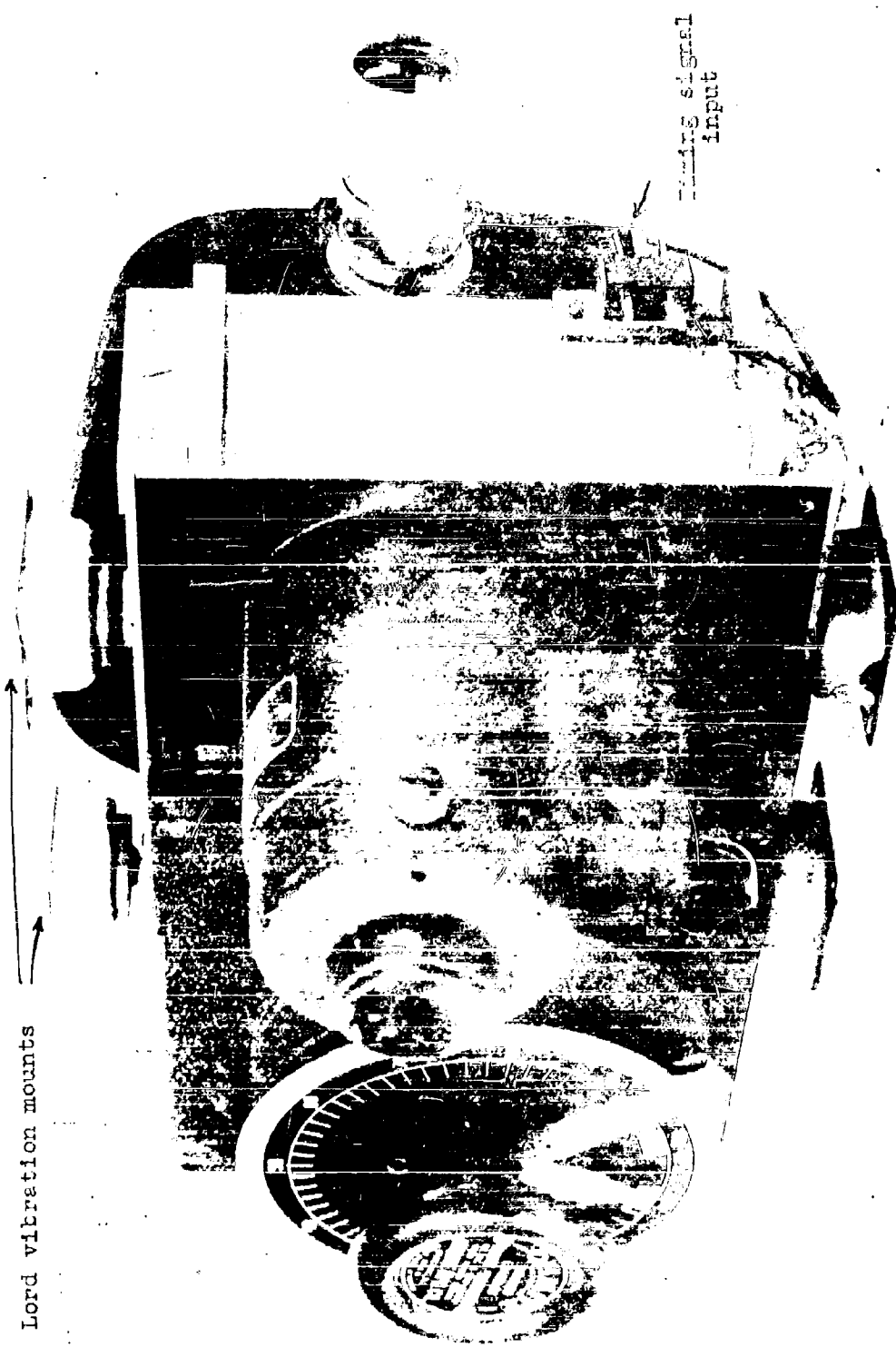


FIG. 12. Eastman high speed camera.

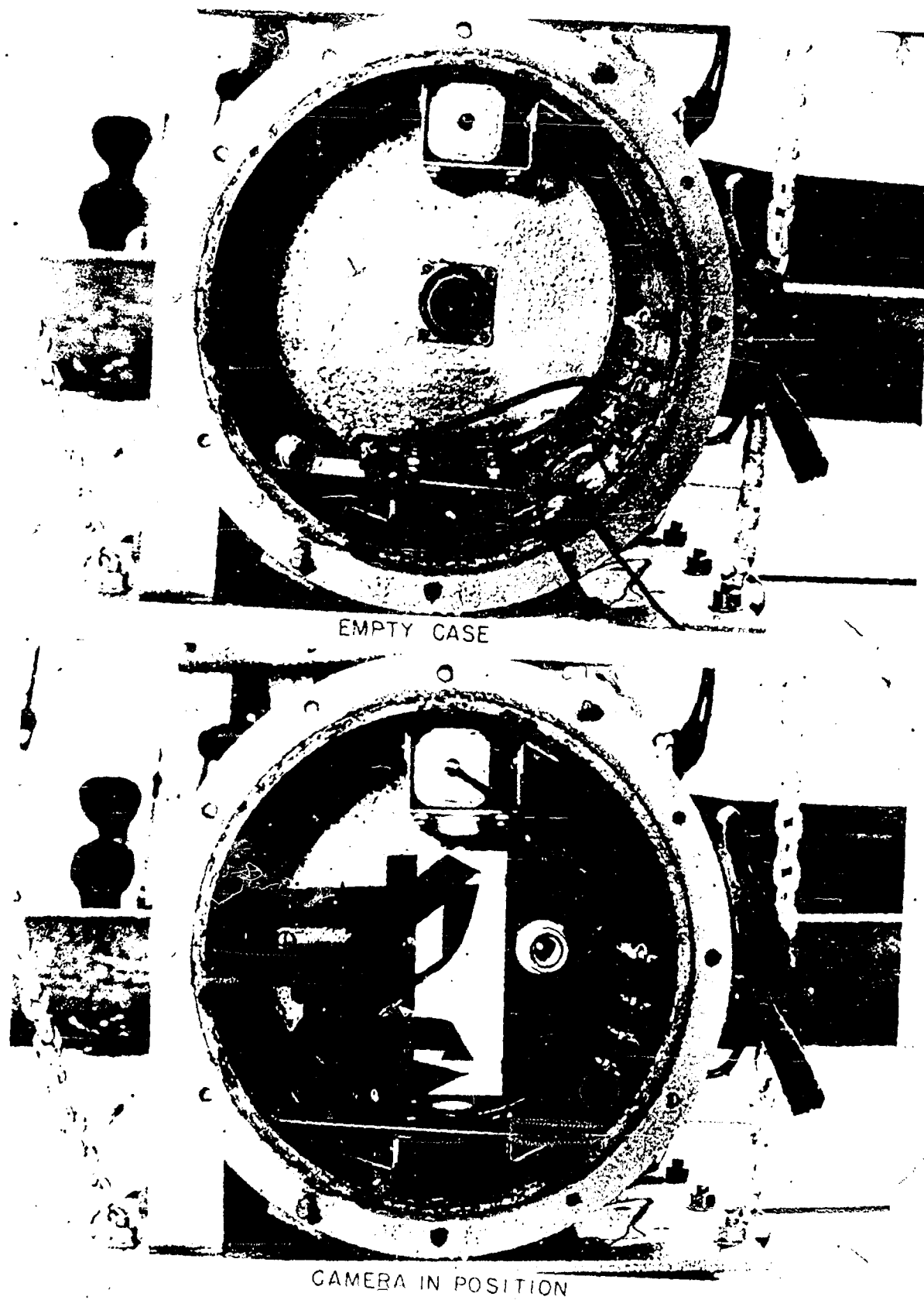


FIG. 13
HIGH SPEED CAMERA AND "EXPLOSION PROOF" CASE

on the ends of the case prevent camera motion along the axis of the cylinder.

The case for this camera is made of standard 16 in. O.D. by 3/8 in. wall thickness steel tubing, and the ends are hot rolled steel 1 in. thick. We have never tested this case near its ultimate strength, but it was calculated that it would stand over 1000 lbs./in.² static pressure and considerably more dynamic pressure of low time constant.

The high speed camera can be used at speeds up to 3000 frames per second. Due to the rotating four-sided prism that is interposed between the lens and the film, the ratio between exposure time and the time between frames is fixed at 1/4 and the minimum exposure time is 80 microseconds. Another effect of the optical system is that it requires long focal length lenses (63 mm minimum) with the result that the field of view is small (angle of view ca. 5°) at reasonable object distances. This feature is a drawback in underwater photography due to the further restriction of the field which results from the high index of refraction of water, and the severe limitations on object distances due to water turbidity.

- (ii) Jerome camera. Figure 14 shows the Jerome 35 mm camera. This camera is of a conventional type, electrically driven, and is limited to speeds slower than 100 frames per second. The angular opening in the shutter is variable, so that exposures as short as one millisecond can be made. A 1 in. focal length lens was used to obtain the widest possible angle of view. The shock mounts shown in the figure engage tracks in the case.
- (iii) Victor camera. Our first underwater movies were taken with an ordinary spring-wound 16 mm camera running at 64 frames per second, with an exposure time of approximately 1/130 second.

(b) Associated equipment for underwater photography.

- (i) Underwater gear. One of the rigs used for photographing damage to cylindrical targets is shown in Figures 15 and 16. The photograph (Figure 15) shows the rig arranged for photographing by reflected light while the drawing (Figure 16) shows the set-up for silhouette. The parallel beams in this frame can be extended to obtain greater object distances. Figure 17 shows the firing circuit diagram.

(c) Light sources.

- (i) Photoflash lamps. In order to increase the duration of the illumination used in these photographs, several photoflash lamps may be set off in sequence by means of the rotating commutator switch shown in Figure 18. The proper time interval to use between #31 photoflash lamps is 80-100 milliseconds. In the clear waters around the Bahamas, it was found that a good silhouette of a cylinder could be obtained at 2500 frames per second with the lens at f/11 using two #31 photoflashes 9 ft. from the camera.
- (ii) Mercury Arc. The light source used with the Victor camera was a G. E. high pressure H-6 mercury arc. This proved satisfactory except that in a fair fraction of the experiments the light was extinguished by the shock wave. Furthermore the intensity is too low for high speed work, and 60 cycle fluctuation would be undesirable in short exposure pictures.
- (d) Timers. -- Each camera is equipped with a small neon flashor which provides timing by marking the edge of the film at a frequency determined by tuning forks - 1000 cycles for the High Speed and 50 cycles for the Jerome. Circuit diagrams for the power supplies that operate these lamps are given in Appendix III.
- (e) Power supply for cameras. -- The cameras must be brought up to speed gradually. The High Speed is equipped with an internal mechanism which cuts out a resistor and provides for gradual acceleration. The Jerome is accelerated by hand with a Variac. The High Speed requires about 1.5 kw (2 at starting) and the Jerome less than 1 kw.

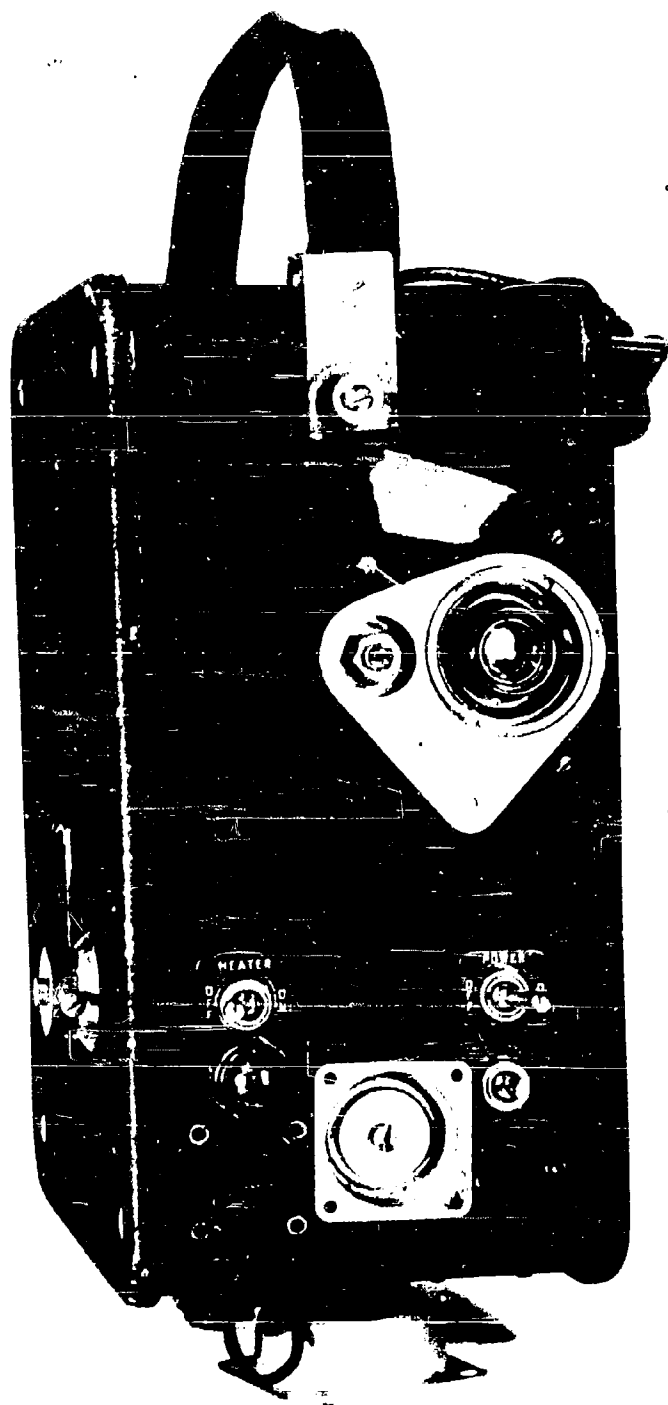


Fig. 14. Jerome camera showing shock mounts.

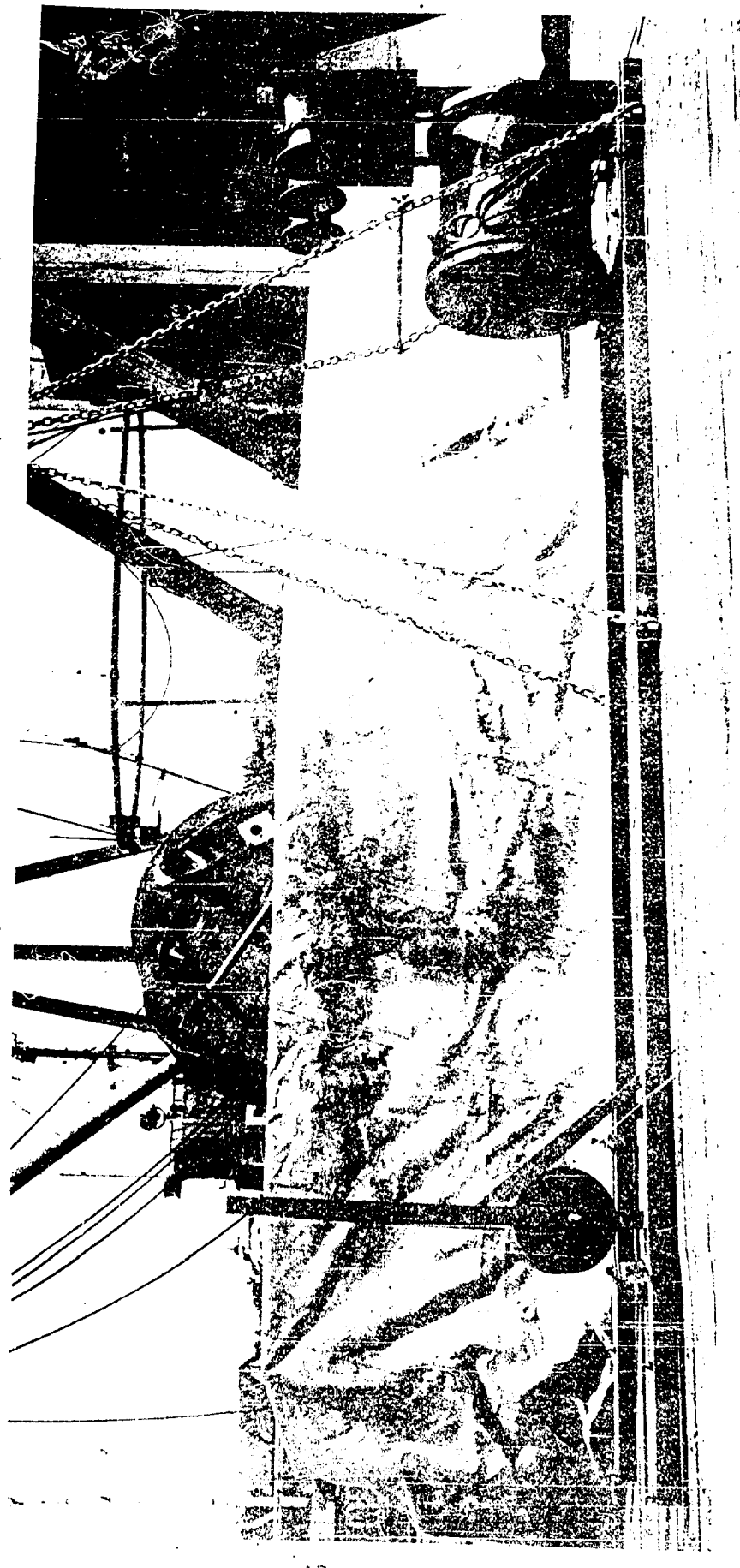
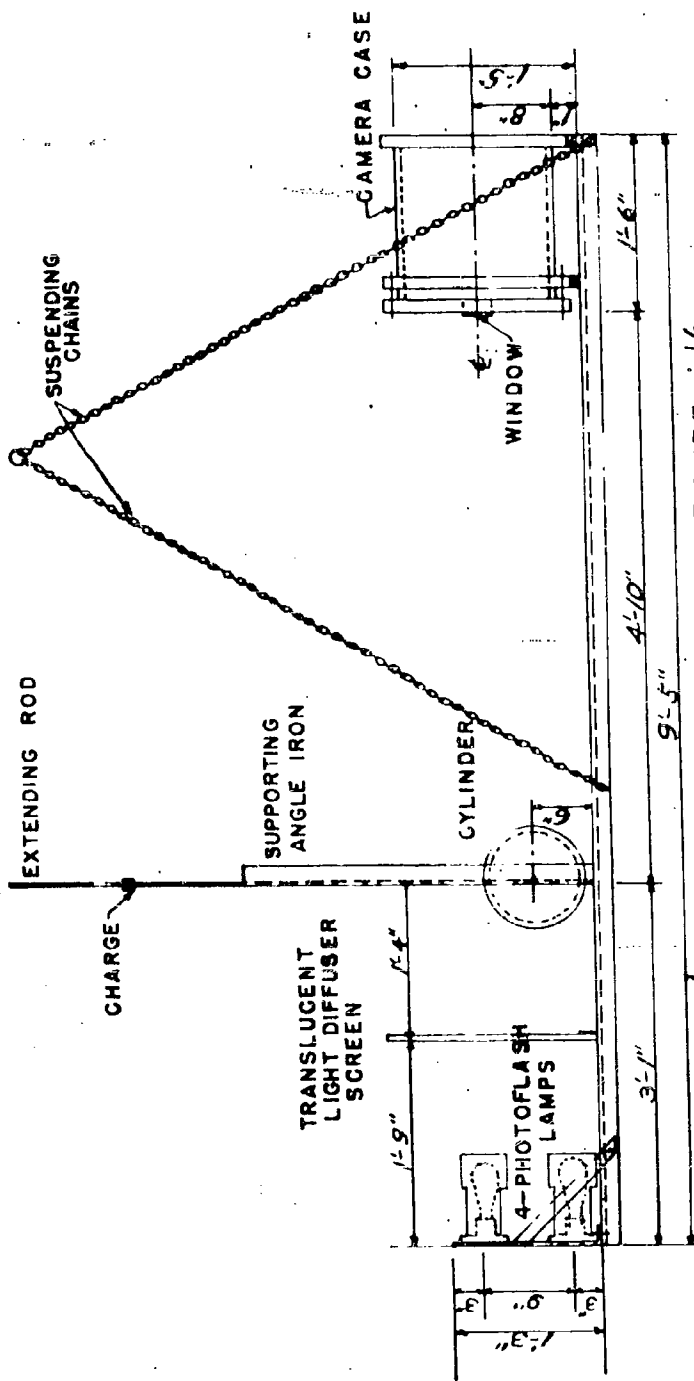
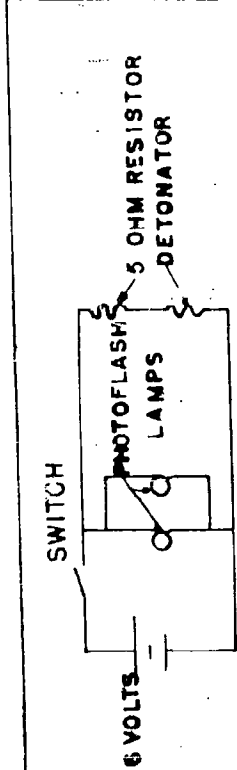


Fig. 15. Rig for high speed photography of cylinders.



FIGURE—16
SIDE ELEVATION OF APPARATUS
USED FOR PHOTOGRAPHING CYLINDER



FIGURE—17
FIRING CIRCUIT DIAGRAM

DRAWN BY HRC
7-24-45

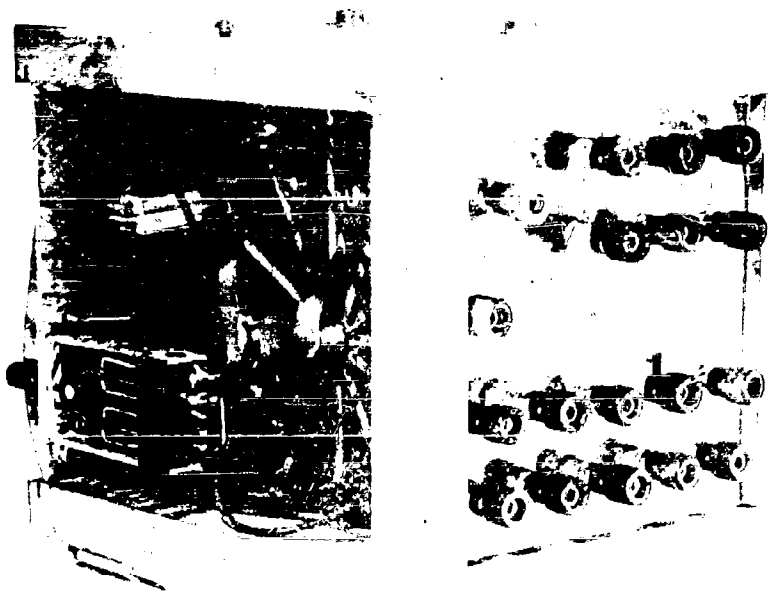


FIG. 16. Rotating commutator switch for firing photoflash lamps in sequence.

III. RESULTS OF EXPERIMENTS

1. Cavitation

Inasmuch as damage theories depend on the presence or absence of cavitation, it was considered important to investigate experimentally the more important factors influencing the production and decay of cavitation. The various divisions of this problem will be discussed separately.

(a) Minimum tension necessary to cause cavitation. -- While theoretical considerations lead to the expectation that very high negative pressures should be necessary to start cavitation in extremely pure (nucleus-free) water, it can be demonstrated that if bubbles or particles of radius r_b are present, cavitation should appear at $P = -2s/r_b$, where s is the interfacial tension between water and the particle. Inasmuch as seawater contains numerous suspended particles, some of considerable size, cavitation might be expected at small negative pressures (tensions).

In order to determine the minimum tension required for cavitation in seawater, the following experiment was carried out: A weak shock wave impinged on an air-backed cellulose acetate diaphragm 0.02 in. thick and 6 in. in diameter. At a known time after impact a photograph was taken and the position of the cavitating region noted. From the curves given in Appendix I, the tension was estimated at the minimum distance from the diaphragm at which cavitation occurred, since the magnitude of the tension is a direct function of the distance from the diaphragm, this value gives the minimum tension necessary for cavitation. It is possible that lower values can be found under other conditions.

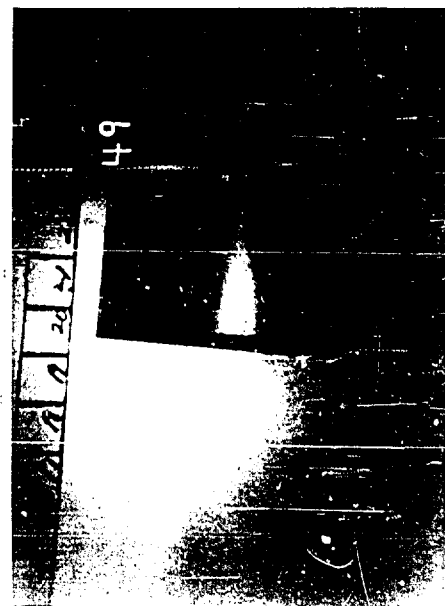
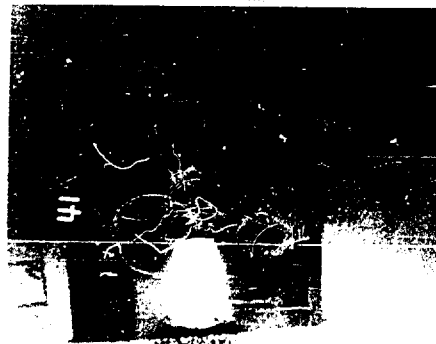
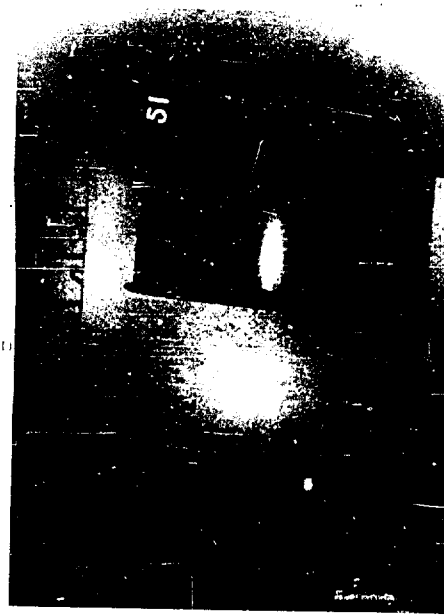
Figure 19 shows cavitation in front of such a surface when a 10 gm charge of loose tetryl was fired 24 in. from the diaphragm. The peak pressure 24 in. from this charge is estimated to be 2700 lbs./in.². The charge used in making Figures 20, 21, and 22 was a three-foot piece of primacord stretched in a straight line perpendicular to the diaphragm at its center. For Figure 20 the closest end of the primacord was 8 in. from the surface of the diaphragm, in Figure 21 it was 10 in. and in Figure 22 it was 20 in. The peak pressures p_0 in the shock fronts at the target are estimated to be 1100, 900, and 450 lbs./in.² respectively. The letters A and B mark the positions of the primary and reflected shockwaves respectively as observed in the original negatives. It will be noted that cavitation is visible in all four pictures.

The theory of Appendix I has been used to estimate the pressures in the water in front of the diaphragm. This simple theory assumes that the shock front is planar, that the diaphragm acts as an incompressible free plate of infinite extent, and that the region ahead of the cavitation front is unaffected by the presence of the cavitation.

Cavitation is observed at least as close to the diaphragm as 1/8 in. From Figure 131 (Appendix I) it is estimated that the pressure at this point ($X = 0.04$) never falls below $P = 0.1$ or $p = -0.1 p_0$. In the case photographed in Figure 22 this means, according to this theory, that the tension $-p$ near the diaphragm never exceeded 45 lbs./in.². We therefore conclude that cavitation in seawater can occur at 45 lbs./in.² (or even less) on the basis of this interpretation of the experiment. Since the maximum tension possible in this experiment on any theoretical basis is 450 lbs./in.² we conclude that this value represents an upper limit for the required tension. These values are estimated relative tensions, from which about 18 lbs./in.² must be subtracted to correct for atmospheric plus hydrostatic pressure.

(b) Criterion for cavitation in front of a steel diaphragm. -- Kirkwood 5/ has

5/ The Plastic Deformation of Marine Structures by an Underwater Explosion Wave II, John G. Kirkwood, OSRD-1115, Serial No. 450, December 9, 1942.



Reproduced From
Best Available Copy



postulated (See Appendix I) that cavitation at a particular point in front of the diaphragm will occur only if the cavitation time θ_c is less than the time for the diffracted wave to come in from the edge of the diaphragm and that the cavitation time can be calculated for an infinite rigid free plate by

$$\theta_c = \frac{\theta \theta_1}{\theta - \theta_1} \ln \frac{\theta}{\theta_1}$$

in which θ is the time constant of the shock wave and $\theta_1 = m/c$, m being the mass per unit area of the plate, ρ and c the density and sound velocity of water, respectively. In order to test this hypothesis, two series of photographs were taken.

In one series, shock waves were reflected from a deformable steel diaphragm, the center of which should approximate the motion of a free plate in the initial part of its motion. In the other series, a closer approximation to a true free plate was made by supporting a steel disk on a weak backing of cellulose acetate or shim brass, and in a few pictures there was no support for the steel plate.

Figures 23, 24, 25, 26, and 27 show UERL diaphragm gages being damaged under the conditions given in Table I. The table shows that cavitation occurs only when θ_c is less than R/c , where R is the radius of the diaphragm. In a few cases, no cavitation occurred under this condition, but the condition was satisfied by only a slight margin. In Figure 25 the cavitation region does not extend back to the diaphragm. This is thought to be due to the increase in pressure caused by "reloading" or deceleration of the diaphragm.

The target used to obtain Figure 28 was a 0.013 in. thick steel diaphragm soldered over the mouth of a 6 in. pipe. Five other photographs were taken of similar targets in which the only experimental condition changed was the time lapse after impact of the shock wave from the 50 gm charge at a distance of 12 in. Cavitation occurred in all pictures except one in which this time lapse was approximately 8 μ sec, whereas the calculated cavitation time (θ_c) is 6 μ sec.

Figure 29 is a drawing of the target used in the second series of photographs to give a closer approximation to a free plate.

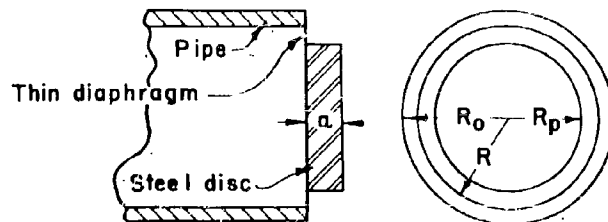


Figure 29. Target simulating free plate.

Typical photographs of cavitation from such a target are Figures 30, 31, and 32. Using this target, it is found that the position of the cavitation front is very close to the region of zero pressure calculated by the method of Appendix I.

Measurements were also made of the radius R_c of the cavitation region and of the maximum perpendicular distance from the plate that cavitation occurred, x_c . The time after impact at which the picture was taken t_c was calculated from the value of x_c 6. These values are shown in Table II, together with the corresponding time

6/ The equation for this was developed from the theory of Appendix I.

$$t_c = \frac{\theta}{\beta - 1} \ln \frac{2\beta}{(\beta + 1) e^{x_c/c\theta} - (\beta - 1) e^{-x_c/c\theta}}$$

where

$$\beta = \theta/\theta_1$$

TABLE I. Cavitation data for steel plates in UERL diaphragm gage.

Fig. No.	Film No.	Charge Weight (gm)	Distance (in.)	θ (μ sec)	Plate Thickness (in.)	Cavitation Time θ_c (μ sec)	R/c (μ sec)	Cavitation Observed?
	2	50	12	35	0.013	6	29	yes
	3	50	14	35	.013	6	29	yes
23	1	50	24	40	.025	8	29	yes
	218	50	24	40	.040	12	29	yes
24	219	50	24	40	.039	12	29	yes
	220	500	48	80	.038	15	29	yes
	5	50	12	35	.074	17	29	yes
25	19	250	30	55	.073	19	29	yes
26	70	250	36	55	.076	20	29	yes
27	24	50	12	35	.156	28	29	no
	23	250	30	55	.156	34	29	no
	4	50	12	35	.500	45	29	no
	21	75	12	40	.500	48	29	no
	22	75	12	40	.500	48	29	no
	31	75	12	40	.500	48	29	no

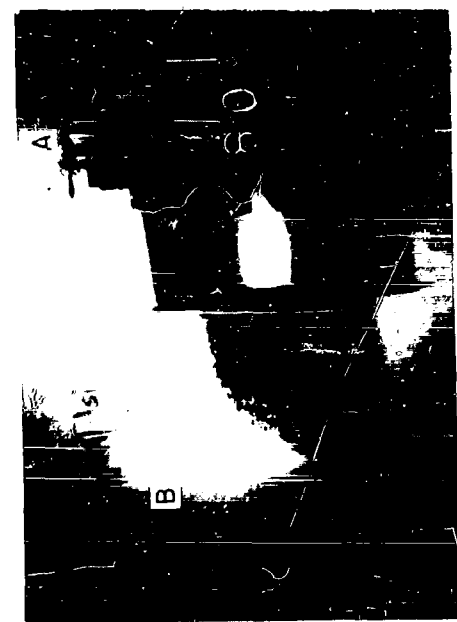


FIG. 30

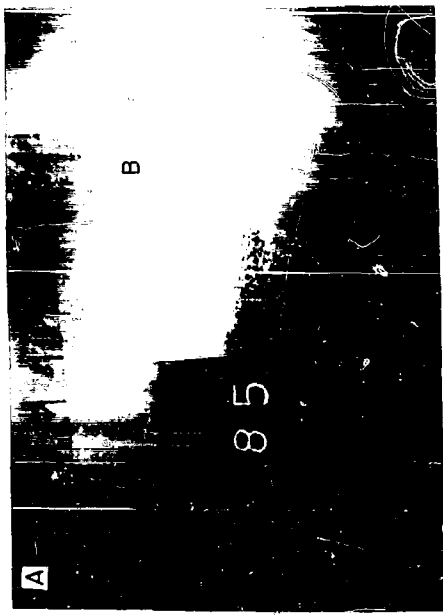


Fig. 31

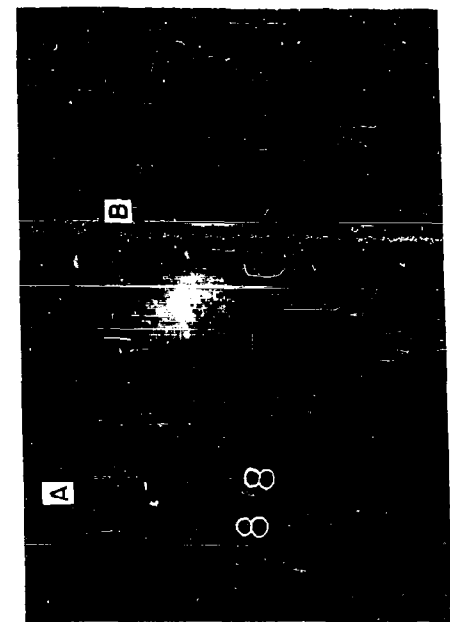


Fig. 32

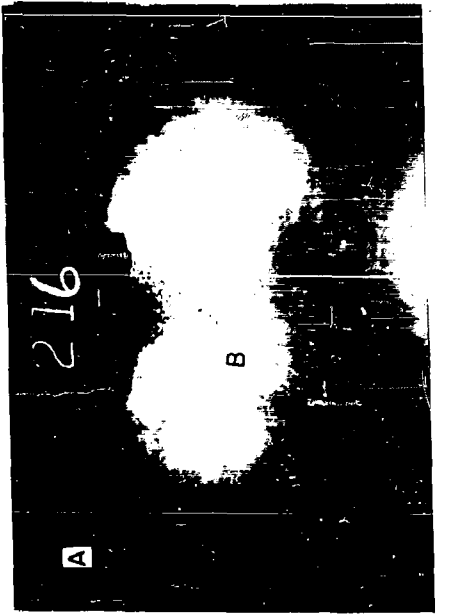


Fig. 33

Figs 30-33. Cavitation from "free" plates.
A= Initial shock wave B= Reflected wave

t_s found from the shock wave position. The radius of the cavitation region R_c was also calculated and the values are shown in Table II together with the measured values. In the calculation it was assumed that cavitation takes place only in the region where the pressure drops to zero before the compressional diffraction wave from the edge of the plate arrives. ^{7/}

It is assumed that once cavitation appears, it persists for some time after the diffraction wave from the edge of the plate has reached it. (See Section III, 1, d.) The rather good agreement of the calculated and observed results for both sets of values argues that the assumptions made in the calculations, including the low value for the tension necessary for cavitation, are roughly correct.

The target used to obtain Figure 33 was an essentially completely free plate which is illustrative of several experiments. A small can filled with air was hung with its open end down and the disk was supported at the air-water interface on small clips which offered no resistance to its motion. The fact that no essential difference is shown between these experiments and the type illustrated by Figure 29 indicates that plates mounted as in Figure 29 were essentially "free" plates.

(c) Cavitation from objects other than plane surfaces. -- A single photograph of an early UERL cylinder taken 200 μ sec after impact of a shock wave from a 65 gm tetryl charge 30 in. distant showed a considerable region of cavitation. This is seen in Figure 34; the cylinder is not shown because of the restricted field of view. The cylinder axis is parallel to the plane of the photograph and the top edge of the cylinder is in view at the lower edge of the picture. Figure 35 shows cavitation off the side of a 4.5 x 5 x 0.011 in. paint can 129 μ sec after being damaged by a 25 gm charge 48 in. away.

Figures 36, 37, and 38 demonstrate that no cavitation occurs when a 1/4 in. piezoelectric gage, or a Hartman type momentum gage or a 5 x 5 in. cylinder of steel is hit by a shock wave from 250 gm of tetryl at 30 in.

(d) Disappearance of cavitation. -- If the cavitation bubbles consist simply of water vapor, it seems hard to understand why these bubbles persist for long times after the pressure has returned to the hydrostatic level. In an attempt to cast some light on this problem, a series of experiments was performed in which cavitation was allowed to disappear spontaneously, while, in another series, auxiliary shock waves were passed into the cavitation region.

Figures 39, 40, 41, 42, and 43 show a series of photographs in each of which a 0.002 in. brass diaphragm supported by a 6 in. pipe was ruptured by a 25 gm charge 12 in. away. The pictures are taken at different times after the impact as shown. The finest bubbles begin to disappear by 125 μ sec and there is only a trace of cavitation left at 400 μ sec.

Figures 44, 45, 46, 47, 48, and 49 show the effect of an auxiliary shock wave. The auxiliary charge, data for which are given in Table III, is detonated at the same time as the charge causing cavitation either by means of primacord or the simultaneous cap method. It may be seen that increase in the pressure of the auxiliary shock wave results in more effective destruction of the cavitation, that increase in time constant has but little effect, and that the large bubbles are much more resistant than the fine bubbles.

(e) Cavitation caused by oblique reflection of shock waves from air-water interfaces. -- Experiments were performed to discover whether there was a critical angle of reflection from a water-air interface beyond which no cavitation would occur. The

^{7/} In computing the time at which the diffraction wave relieves the tension in front of the plate, it must be remembered that the front of the diffraction wave may actually reduce the pressure in front of the plate and only in later stages raise it, since initially the pressure is higher in front of the plate than in the surrounding water. It is only when the plate is surrounded by an infinite baffle that the diffraction wave is always positive relative to the existing pressure.

Table II. Summary of results of studies of cavitation from simulated free plates.

Fig. No.	Film No.	Inside Radius of pipe (in.)	Thickness of disk (in.)	Radius of disk (in.)	Charge weight (g)	Charge-plate distance (in.)	Time constant of shock wave θ (microsec)	R_c (calc) (in.)	R_c (obs) (in.)	x_c (obs) (in.)	t_c (calc) (microsec)	t_g (obs) (microsec)
	77	2.78	.154	1.65	25	24	32	1.59	1.98	1.5	2.0	47
	79	"	"	"	150	"	44	2.19	1.78	1.5	2.4	56
30	80	"	"	1.00	"	"	44	2.19	1.78	1.9	2.6	58
	83	1.78	"	1.65	25	12	24	1.20	1.12	1.1	1.8	42
31	85	"	"	"	150	24	44	2.19	0.78	0.6	3.2	69
32	88	2.63	.255	2.33	"	"	44	1.33	1.46	1.1	1.25	47
	93	1.55	.154	1.38	"	"	44	2.19	0.55	0.3	---	66
	95	1.55	"	"	250	"	51	2.54	0.46	None	---	74
	97	1.79	.382	1.66	150	"	44	0.88	0.48	0.3	1.8	59
	99	"	"	"	"	"	44	0.88	0.48	0.5	2.5	72
	100	1.55	.190	1.38	"	"	44	1.78	0.48	0.3	2.4	58
	201	2.63	.502	2.47	25	12	24	0.37	1.80	1.1	3.0	78
	202	1.80	.382	1.76	250	24	51	1.02	0.33	0.2	2.8	76
	203	1.55	.190	1.34	"	"	51	2.06	0.37	None	---	85
	204	1.80	1.06	1.63	"	"	51	0.37	0.04	None	---	No Cav.
33	214	1.60	0.150	1.59	25	12	24	1.20	0.95	0.90	2.2	48
	216	"	"	"	"	"	24	1.20	0.95	1.0	1.2	41
												38

Table III. Experimental conditions applying to the photographs of Figs. 39 - 49.

Target, .002 in. air-backed brass diaphragm over end of 6 in. pipe.

Cavitation produced by 25 g loose tetryl charge.

Distance from target to cavitation producing charges, 12 in.

Figure Number	Auxiliary charge and shock-wave data					Approximate time interval between impact of cavitation producing wave and picture (microsec)
	Charge weight (g)	Charge to shock wave distance (in.)	Calc. Peak pressure (lb/in. ²)	Calc. time constant (microsec)		
39	None					75
40	None					125
41	None					175
42	None					225
43	None					400
44	25	20.5	4400	30		125
45	150	40	4000	49		235
46	150	35	4600	48		125
47	250	44	4400	60		125
48	250	14.5	13000	45		125
49	25	35.5	2500	35		90

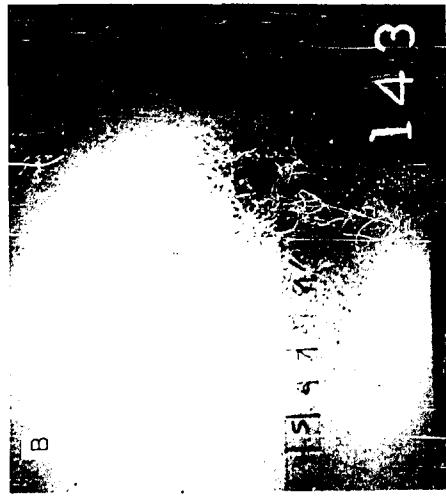


Fig 34

Cavitation about collapsing cylinders

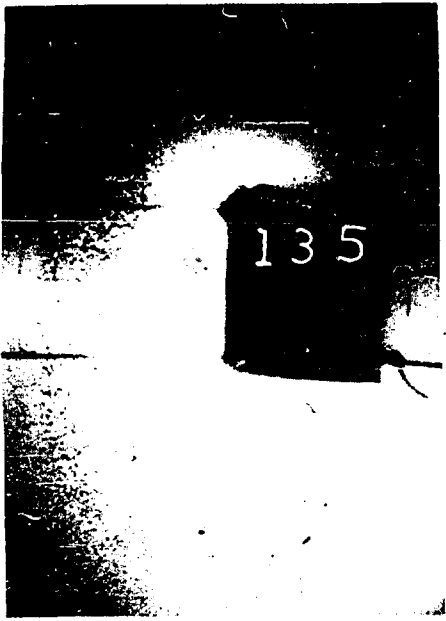


Fig 35

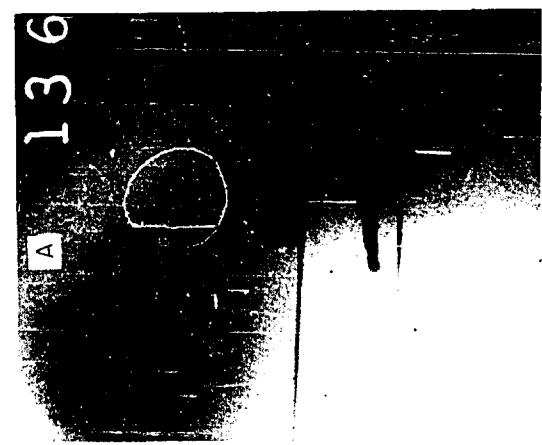


Fig 36
Piezo electric gauge

A = Initial shock wave

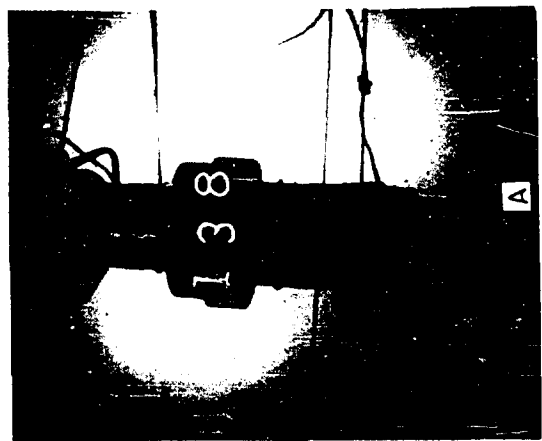


Fig 37

Momentum gauge
B = Reflected wave

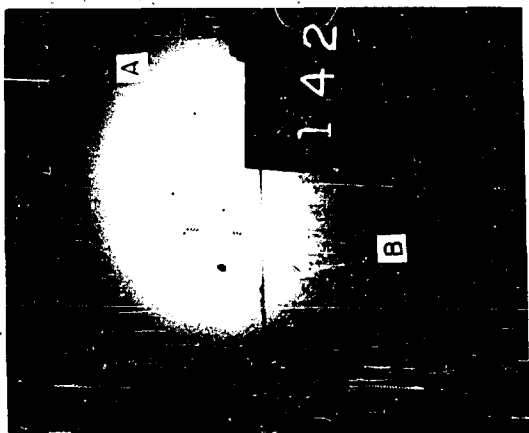
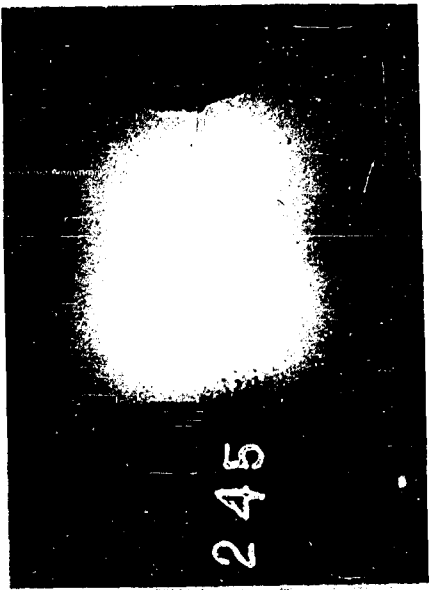


Fig 38
Steel block

A = Initial shock wave
B = Reflected wave



Figs 39-43 Spontaneous disappearance of cavitation at various times after impact of shock wave

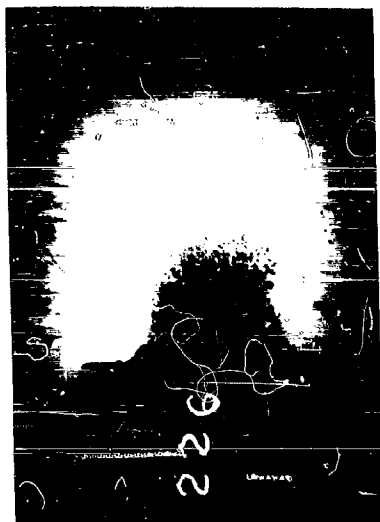


FIG. 46



FIG. 45.



FIG. 44



FIG. 49

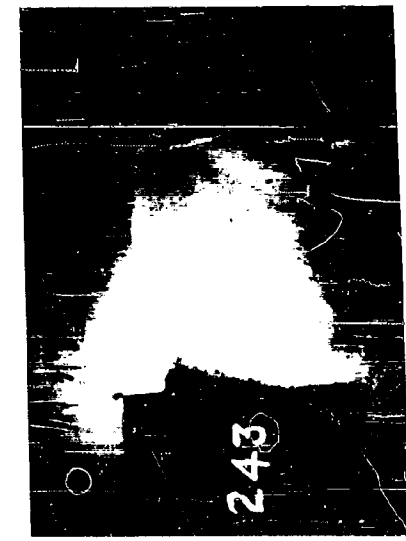


FIG. 48



FIG. 47

DESTRUCTION OF CAVITATION BY SHOCK WAVES
[EXPERIMENTAL CONDITIONS IN TABLE III]

water-air interfaces were provided by filling with air to hydrostatic pressure a 6 in. pipe open on the bottom as shown in Figure 50. Other experiments were carried out substituting a 20 x 10 in. sheet metal trough for the pipe, and finally by using the surface of the sea on a calm night. It was found that such a critical angle existed and was greater for greater size of surface.

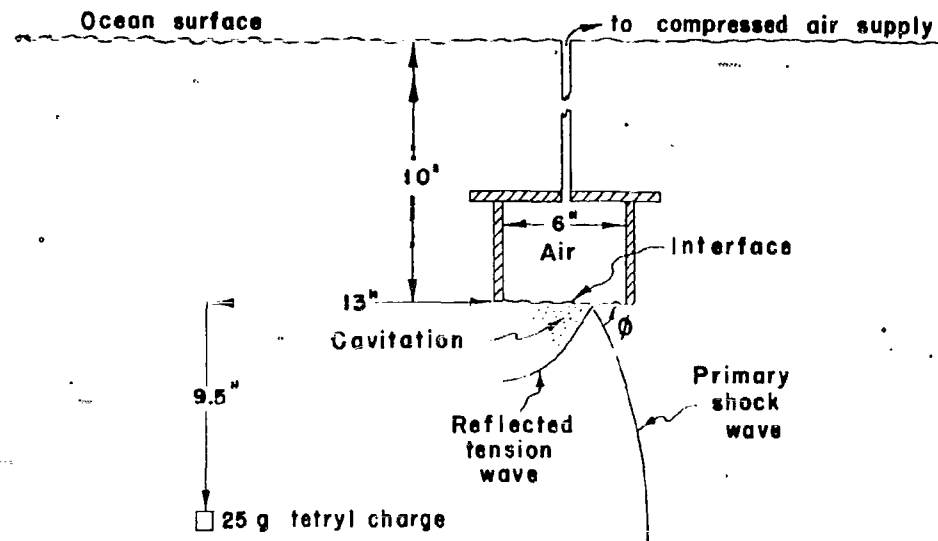


Figure 50. Sketch showing experimental arrangement for Figs. 51 - 56.

The results of the experiments with the six in. pipe are listed in Table IV, and six representative pictures are shown in Figures 51, 52, 53, 54, 55, and 56. The critical angle is about 70° for the conditions of these experiments.

Table IV Data of Experiments on Oblique Reflection of Shock Waves from Water-air Interfaces

Fig. No.	Film No.	Charge Weight (gms)	Distance, Charge to Shock Front (in.)	Angle of Incidence ϕ (degrees)	Estimated Peak Pressure (lbs/in. ²)	Cavitation ?
51	256	25	23 1/2	0	3700	yes
52	270	250	45	45	4200	yes
-	258	25	22 1/2	50	3900	yes
-	261	25	19 1/2	56	4500	yes
53	264	25	19 1/2	62	4500	yes
54	265	250	45 1/2	69	4100	no
55	259	25	21	70	4200	no
-	267	25	20 1/2	71	4300	?
-	269	250	46	71	4100	no
56	257	25	23	90	3800	no

With the large trough, pictures have been taken up to 80° and, using the surface of the ocean, up to 83° . Cavitation was present in all cases, although it was much fainter at the larger angles. See Table V for complete data and Figures 57, 58, 59, and 60 for typical examples.



Fig. 53
62°

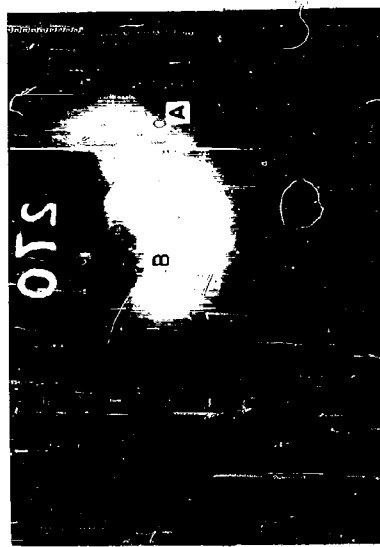


Fig. 52
45°

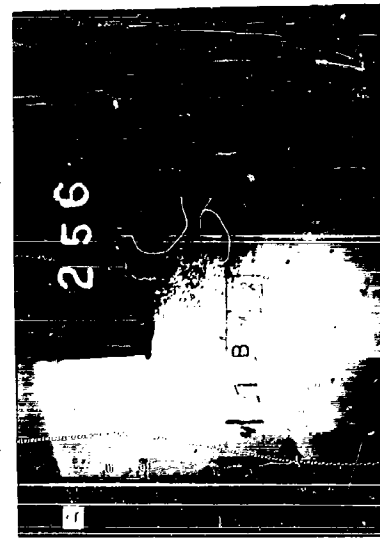


Fig. 51
 $\phi = 0^\circ$



Fig. 56
90°



Fig. 55
70°



Fig. 54
69°

Figs. 51-56. Oblique reflection of shock waves from water-air interface (6 in. diameter).

A=Initial shock wave B=Reflected wave

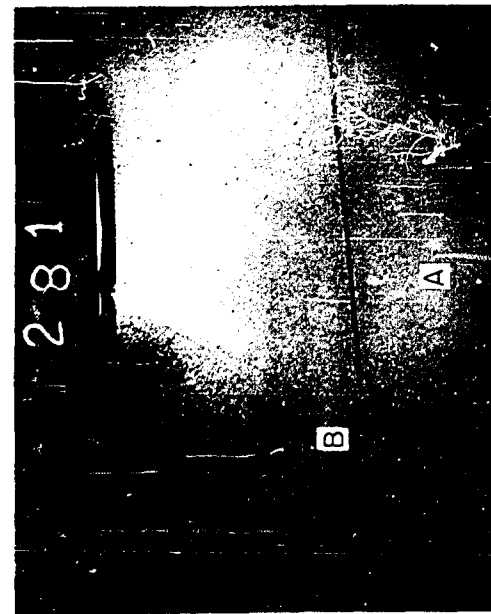


FIG. 57

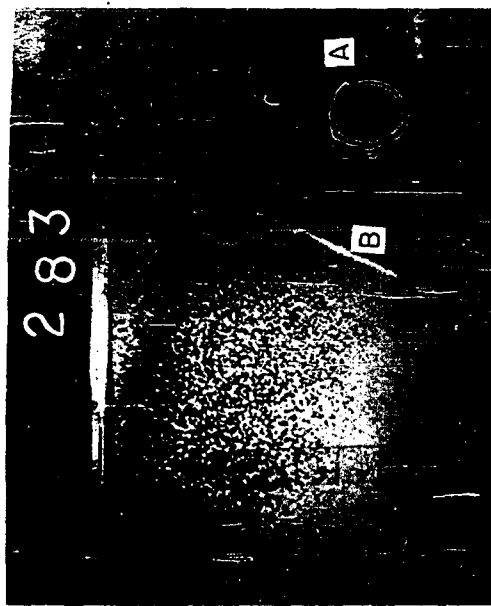


FIG. 58

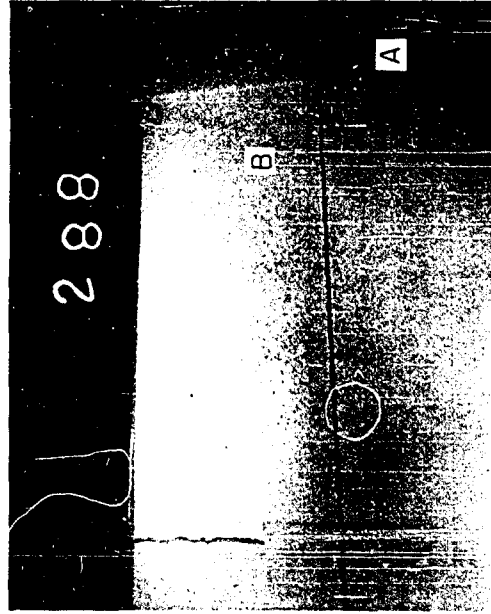


FIG. 59

CAVITATION PRODUCED BY OBLIQUE REFLECTION
OF SHOCK WAVES FROM WATER-AIR INTERFACES
A= Initial shock wave B= Reflected wave

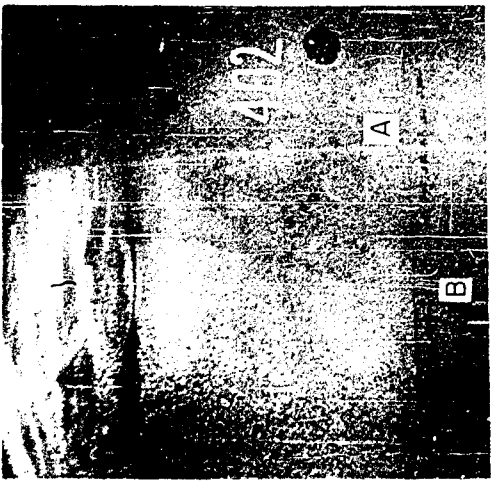


FIG. 60

Table V. Data of experiments on oblique reflection of shock waves from 20 in. by 10 in. Water-air interface, and from ocean surface.

Fig. No.	Film No.	Charge Weight (g)	Charge below surface (in.)	Charge-to-shock front (in.)	Estimated peak pressure at time of photograph (lb./in. ²)	Angle of incidence (degrees)	Surface	Qualitative description of cavitation
57	281	25	6	20	4400	73	Trough	Heavy
	282	25	4	24	3800	81	"	Heavy (Fig. 58)
58	283	250	12	45	3700	75	"	Heavy
	284	250	8	46	3600	80	"	Light (Fig. 59)
	285	25	12	45	2000	75	"	Heavy (Fig. 57)
	286	25	12	50	1800	76	"	Moderate (Fig. 60)
59	288	25	12	68	1300	80	"	Light
	289	25	12	70	1300	80	"	Moderate (Fig. 60)
	297	25	12	73	1200	81	Ocean	Moderate (Fig. 60)
	401	25	8	75	1200	84	"	Light (Fig. 60)
60	402	25	14	74	1200	79	"	Moderate

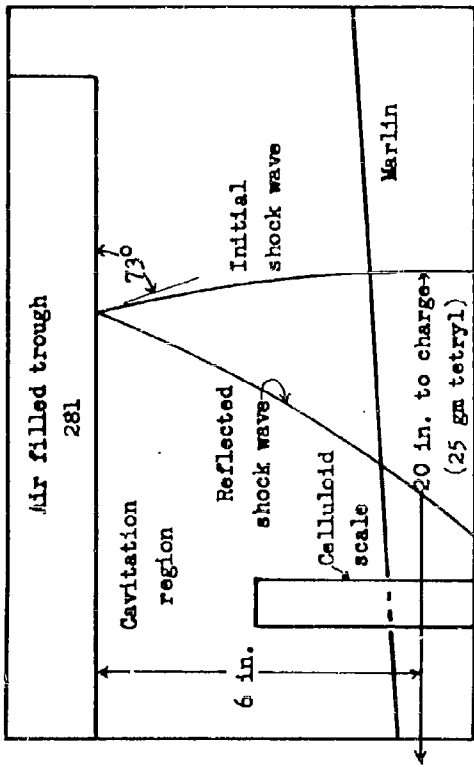


Fig. 57.

Celluloid scale - 1 in./unit

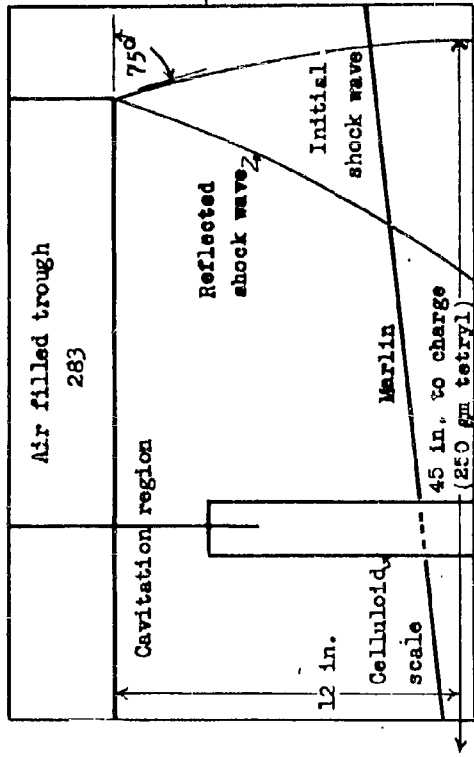


Fig. 58.

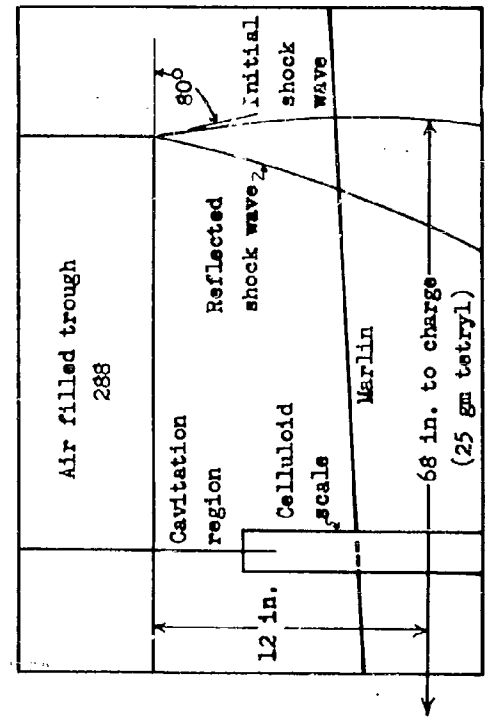


Fig. 59.

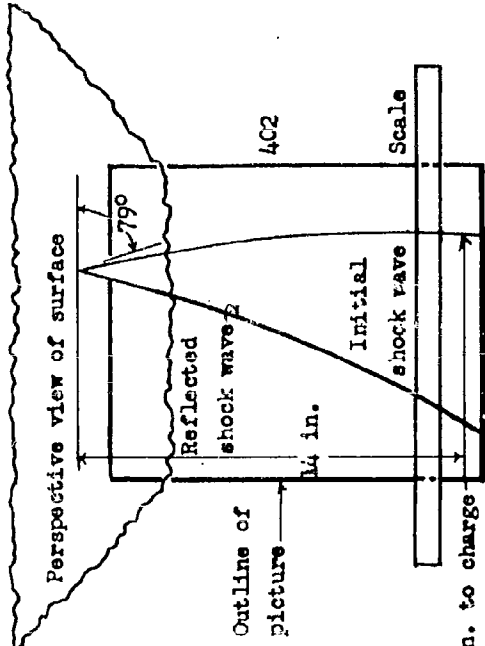


Fig. 60.

Schematic diagrams of Figs. 57, 58, 59, and 60.

Data for Figs. 61 through 67.

Spheres, 2-5/8 in. diameter Detonated at center	
Fig.	61
Estimated time after detonation (μsec)	13
Shock wave axes (in.)	
Vertical	4.6
Horizontal	4.6
Bubble axes (in.)*	
Vertical	3.7
Horizontal	3.8
Distance between inside edges of scale markings (in.)	7

Cones, 3-1/2 in. equilateral Detonated at center	
Fig.	65
Estimated time after detonation (μsec)	59
Shock wave axes (in.)	
Vertical	13.2
Horizontal	13.2
Bubble axes (in.)*	
Vertical	5.9
Horizontal	6.0
Distance between inside edges of scale markings (in.)	7

* Uncorrected for optical distortion.

2. Investigation of the effect of shape of charge and point of detonation on shock wave and bubble

Photographs (reproduced in Figures 61 to 103) of the shock wave and bubble surrounding spherical, cylindrical and conical charges weighing approximately 1/2 lb. have been taken at intervals ranging from 10 to 200 microseconds after the initiation of detonation at various points in the charges. It has been found that the shock wave tends rapidly to become spherical after it leaves the charge. A graph (Figure 105) giving bubble size as a function of shock wave radius for spherical charges of this type is also included.

The charges were all of cast pentolite and were bare except for a waterproof coating. The cylinders were cast in the following length-to-diameter ratios (keeping the weight constant): 1:1, 2:1, 4:1, 8:1. The cones were of the same weight as the cylinders and were equilateral. Timing of the detonation of the main charge and the flash charge was accomplished by the simultaneous firing of two No. 8 seismographic (SSS) DuPont caps connected in series, the delay interval being determined by a suitable length of primacord extending from one cap to the flash charge; the other cap was inserted in a well provided in the main charge. One cylinder of each shape was detonated at the center and another at one end. Of the cones, one was detonated at the apex, another at the center of the base and a third at the "center" defined as the point equidistant from the base and the conical wall. As control tests, photographs at the same time intervals were taken of cast pentolite spheres of the same weight and detonated from the center.

The experimental set-up for these shots consisted simply of the main charge, the flash charge, the camera, and occasionally a translucent diffusing screen. The main charge was suspended in front of the camera by strings cast in the charge; the flash charge was mounted on the line from the camera to the main charge, and behind the main charge as viewed from the camera. The diffusing screen, when used, was mounted between the flash charge and the main charge. For the 10 and 50 microsecond series, the distance from the camera to the main charge was about 60 in.; the distance from the main charge to the flash charge was about 24 in. For the 100 microsecond series, the distances were about 76 in. and 32 in. respectively, and for the 200 microsecond series, the distances were about 112 in. and 46 in. respectively.

In some of the spherical charge control shots, two straight steel rods 3/8" in diameter and about 6 ft. long were mounted perpendicular to the camera-charge axis and in the plane of the center of the main charge; the ends of these rods pointed toward the charge and were placed so as to be just outside the bubble at the instant of the photograph (Figures 62 - 64). Knowing the distance between the two ends, it was possible to obtain an estimate of the optical distortion of the bubble. The rods were sufficiently long so that the shock wave in the rod had not reached the far end of the rod at the instant of the photograph; hence, motion of the near end of the rod could not occur up to the instant of the photograph except by elastic compression of the rod. This amount is well under 0.1 in. in all cases. The ends of the rods were calculated from the photograph to be about 5% (2 to 8%) farther apart than they actually were which indicates that the diameter of the bubble must have been magnified by the shock wave by this amount.

The photographs are reproduced in Figures 61 to 100. The 50, 100 and 200 microsecond series are complete; the 10 microsecond series is not complete, but the pictures which are available for this time interval are presented and also some other photographs which are of interest although they do not fall into any of the four time groups. The data for each figure appear on the page opposite the figure, and include lengths of the vertical and horizontal axes of the shock wave and bubble as determined from measurements on the original negatives and the lens equations. From previous optical tests (See III, 5, d), it is believed that the shock wave axes thus determined are accurate to within one inch.

Each photograph is a double exposure due to the relatively weak flash of light given off by the main charge before detonation of the flash charge, the camera shutter being open during the whole interval. This causes an image of the original charge to appear on the film.

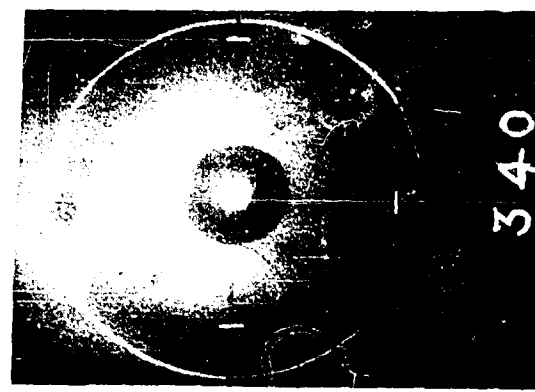


Fig. 64

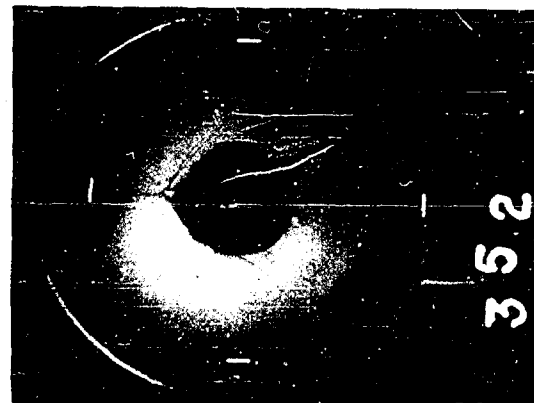


Fig. 67

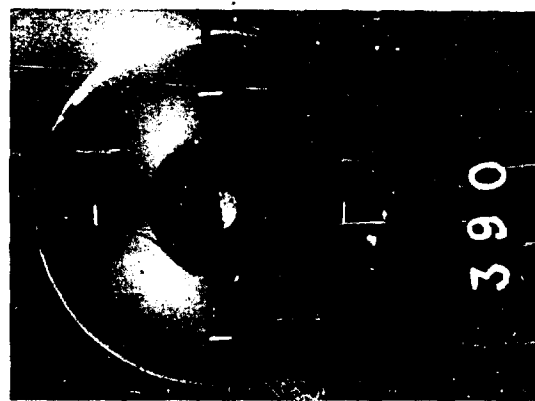


Fig. 63



Fig. 66

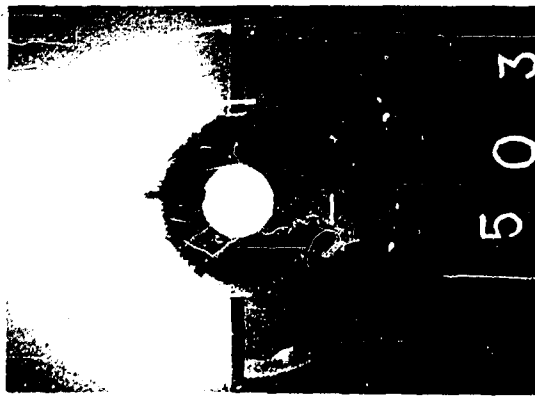


Fig. 62

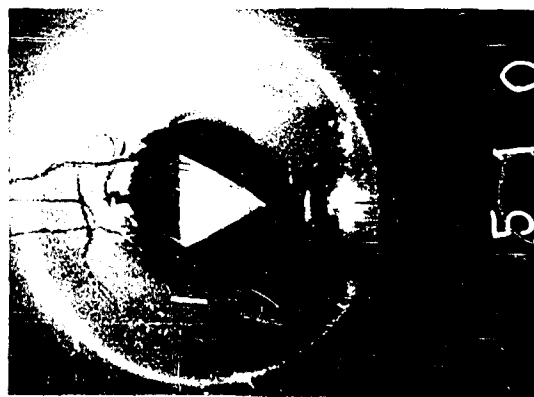
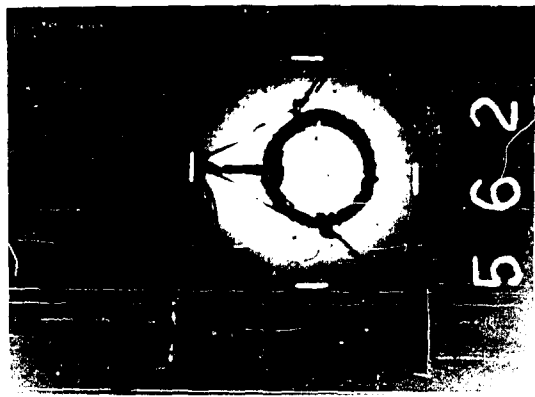


Fig. 65



Figs. 61-64 Spheres, 2 5/8 in. diam., detonated at center

Reproduced From
Best Available Copy



Fig. 7C

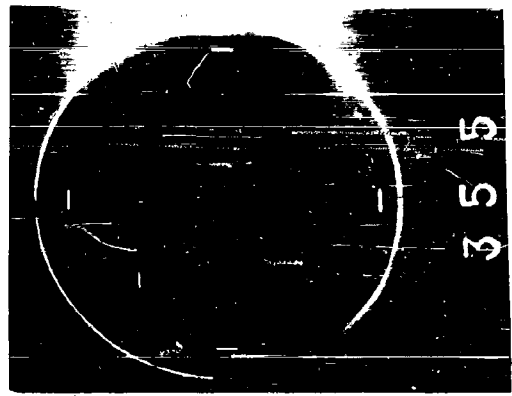


Fig. 7C



Fig. 69
Detonated at apex



Fig. 72
Detonated at center of base

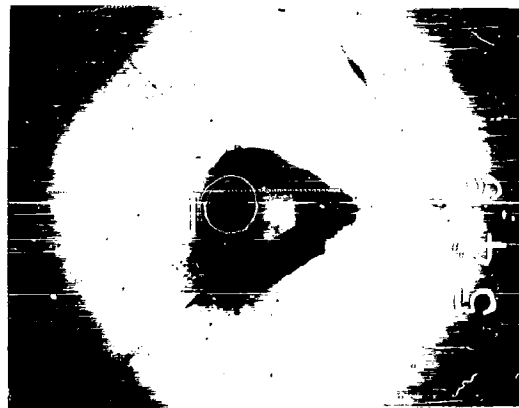


Fig. 68



Fig. 7

Figs. 68-73 Cores, 3 1/2 in equilateral

Data for Figs. 68 through 73.

Cones, 3-1/2 in. equilateral Detonated at apex		68	69	70
Fig.		46	124	215
Estimated time after detonation (μsec)				
Shock wave axes (in.)				
Vertical	11.4	22.2	33.9	
Horizontal	11.1	21.9	33.5	
Bubble axes (in.)*				
Vertical	6.0	8.6	10.7	
Horizontal	5.3	7.4	9.2	
Distance between inside edges of scale markings (in.)		7	13	26
Cones, 3-1/2 in. equilateral Detonated at center of base		71	72	73
Fig.		52	87	195
Estimated time after detonation (μsec)				
Shock wave axes (in.)				
Vertical	12.1	17.1	31.2	
Horizontal	12.2	17.0	31.2	
Bubble axes (in.)*				
Vertical	5.8	7.0	9.8	
Horizontal	6.4	6.9	9.3	
Distance between inside edges of scale markings (in.)		7	13	26

* Uncorrected for optical distortion.

Data for Figs. 74 through 80.

Cylinders, 2-1/2 in. diameter, 2-1/2 in. long
Detonated at center

Fig.	Estimated time after detonation (sec)	74	75	76	77
Shock wave axes (in.)					
Vertical	-		11.4	20.5	30.8
Horizontal	-		11.1	20.8	30.8
Bubble axes (in.)*					
Vertical	-	5.4	8.1	8.9	
Horizontal	-	5.2	7.2	8.8	
Distance between inside edges of scale markings (in.)		7	13	13	26

Cylinders, 2-1/2 in. diameter, 2-1/2 in. long
Detonated at top end

Fig.	Estimated time after detonation (sec)	78	79	80
Shock wave axes (in.)				
Vertical	-	11.7	19.7	32.3
Horizontal	-	10.9	19.6	32.5
Bubble axes (in.)*				
Vertical	-	6.5	8.0	9.6
Horizontal	-	5.2	6.9	9.8
Distance between inside edges of scale markings (in.)		7	13	26

* Uncorrected for optical distortion.

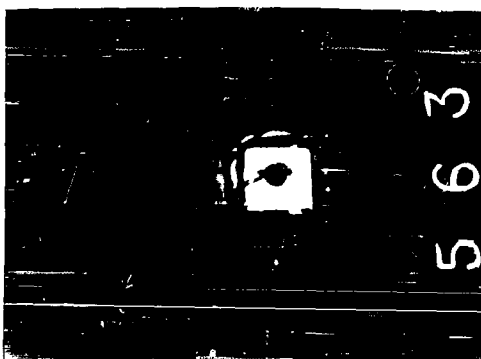
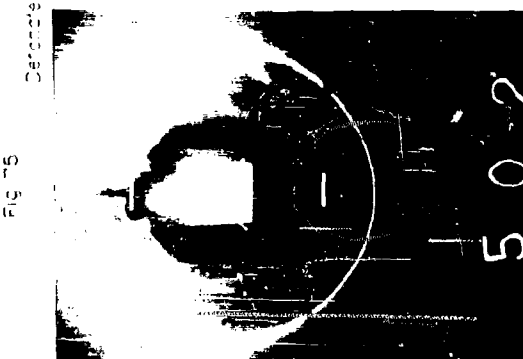
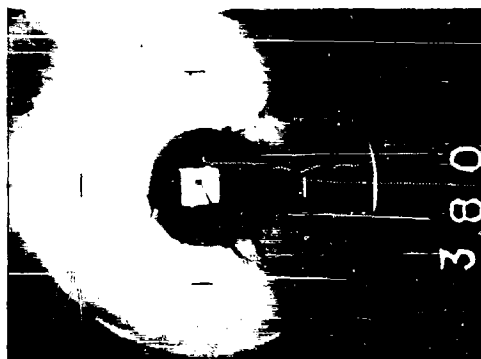


Fig. 75

Fig. 75

Detached at top end

Fig. 76

Fig. 76

Cylinders, 2 1/2 in diam, 2 1/2 in long

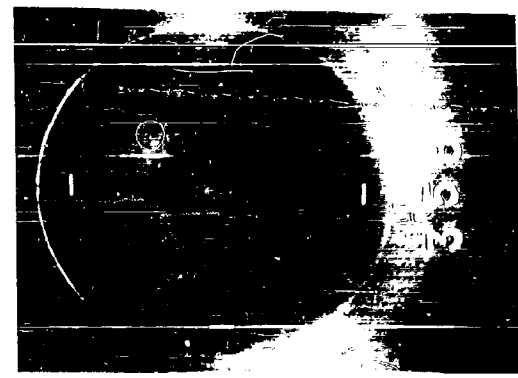


Fig. 82
Detonated at center

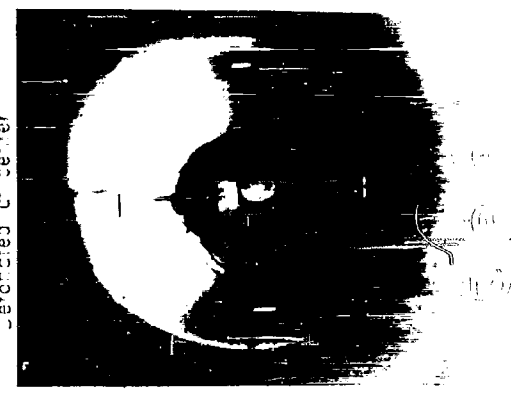


Fig. 85
Detonated at top end

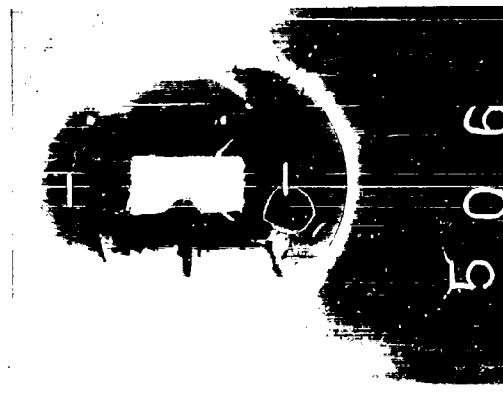


Fig. 81



Fig. 34

Figs. 81-86
Cylinders, 1 3/4 in diam. 3 1/2 in long

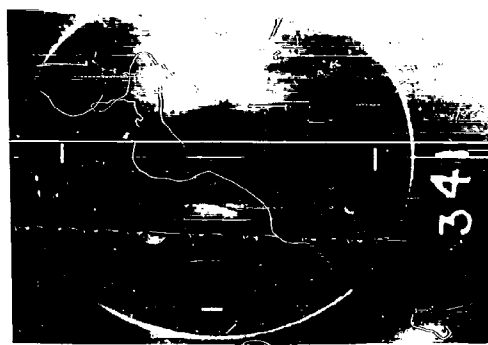


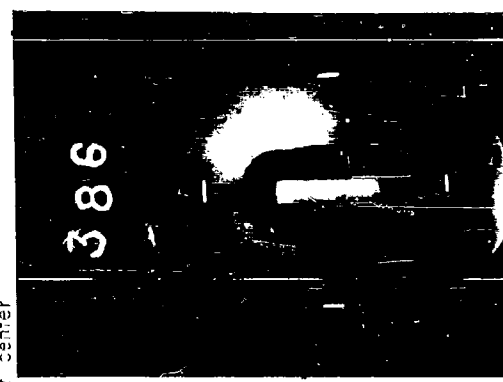
Fig 82



345



Fig 83



Detonated at center

Fig 92

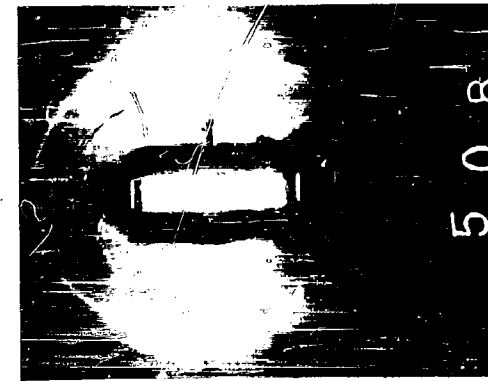


Fig 87

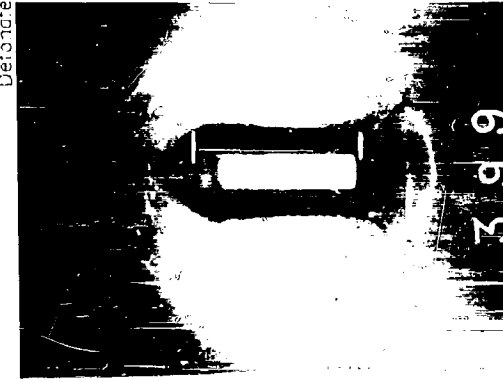


Fig 91

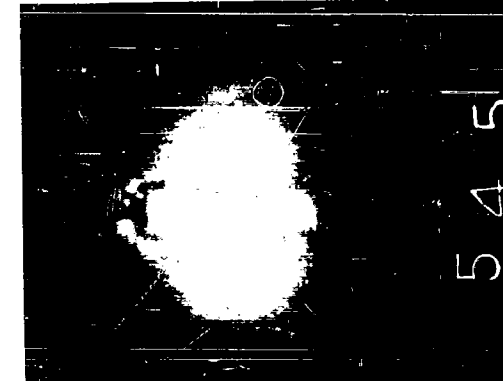


Fig 93

Figs 87-93 Cylinders. 1 7/16 in diam, 5 7/8 in long

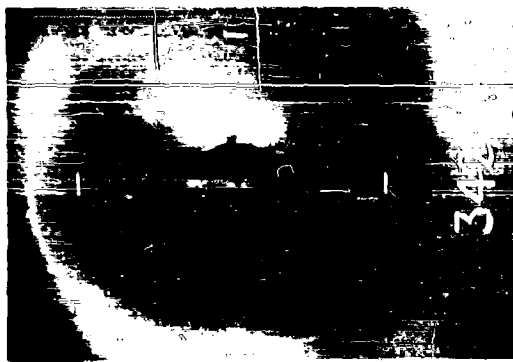


Fig. 97



Fig. 96

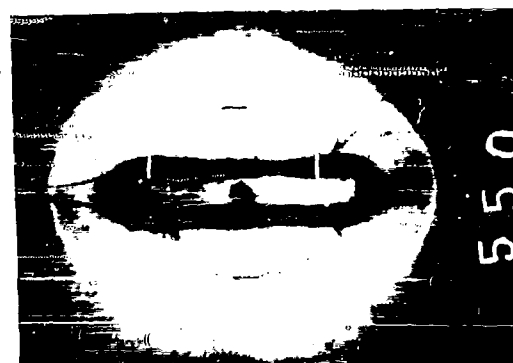


Fig. 95
Detonated at Center

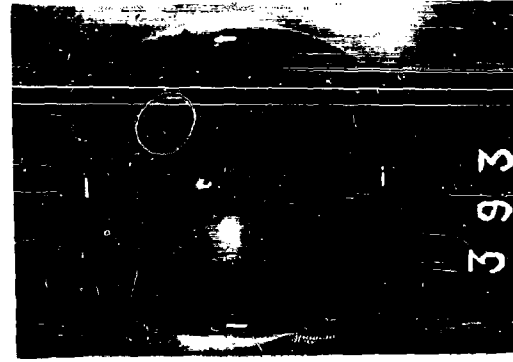
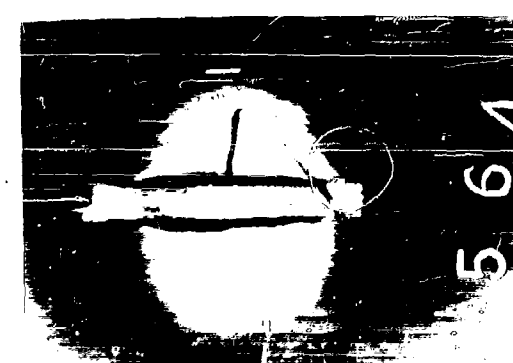


Fig. 100

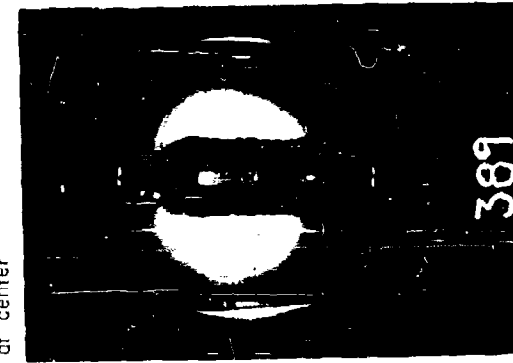


Fig. 99

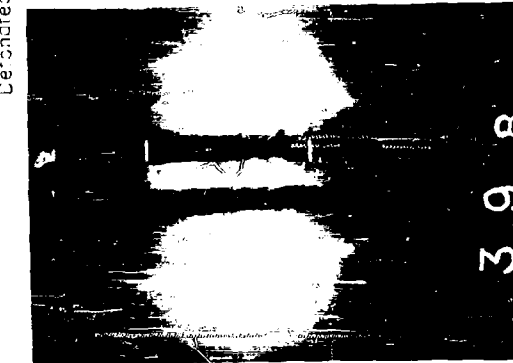


Fig. 98

Fig. 95 Detonated at top end
Figs. 94-100 Cylinders, $1\frac{1}{8}$ in. diam., 2 in. long

Date for FIGS. 81 through 86.

Cylinders, 1-3/4 in. diameter, 3-1/2 in. long Detonated at center		81	82	83
Fig.		37	111	193
Estimated time after detonation (μsec)				
Shock wave axes (in.)		10.7 8.9	20.7 19.5	31.3 30.8
Vertical				
Horizontal				
Bubble axes (in.)*		6.4 4.3	8.4 6.6	10.0 8.6
Vertical				
Horizontal				
Distance between inside edges of scale markings (in.)		7	13	26
Cylinders, 1-3/4 in. diameter, 3-1/2 in. long Detonated at top end		84	85	86
Fig.		50	91	196
Estimated time after detonation (μsec)				
Shock wave axes (in.)		12.7 11.3	17.9 16.8	31.8 31.1
Vertical				
Horizontal				
Bubble axes (in.)*		7.2 4.7	8.2 5.3	10.6 8.0
Vertical				
Horizontal				
Distance between inside edges of scale markings (in.)		7	13	26

* Uncorrected for optical distortion.

Data for Figs. 87 through 93.

Cylinders, 1-7/16 in. diameter, 5-7/8 in. long
Detonated at center

Fig.	Estimated time after detonation (μsec)	Shock wave axes (in.)	Bubble axes (in.)*	Distance between inside edges of scale markings (in.)	
87	61	15.5 11.8	21.1 18.0	88	89
88	107			107	207
89					
90	91	14.4 10.5	20.2 17.5	92	93
91	54	2.4		101	207
92					
93					

Cylinders, 1-7/16 in. diameter, 5-7/8 in. long
Detonated at top end

Fig.	Estimated time after detonation (μsec)	Shock wave axes (in.)	Bubble axes (in.)*	Distance between inside edges of scale markings (in.)	
90	10	10.5	17.5	7	26
91		14.4	20.2	7	
92		2.4		13	
93					
94					
95					
96					
97					
98					
99					
100					
101					
102					
103					
104					
105					
106					
107					
108					
109					
110					
111					
112					
113					
114					
115					
116					
117					
118					
119					
120					
121					
122					
123					
124					
125					
126					
127					
128					
129					
130					
131					
132					
133					
134					
135					
136					
137					
138					
139					
140					
141					
142					
143					
144					
145					
146					
147					
148					
149					
150					
151					
152					
153					
154					
155					
156					
157					
158					
159					
160					
161					
162					
163					
164					
165					
166					
167					
168					
169					
170					
171					
172					
173					
174					
175					
176					
177					
178					
179					
180					
181					
182					
183					
184					
185					
186					
187					
188					
189					
190					
191					
192					
193					
194					
195					
196					
197					
198					
199					
200					
201					
202					
203					
204					
205					
206					
207					
208					
209					
210					
211					
212					
213					
214					
215					
216					
217					
218					
219					
220					
221					
222					
223					
224					
225					
226					
227					
228					
229					
230					
231					
232					
233					
234					
235					
236					
237					
238					
239					
240					
241					
242					
243					
244					
245					
246					
247					
248					
249					
250					
251					
252					
253					
254					
255					
256					
257					
258					
259					
260					
261					
262					
263					
264					
265					
266					
267					
268					
269					
270					
271					
272					
273					
274					
275					
276					
277					
278					
279					
280					
281					
282					
283					
284					
285					
286					
287					
288					
289					
290					
291					
292					
293					
294					
295					
296					
297					
298					
299					
300					
301					
302					
303					
304					
305					
306					
307					
308					
309					
310					
311					
312					
313					
314					
315					
316					
317					
318					
319					
320					
321					
322					
323					
324					
325					
326					
327					
328					
329					
330					
331					
332					
333					
334					
335					
336					
337					
338					
339					
340					
341					
342					
343					
344					
345					
346					
347					
348					
349					
350					
351					
352					
353					
354					
355					
356					
357					
358					
359					
360					
361					
362					
363					
364					
365					
366					
367					
368					
369					
370					
371					
372					
373					
374					
375					
376					
377					
378					
379					
380					
381					
382					
383					
384					
385					
386					
387					
388					
389					
390					
391					
392					
393					
394					
395					
396					
397					
398					
399					
400					
401					
402					
403					
404					
405					
406					
407					
408					
409					
410					
411					
412					
413					
414					
415					
416					
417					

Data for Figs. 94 through 100

Cylinders, 1-1/8 in. diameter, 9 in. long						
Detonated at center						
Fig.	94	95	96	97	203	
Estimated time after detonation (μ sec)	11	60	120			
Shock wave axes (in.)						
Vertical	3.3	16.6	24.4	34.6		
Horizontal		10.2	18.5	29.7		
Bubble axes (in.)*						
Vertical		12.1	13.2	14.7		
Horizontal		3.7	5.2	6.9		
Distance between inside edges of scale markings (in.)	7	7	13	26		
Cylinders, 1-1/8 in. diameter, 9 in. long						
Detonated at top end						
Fig.	98	99	99	100	198	
Estimated time after detonation (μ sec)	56	94	94			
Shock wave axes (in.)						
Vertical	15.9	20.6	20.6	33.8		
Horizontal	9.9	14.9	14.9	29.3		
Bubble axes (in.)*						
Vertical	11.6	12.5	12.5	14.2		
Horizontal	3.5	4.2	4.2	6.1		
Distance between inside edges of scale markings (in.)	7	7	13	26		

* Uncorrected for optical distortion.

Data for Figs. 101 through 104: Miscellaneous Photographs

Fig.	101	102
Cylinder; diameter (in.) length (in.)	2-1/2 2-1/2	1-1/8 9
Detonated at center		
Estimated time after detonation (μ sec)	25	83
Shock wave axes (in.)		
Vertical	8.0	19.4
Horizontal	7.7	13.1
Bubble axes (in.) *		
Vertical	4.9	12.7
Horizontal	5.4	4.2
Distance between inside edges of scale markings (in.)	7	13

Fig. 103

Cylinder; diameter (in.) 1-3/4.
length (in.) 3-1/2.

Detonated at top end.

Shock wave just emerging from top.

Fig. 104

Flash photograph following
detonation of Ensign-Bickford
primacord.

* Uncorrected for optical distortion.

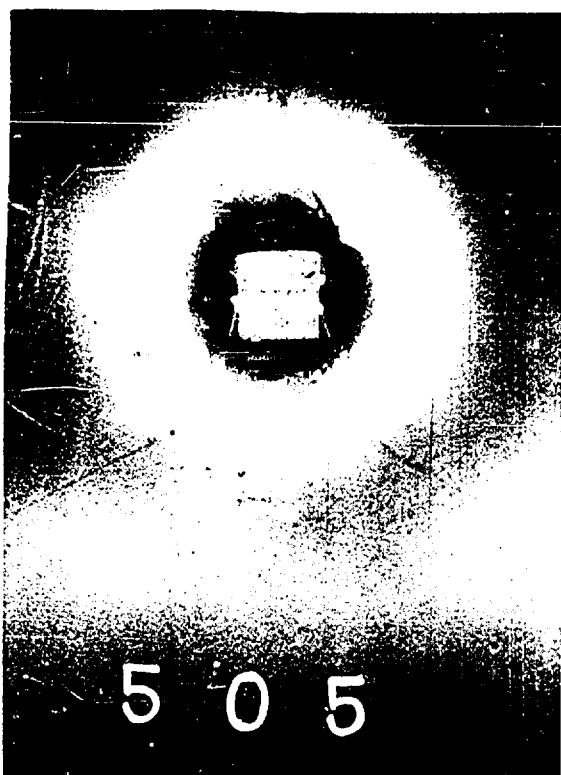


Fig. 101



Fig. 102

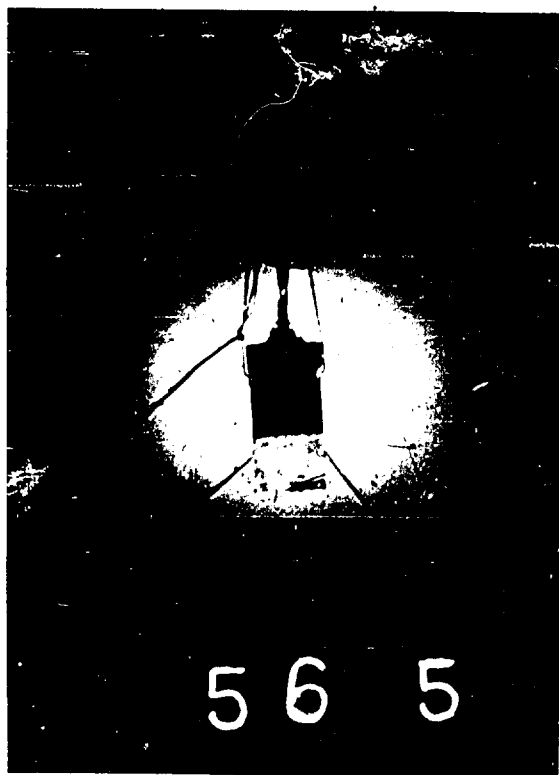


Fig. 103



Fig. 104

Figs 101-104 Miscellaneous photographs

Because of distortion occurring in reproduction, horizontal and vertical scales are provided in the photographs in the form of black or white lines drawn on the prints. The distances between the inside edges of the lines corresponds in the actual experiments to 7 in. in the 10 and 50 microsecond series pictures and the miscellaneous photographs, to 13 in. in the 100 microsec. series and to 26 in. in the 200 microsec. series.

The pieces of some of the longer cylindrical charges which had been broken in handling were rejoined after fusion at the points of fracture. It is interesting to note that the remelted parts are visible in the photographs. In many of the photographs, twine, pieces of detonator wire, and part of the detonator itself are visible in addition to the charge, bubble, and shock wave.

The focal length of the camera lens was determined at two distances by photographing a grid underwater so that calculations based on the lens equations could be made. In so doing, it was found that the lens used gave some "pincushion" distortion of rectangular objects, but this distortion is not sufficient to change the relative axial lengths by an amount greater than 0.6 in.

Figure 105 shows the relation between bubble radius and shock wave radius for 1/2 lb. spherical charges of cast pentolite. Since the time intervals for these shots can be estimated from the positions of the shock waves, an approximate time scale is also included.

Figure 106 indicates the rates at which the shock waves from the asymmetric cylindrical charges approach a spherical shape.

3. Pressure and time-constant measurements of shock waves by optical distortion.

Several photographic methods have been developed which allow calculation of the peak pressure of a shock wave, and for one of these methods the calculations have been extended to make possible an evaluation of the time constant of the shock wave. These methods make use of the fact that light rays passing through a shock wave at favorable angles are considerably distorted due to the increase of refractive index in the region of high pressure. A detailed theoretical discussion of these methods is to be found in Appendix II.

(a) Spherical shock wave; charge not on the optical axis; charge in grid plane. -- The arrangement with which most of the work has been done involves placing a transparent lucite grid marked off with lines 1/4 in. apart in front of the camera, and the shock-wave-producing charge off to one side and in the same plane with the grid. (See Figure 133, Appendix II.) A flash charge is placed behind the grid and is timed by means of primacord to go off when the shock wave from the main charge is crossing the grid. The results of both peak pressure and time-constant determinations from four shots using this method agree essentially with UERL piezoelectric results for similar conditions.

(i) Peak pressure. Two of these four shots were made with 250 gm tetryl as the main charge, and the photographs were taken when the shock wave radius was about 15 in. One of these photographs is reproduced in Figure 107. The theory (Appendix II.1) relates the amount of apparent displacement of an individual intersection of grid lines with the average refractive index of that section of the shock wave through which the corresponding light ray must pass. This average refractive index is then converted to the corresponding pressure, P_{av} . This calculation is made for several grid intersections at different radii. Plotting (on semi-log paper) $\log P_{av}$ against the corresponding distances of the mid-points of the refracted light rays behind the shock front, $(|R| - r_{av})$, a straight line is obtained to within the precision of measurement. Figure 108 is such a plot for a shock wave 14.9 in. from a 250 gm tetryl charge, while Figs. 109 and 110 are the results of measurements on two different prints of another shock wave 14.4 in. from 250 gm tetryl. The average deviations from the straight lines drawn are approximately 7%, 6%, and 3%, respectively. The peak pressure is assumed to be the extrapolation of this line to zero distance behind the front. Any errors introduced by assumption that the calculated P_{av} 's correspond to the

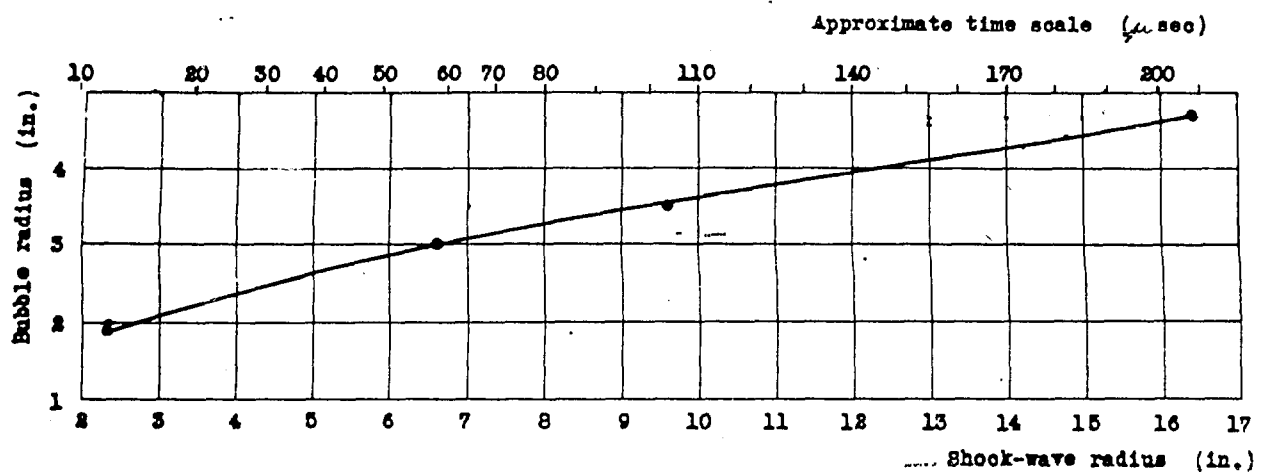


Fig. 105. Bubble radius vs. shock-wave radius for $\frac{1}{2}$ lb cast pentolite (spherical charge).

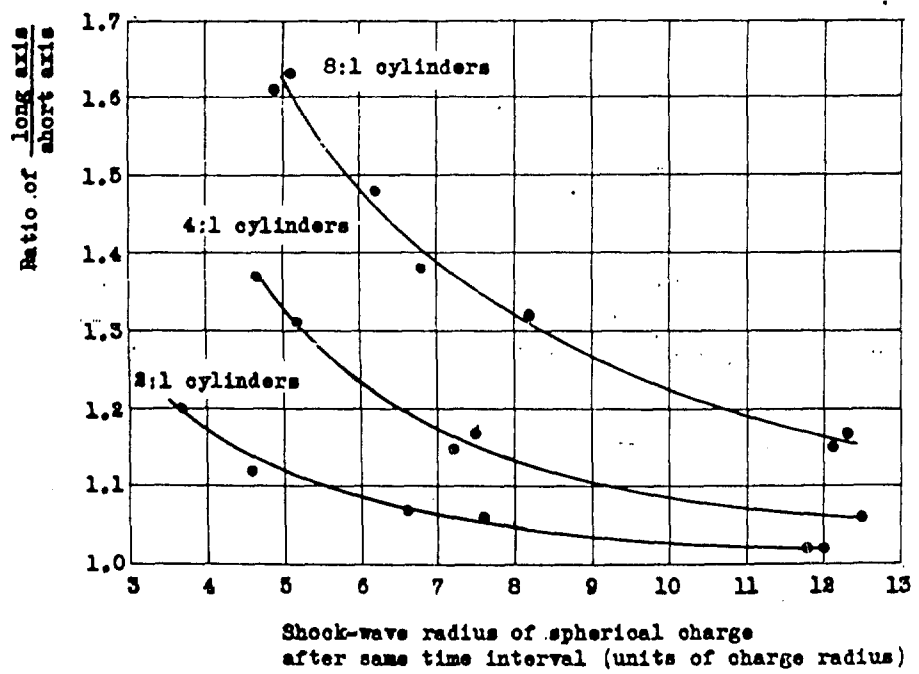


Fig. 106. Ratios of long axis to short axis of shock waves from asymmetric cylinders vs. shock-wave radius (in charge radii) for spherical charge of same weight and after same time.

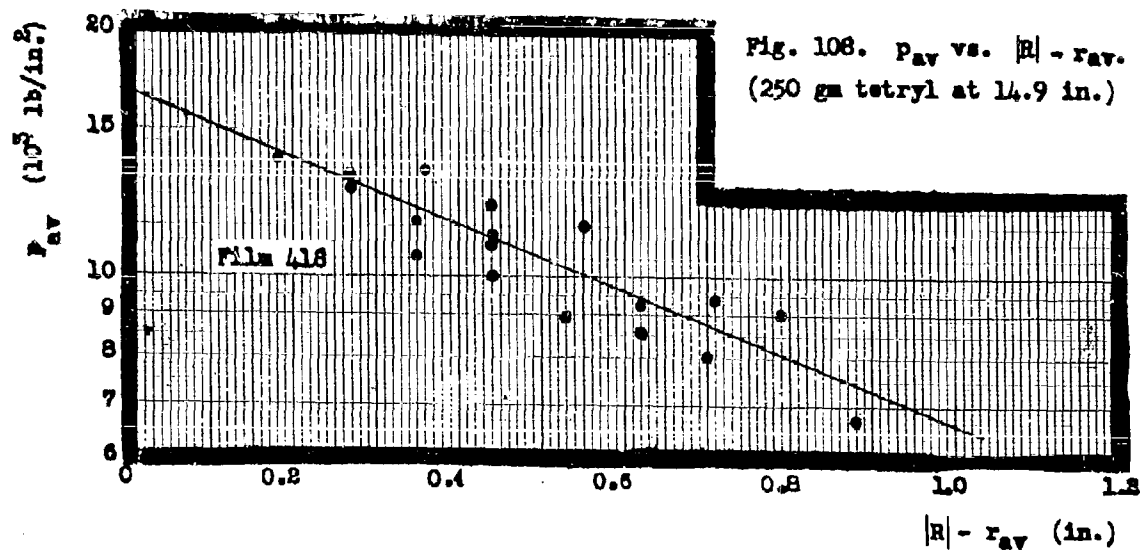


Fig. 108. P_{av} vs. $|R| - r_{av}$.
(250 gm tetryl at 14.9 in.)

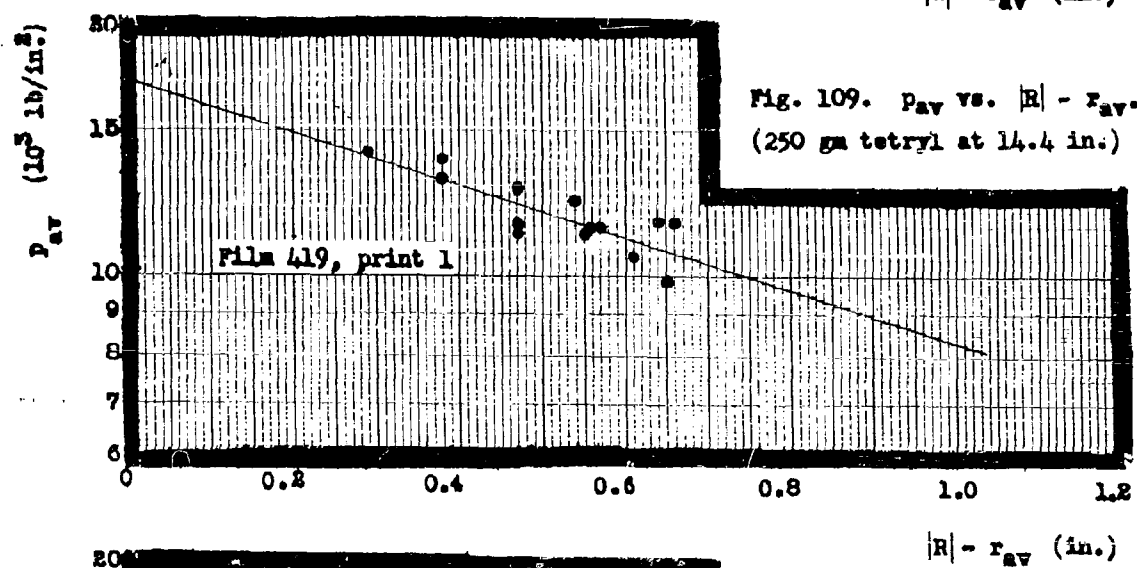


Fig. 109. P_{av} vs. $|R| - r_{av}$.
(250 gm tetryl at 14.4 in.)

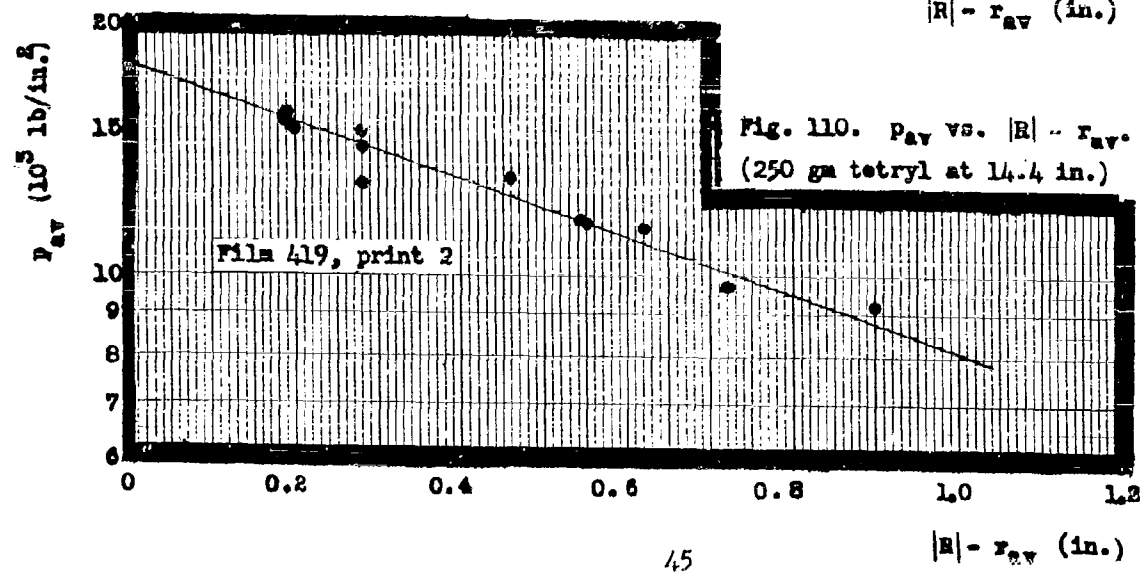
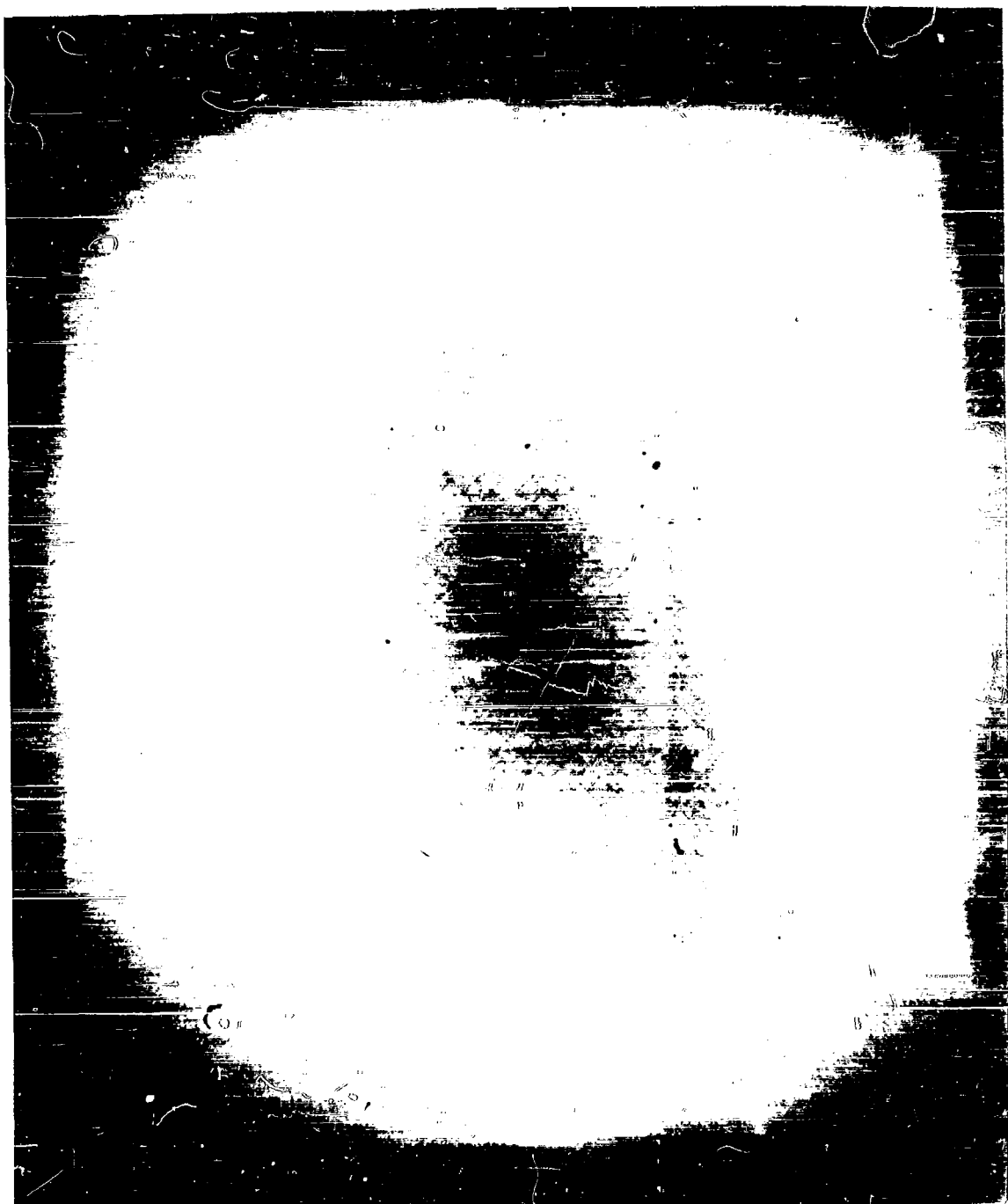


Fig. 110. P_{av} vs. $|R| - r_{av}$.
(250 gm tetryl at 14.4 in.)

Fig. 107 Typical example of optical distortion photograph. Film 418- 250 gm tetryl at 14.9 in



points of mean distance of the light rays behind the shock front should go to zero in this limit. The peak pressure obtained from two prints of the same shot (Figures 109 and 110) agree to within 4.5% (17,200 and 18,000 lbs./in.²). Correcting the result from Figure 108 ($P_{max} = 16,700$ lbs./in.²) to a shock wave radius of 14.4 in., using a distance exponent of 1.13, one obtains a pressure of 17,400 lbs./in.², which agrees with the average of Figures 109 and 110 to within 1.5%.

This method of peak pressure determination was also applied successfully to the other two shots, consisting of ca. the equivalent of ca. 364 gm TNT and using a shock wave radius of ca. 16 in. Measurements were made at several pairs of grid line intersections for each of the two films. The values of $\log P_{av}$ were plotted against $(|R| - r_{av})$ as before and one straight line was drawn through the data from both films, since the value of $|R|$, the shock wave radius, for the two films was identical. Extrapolation of this line to $|R| - r_{av} = 0$ gave a value for P_{max} of 17,050 lbs./in.². This plot is given in Figure 111. The average deviation of the points from the straight line is ca 5.5%, with no systematic difference between the points for the two shots.

(ii) Time-constants. The results for the two torpex shots were also used for calculation of time-constants of the shock wave. Since the detailed development of the theory, together with a sample calculation, is given in Appendix II, only the results will be reported here. In general, the calculations are considerably more tedious than for the peak pressures.

Five points were used in the calculations, two from one shot and three from the other. The ones whose images were the clearest, and thus the most accurately measured, were selected. They were picked from the plot of Figure 111 at different values of $(|R| - r_{av})$ and at different deviations from the line. The results of the calculations are shown in Table VI.

Table VI. Results in the evaluation of time constant.

Film No.	Point No.	$ R - r_{av}$ (in.)	θ_r (in.)	$r' - D_r$ (in.)	θ_t (μ sec)
536	22	0.61	3.15	14.76	39.1
537	5a	0.63	3.39	14.72	41.3
537	12	0.94	3.23	14.11	39.6
536	8	0.97	3.68	14.03	43.8
537	18	1.13	3.09	13.71	38.1

Av. $\theta_t = 40.4$ μ sec, average deviation from mean = 1.7 μ sec.

It will be noted that there is no systematic trend of θ_t with distance of the point selected for calculation behind the shock front ($|R| - r_{av}$).

(iii) Summary and remarks. As shown in Figure 111, the peak pressure of the shock wave produced by ca. 364 gm TNT at 16.0 in. is 17,050 lbs./in.². The results for both peak pressure and time constant are in essential agreement with piezoelectric results obtained at UERL both for small bare charges and depth bombs (scaled down). The agreement is within the accuracy of either method for these experimental conditions (ca 10%).

This experimental method has the disadvantage that the results obtained are rather sensitive to the geometry of the experiment. For example, to obtain the desired accuracy for these shots, the point at which the line from the camera lens, perpendicular to the grid, intersected the grid had to be determined in the actual set-up to within 1/16 in. For this reason, a single rigid frame had to be used to support the camera, the main charge, and the grid. It has been demonstrated, however, that the method is satisfactory if the experiment is carefully set up.

Further experiments in fresh water for comparison with those made in salt water should be done.

(b) Spherical shock wave; charge on the optical axis; charge in grid plane. -- The theory for peak pressure determination has been worked out for an experimental arrangement similar to that of Section (a) except that now the charge is located directly in front of the camera (See Appendix II, 2). Figure 112 (Film 526) shows a photograph obtained according to this method.

(c) Non-spherical shock wave; charge on the optical axis; charge in grid plane. -- The theory for peak pressure determination has also been worked out for an experimental arrangement similar to that of Section 3(b) except that the shock wave surface is not required to be spherical, but expressible only by some definite equation of the form $f(x, y, z) = 0$ (See Appendix II, 3).

(d) Spherical shock wave; charge on the optical axis; charge in front of grid plane. -- Partly to increase the amounts of distortion measured on the photograph, and thus improve the precision of the measurements, and partly in an effort to find an experimental arrangement in which less precision would be necessary in setting up the apparatus, one photograph (reproduced in Figure 113 (Film 531)) has been taken in which the grid was mounted in back of the charge, as viewed from the camera. Inspection of Figure 138 in Appendix II, 4 will show how the measured distortion is increased by allowing the refracted ray, (considered as projected backwards) to traverse a greater distance than in the other experimental set-ups. Another evident advantage of this arrangement is that at the time of the photograph the shock wave need not have reached the grid, so that there is no danger of mechanical distortion of the grid.

In this particular shot, the charge was 250 gm cast pentolite and was placed 51 in. in front of the camera. The grid was positioned 8 in. behind the charge, and a flash charge 28 in. behind the grid. Since the charge and grid are at different distances from the camera, both the shock wave and the grid cannot be in perfect focus, but this is not likely to be troublesome if a reasonably small lens aperture is used.

Not enough work has been done using this method to warrant a comparison with the method described in Section III, 3, (a).

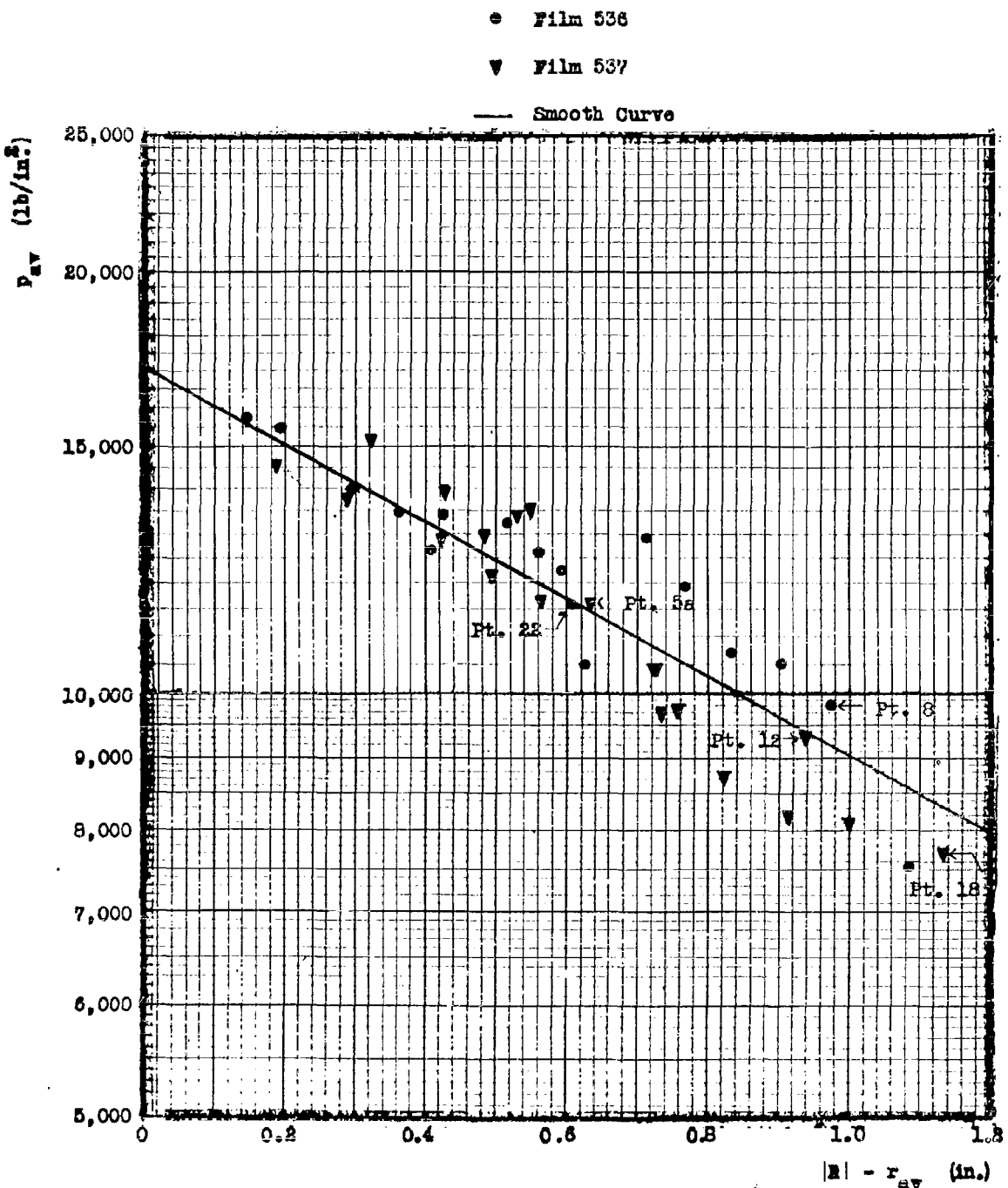


Fig. III. p_{av} vs. $|R| - r_{av}$ for shock waves produced by two charges of ca. 364 gm TNT at a value of $|R|$ of 16 in.

OPTICAL DISTORTION PHOTOGRAPHS

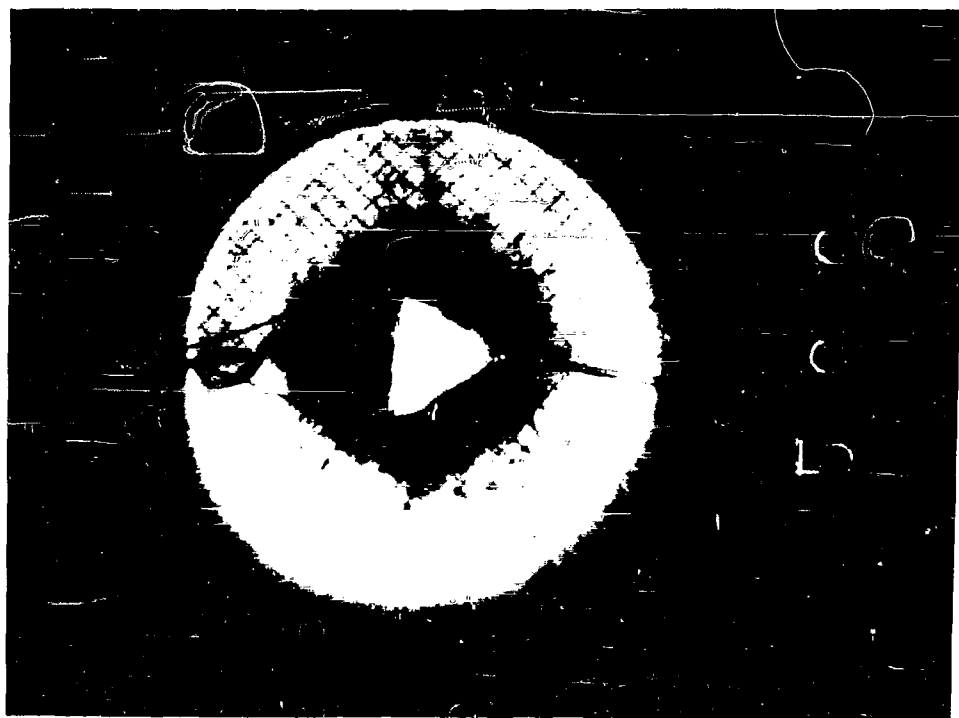


Fig. 112. Spherical shock wave; charge on the optical axis; charge in grid plane.

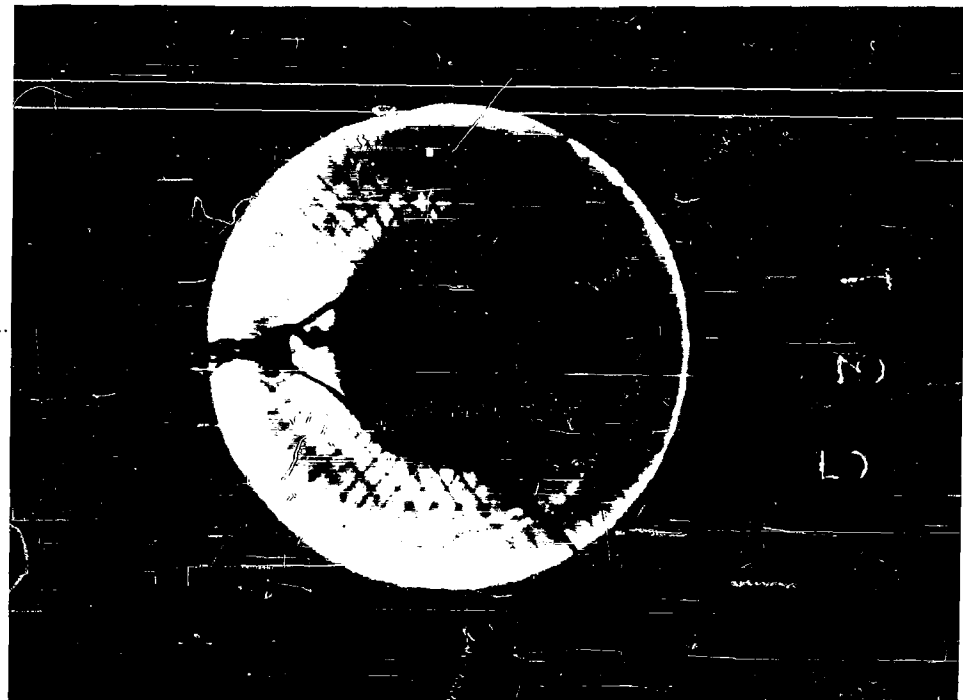


Fig. 113. Spherical shock wave; charge on the optical axis; charge in front of grid plane.

4. Cylinder Damage 8/

(a) Introduction. -- After some of the early UERL experiments on damage to cylindrical targets by explosions, it became apparent that bubble pressure was contributing to a considerable extent to the damage. Since bubble damage does not scale in the same manner as shock-wave damage and since the gross damage is the result of both bubble and shock wave damage, a preliminary step in the interpretation of the cylinder results is the separation of shock wave and bubble pulse damage. The easiest way to effect this separation is by photography.

(b) Still pictures. -- Preliminary still photographs taken between the time of impact of the shock wave and the first bubble pulse showed that damage was by no means complete compared with the final condition of the cylinder. These pictures, some of which are shown in Figures 114, 115, 116, were taken with a photoflash lamp so that the act of photographing the cylinders does not contribute to the damage.

(c) Slow speed movies. -- Some motion pictures were then taken with the Victor camera of 3 simple, small cylindrical shells of the S type 8/ and one unsupported cylinder of the SA type being damaged by a 25 gm charge. These showed that the unsupported cylinder was practically undamaged until the time of the first bubble pulse and was damaged by both the first and second pulses. The supported cylinder, on the other hand, was damaged essentially completely by the shock wave.

(d) High speed movies. -- Still another series of experiments was performed with SD class cylinders at depths of 200, 400 and 580 ft. The photographs were taken with the Eastman high speed camera with #31 photoflash lamps for lighting. The apparatus shown in Figure 116 was used. A representative film is reproduced in Figure 117. It shows that the cylinder was relatively stable after it was damaged by the shock wave but collapsed completely soon after the bubble pulse. This sequence of events was not followed for closer shots; in some of the latter, instability resulted from shock wave damage.

The sharpness of this series is due to the unusual clarity of the Bahamas water in which the pictures were taken. The Secchi disk reading was about 135 ft.

A complete description of the cylinder results will be given in a forthcoming report. 8/

5. Miscellaneous experiments

(a) Mach effect. -- Three pictures were taken of intersecting shock waves having a peak pressure about 700 times hydrostatic pressure ($\sim 9,500$ lb./in.²). In two cases the intersection was obtained by reflecting the shock wave from a 50 gm tetryl charge off a 1/2 in. steel plate 12 in. away, and in the third case, by the shock waves from two appropriately placed 50 gm charges. (See Figure 118). In all three shots, the charges were approximately 12 in. from the point of intersection of the shock waves. The resulting pictures are Figures 119, 120, and 121. The angle of intersection of the shock waves shown is 64°, 71°, and 71° respectively. The Mach effect appears quite strongly in the last two cases. A fourth picture with an angle of intersection of 45° is presented for comparison in Figure 122. This angle is outside the Mach region and no Mach effect shows although the appearance of the shock waves is somewhat distorted due to refractive index discontinuity.

(b) Shock wave from 300 lb. charge. -- A single flash picture of the shock wave from a 300 lb. charge was taken in the Bahamas at a distance of 65 ft. and is presented in Figure 123 to show the possibilities for full scale photography in clear water. Although lack of time prevented us from following up this promising lead, it is

8/ These cylinders are described in a report by J. C. Decius and P. M. Fye, Damage to Thin Steel Cylindrical Shells by Underwater Explosions, NDRC Report No. A-369, OSRD No. 6247.

BEFORE BUBBLE PULSE

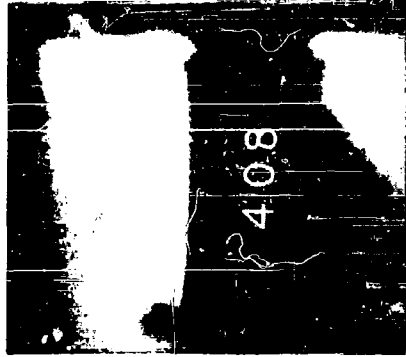


Fig. 114 A
 $T \approx 55$ $T_B - T \approx 20$
 $T_B = 75$ millisecond

LONG AFTER BUBBLE PULSE

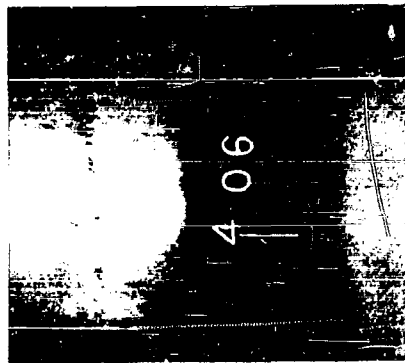


Fig. 115 A
 $T \approx 40$ $T_B - T \approx 35$
 $T_B = 75$ millisecond

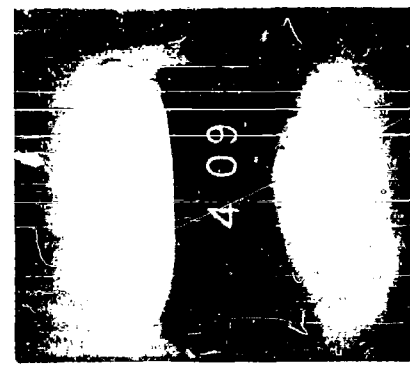


Fig. 116 A
 $T \approx 65$ $T_B - T \approx 35$
 $T_B = 75$ millisecond

Fig. 114 B

$T =$ TIME AFTER EXPLOSION: MILLISEC.

Fig. 115 B

$T_B =$ CALCULATED TIME OF BUBBLE PULSE: 75 MILLISEC.

Fig. 116 B

DAMAGE TO CYLINDERS BEFORE AND AFTER CALCULATED TIME OF BUBBLE PULSE

UNIT OF TIME = 1 MSEC

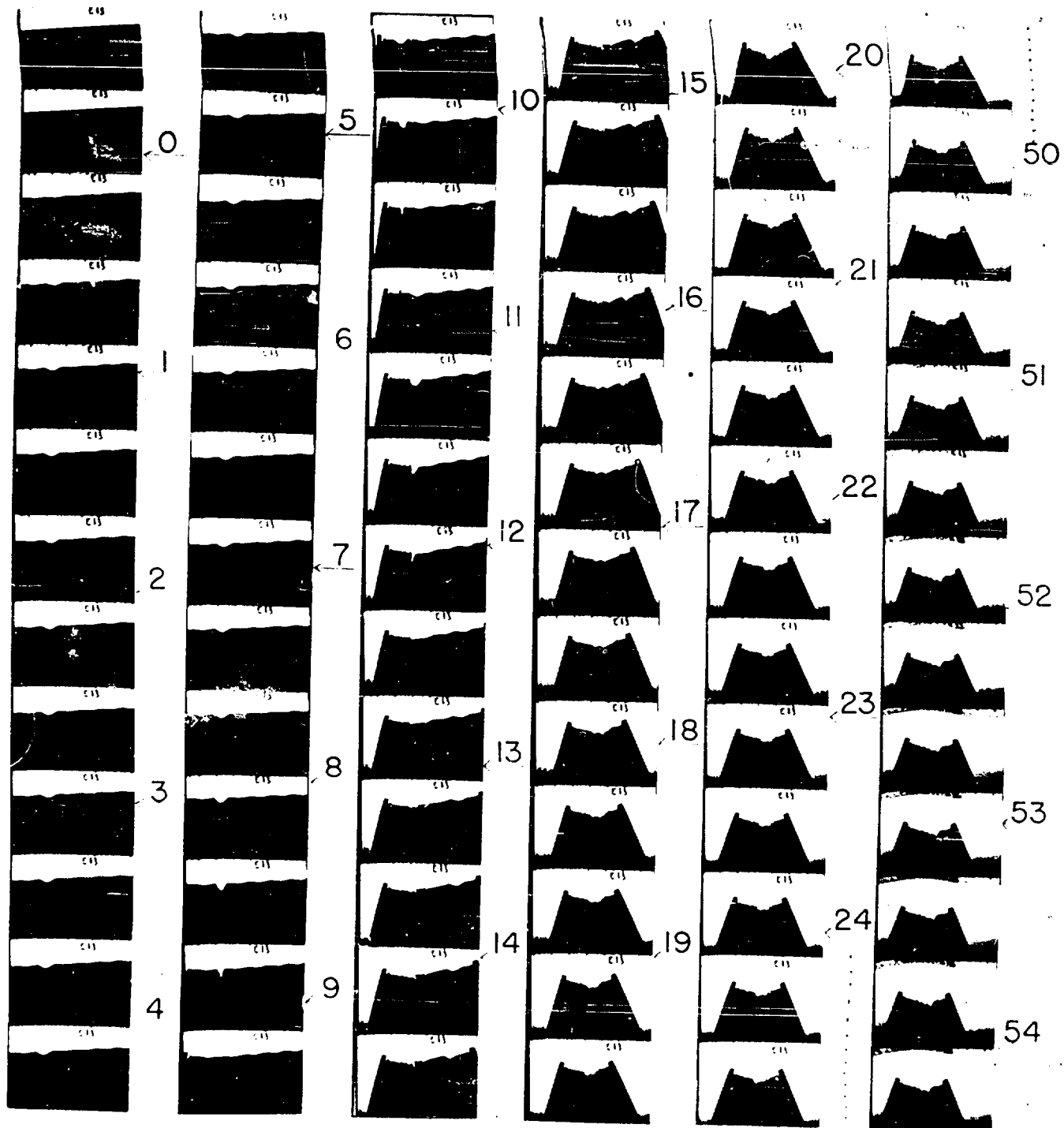


FIG. II7
CYLINDER NO. SD-47-29C
CHARGE: 25.3 G. PRESSED TETRYL
CYLINDER DEPTH: 580'
CHARGE DISTANCE: 28"
OOR: OVERALL = 0.26%, FRONT 90° = 0.12%
BUBBLE PERIOD: 7.9 MSEC
CAMERA SPEED: 2500 FRAMES/SEC

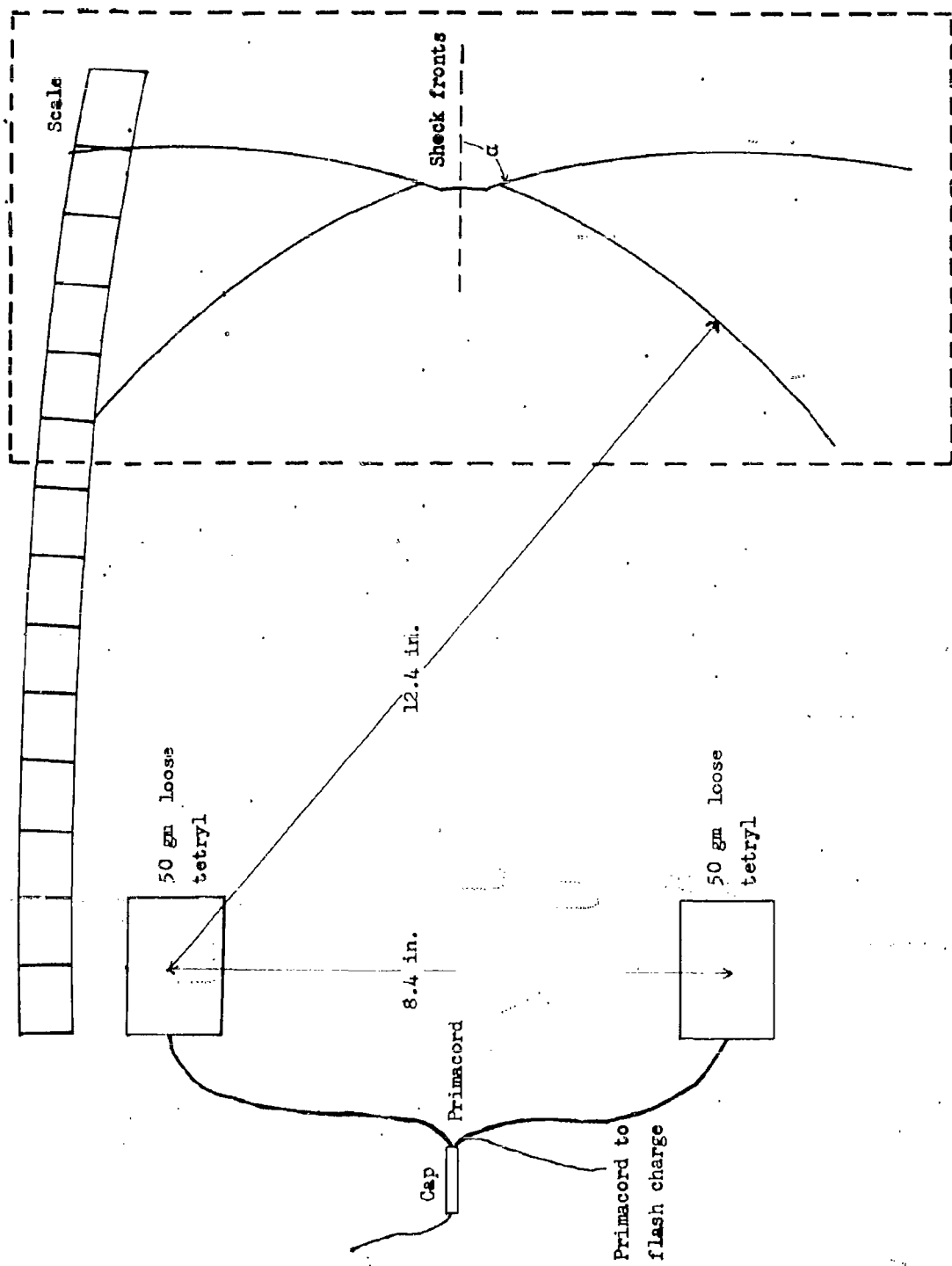


FIG. 118. Schematic view, from camera position, of arrangement for Fig. 121.

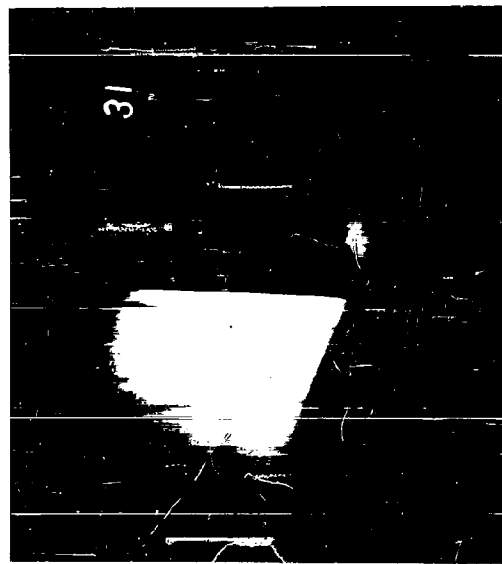


Fig. 119



Fig. 120



Fig. 121

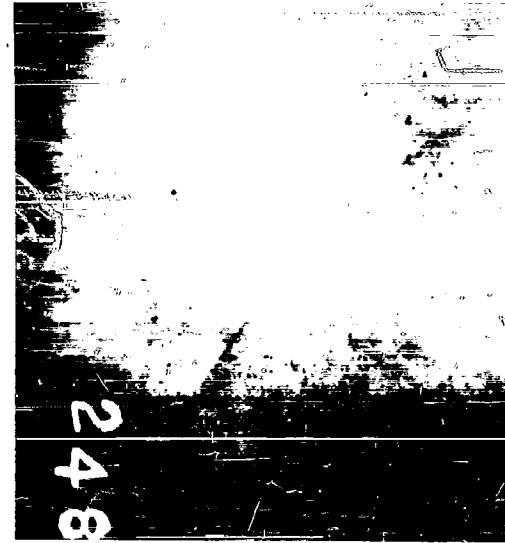


Fig. 122

Intersecting shock waves

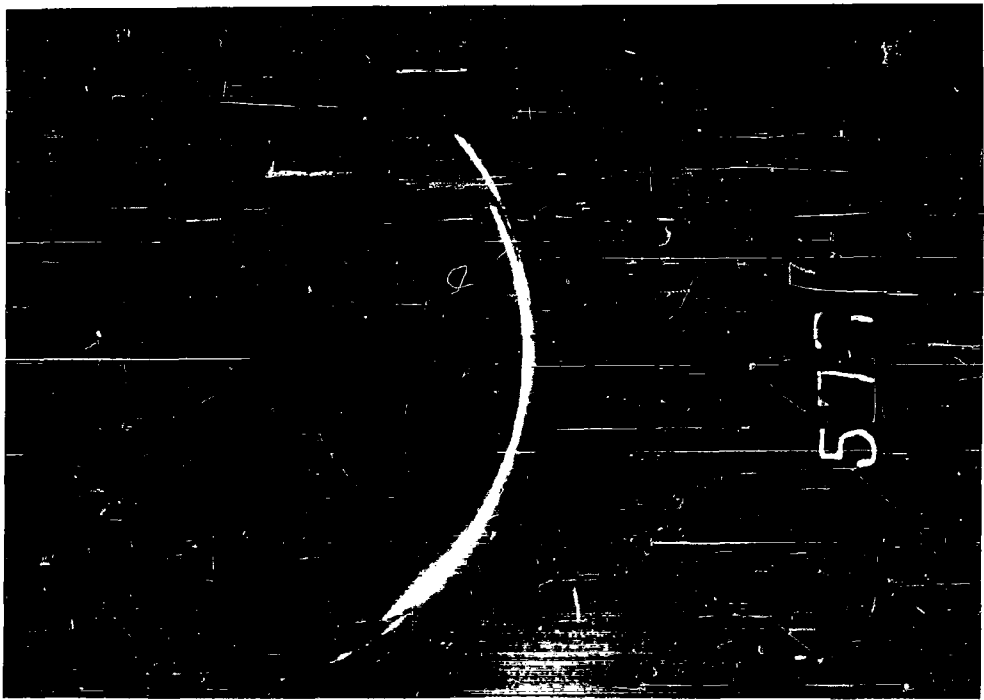


Fig. 123. Shock wave from
300 lb charge 65 ft from camera.

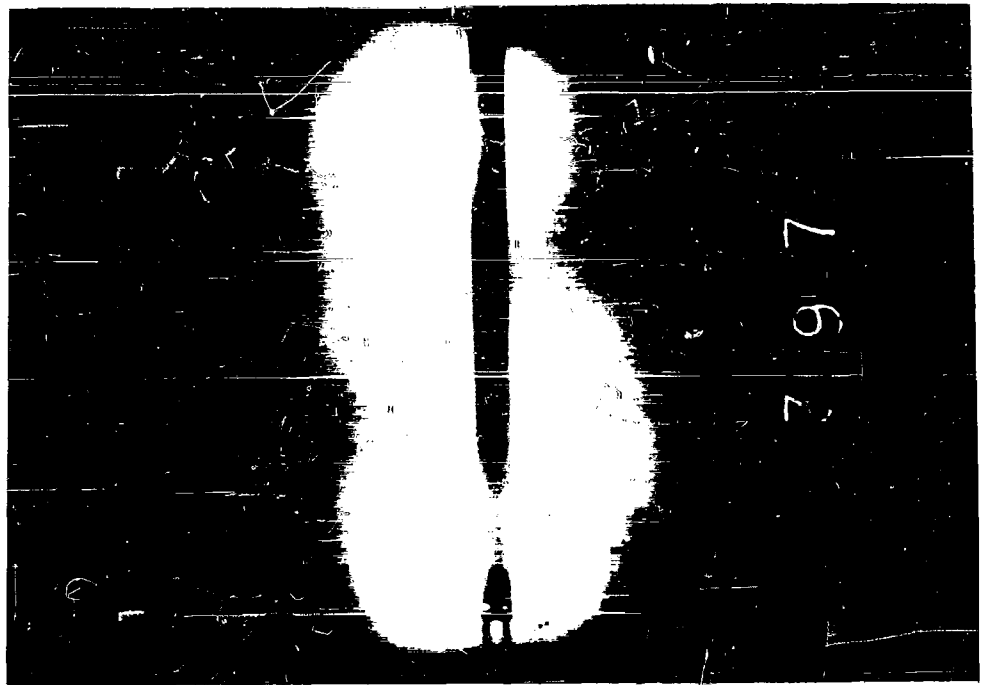


Fig. 124. Shock wave photo-
graphed at two positions by double
exposure technique.

obvious that good pictures can be taken under these circumstances. A large edition of the conventional flash charge was used and the equipment, including flash charge, depth charge and camera was strung out on a line supported by floats. The line was stretched out by a small boat.

(c) Pressure of shock wave determined from shock wave velocity. -- One measurement of average shock wave velocity was made by a double exposure technique. Two flash charges were employed and set off about 246μ sec apart. It was intended to obtain this time difference accurately by means of piezoelectric gages strapped to the two flash charges and recording on an oscilloscope. This part of the experiment failed, and the time difference can be estimated only from the length of primacord used to delay the second flash charge. Figure 124 shows the shock wave at the two positions and a steel scale 15.66 in. long. The shock wave came from a third charge to the left of the field of view. The average velocity determined from this shot is about 5180 ft./sec., or about 270 ft./sec. greater than acoustic velocity for the conditions of the experiment. This corresponds to a pressure of about 8,000 lbs./in.² averaged over the time interval. The average pressure over this period as determined from piezoelectric gage measurements under similar conditions is about 11,000 lbs./in.². Considering the inaccuracy of the time interval measurement, this agreement seems satisfactory. It is to be noted that since the excess velocity (over acoustic) determines the pressure of the shock wave, the accuracy of the measurement of the total velocity must be considerably greater than the accuracy desired for the pressure to be determined.

(d) Experiments showing that the apparent positions of the shock wave coincides closely with its actual position. -- Three experiments have shown that, under the conditions ordinarily employed at UERL, the position of an underwater shock wave is within 1/2 in. of the position indicated by its flash photograph.

In one experiment piezo gages were used to obtain the time interval between the time of the photographic flash and the time the shock wave reached a known radius. From the known velocity of the wave it was possible to calculate its true radius at the time of the photograph and compare it with the value computed from the photographic image.

The 250 gm sphere of cast pentolite which produced the shock wave to be photographed was detonated simultaneously with the initiation of a 46 in. length of primacord leading to the flash charge. The time of the photograph was thus about 185μ sec after the start of the shock wave. A small tourmaline gage fastened to the shock wave charge served to turn on the oscilloscope spot for a rotating drum camera, while a similar gage on the flash charge signalled the time of the photograph. A third gage 17 1/4 in. from the shock wave charge noted the arrival of the shock wave at this radius. The diagram shows the arrangement used.

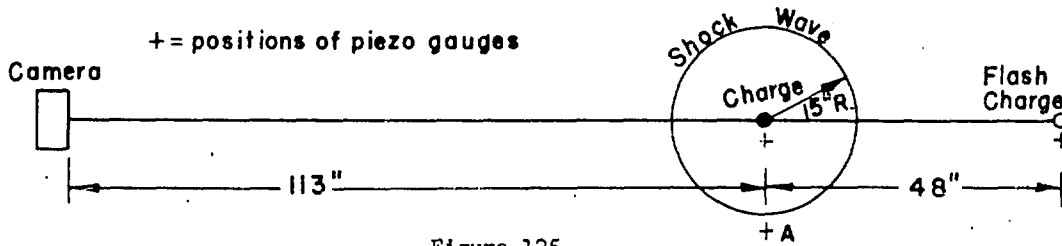


Figure 125.

The radius at the time of the photograph was 14.7 ± 0.2 in. as calculated from the positions of the gages and the measured time intervals. Values for the velocity of sound were taken from "Tables of the Velocity of Sound in Pure Water and Sea Water for use in Echo Sounding and Sound Ranging" (Second Edition) by D. J. Mathers. These were corrected for the effect of finite pressure in the

shock front by means of the data of Kirkwood and Montroll. 9/ Since the distance between the shock wave and the piezo gage at position A was only 2.25 in. at the instant of the photograph, these corrections amount to less than 0.25 in.

A similar experiment was carried out with the shock wave charge just out of the field of view and with a diffusion screen between the flash charge and shock wave. The whole set-up, shown in the diagram below,

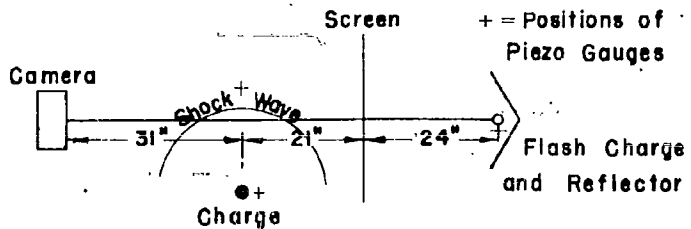


Figure 126

is similar to that used in this laboratory for cavitation studies. The resulting photograph is shown in Figure 129. From it one obtains a distance of 3.44 in. from the shock wave to the piezo gage as compared with a value of 3.36 in. calculated from the piezo records.

A third experiment compared the image of the shock wave with the projection of its shadow on a translucent screen. No piezo gages were involved. Two translucent paper screens were put in the same plane with the shock wave charge and perpendicular to the line from the camera to the charge. The charge and screens as viewed from the camera are sketched below:

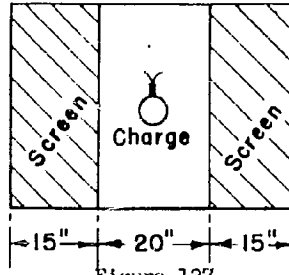


Figure 127

The whole set-up is shown from the top in the following sketch:

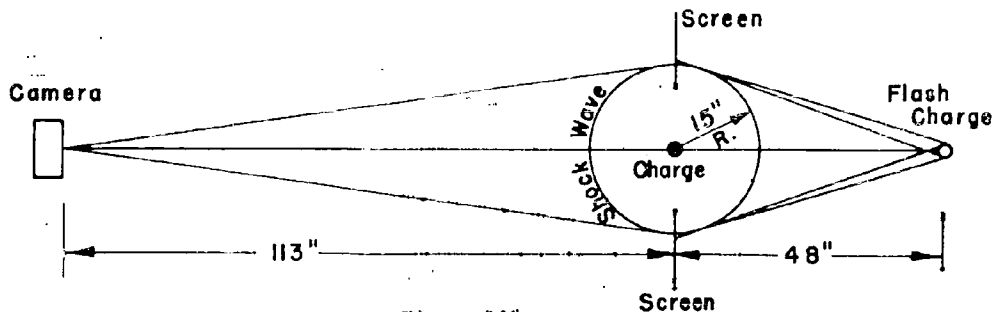


Figure 128

9/ The pressure wave produced by an underwater explosion II, July 1, 1942, by J. G. Kirkwood and E. W. Montroll, OSRD Report 670.

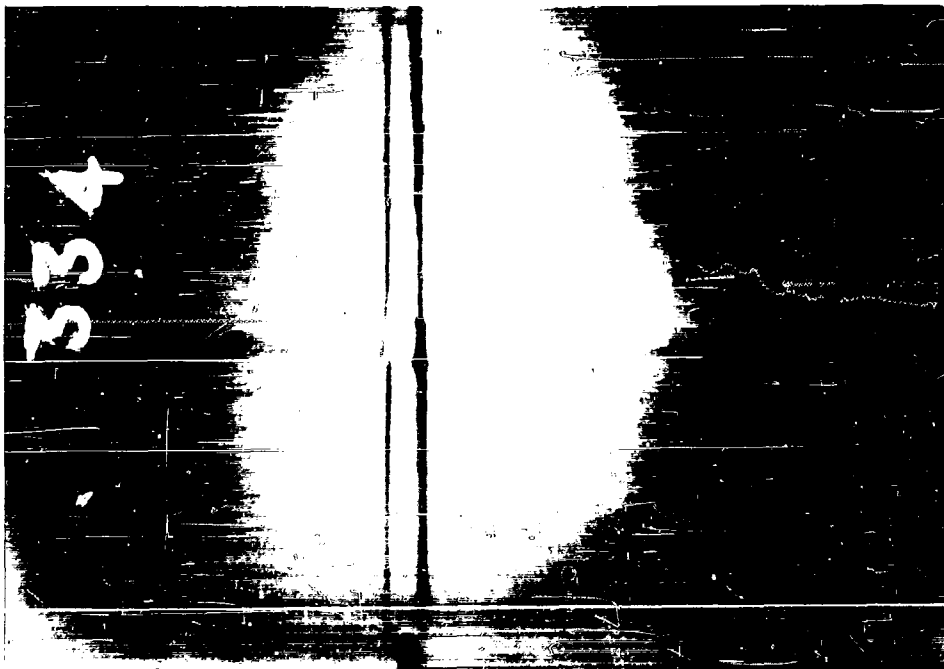


FIG. 129

PHOTOGRAPHS FROM WHICH AGREEMENT BETWEEN
TRUE AND APPARENT SHOCK-WAVE POSITIONS IS OBTAINED.



FIG. 130

The resulting picture is reproduced in Figure 130. The image of the shock wave sphere and the image of the shadow projection of the shock wave sphere are seen nearly to coincide. On the average, however, the radius of the shadow projection appears greater than the radius of the shock wave by an amount corresponding to 0.25 in. The geometry of the experiment would require a radius difference of 0.65 in. The discrepancy is within the limits of experimental error.

(e) Luminosity of charges exploded underwater. -- It is shown elsewhere in this report (Sec. III, 2) that bare charges of cast pentolite were observed to emit light when detonated underwater. Photographs indicate this light to be of very short duration, probably less than 1 μ sec, because of the detail visible (numbers on the charges, cracks, etc.) and because there is no blurring. Foreseeing possible uses for this flash of light (e.g., accurately signalling at a distant point by means of a photo-electric cell the time at which a charge detonates), several tests were conducted to determine if a cased charge would emit light on detonating underwater.

In all tests, the charge, weighing from 1/2 to 1 lb., was placed 5 ft. in front of the camera and the lens aperture was set at f:3.5. A short piece of primacord, to be detonated simultaneously with the charge, was also included in the field of view to serve as a standard for comparison, since primacord had been found to emit light on detonating underwater (See Figure 104). All tests were conducted at night.

The results showed that a heavy opaque casing reduced the emitted light to the extent that it was no longer detectable. For example, a charge wrapped with black rubber tape and detonated barely showed on the film, and a charge enclosed in a piece of steel pipe with pipe caps on the ends resulted in no image at all. Less heavy casings, however, such as 1/16 in. thick brass tubing, tin cans, and black lacquer resulted in weak but definite images of the charge and sometimes streamers of light emanating from the charge. There was some indication that aluminized explosives (torpex and minol) emitted more light than tetryl or pentolite under the same conditions, but the evidence is insufficient on this point.

APPENDIX I

THEORY OF PRESSURE IN FRONT OF AN AIR-BACKED FREE PLATE ACCELERATED BY A SHOCK WAVE

When a plane shock wave strikes a free air-backed plate head on, the pressure in the water in front of the plate first rises as the original wave passes through it, then rises still further as the reflected shock wave returns from the plate. The pressure on the plate causes it to begin to move and its motion reduces the pressure, sending out a rarefaction wave. Consequently, the pressure out in front of the plate, after rising twice, then falls and actually goes negative, provided that cavitation does not interfere. The pressure can be calculated under certain simplifying assumptions; namely, the plate is assumed to be made of an infinitely rigid material, to be of infinite extent (but finite thickness), i.e., a rigid body whose motion is restricted only by its inertia. It is also assumed that cavitation does not form and that acoustic (small amplitude) theory can be used.

The pressure at a point x (measured positively out into the water from the initial position of the plate) and at a time t (measured from the time the original wave strikes the plate) is the sum of three terms:

(1) The pressure due to the original shock wave (assumed to be exponential in shape)

$$- \frac{t + \frac{x}{c}}{\theta} p_0 e \quad , \text{ for } t > - \frac{x}{c} , \quad (I-1)$$

(2) The pressure due to the reflected wave

$$- \frac{t - \frac{x}{c}}{\theta} p_0 e \quad , \text{ for } t > \frac{x}{c} , \quad (I-2)$$

(3) The rarefaction wave from the motion of the plate

$$- \rho c u \quad \text{for } t > \frac{x}{c} . \quad (I-3)$$

In the above, p_0 is the peak pressure and θ the duration parameter of the original wave, m is the mass per unit area and u the instantaneous velocity of the plate, c the velocity of sound in water, and ρ the density of water. By Newton's law the sum of these pressures (acting at $x = 0$) will give the plate a velocity.

$$u = \frac{2 p_0 \theta}{m (\beta - 1)} (e^{-t/\theta} - e^{-\beta t/\theta}) , \quad (I-4)$$

in which $\beta = \rho c \theta / m$. In inserting this value of u in the expression for the pressure at x the proper value of the time to use is $t - x/c$ because of the propagation time. It is convenient to measure pressure in terms of p_0 , time in terms of θ , and distance in terms of $c\theta$; i.e., $P = p/p_0$, $T = t/\theta$, $X = x/c\theta$. Then the sum of the three terms becomes

$$P = e^{-(T+X)} - \frac{\beta + 1}{\beta - 1} e^{-(T-X)} + \frac{2\beta}{\beta - 1} e^{-\beta(T-X)} \quad (I-5)$$

an equation valid only for $T \geq X$. These considerations naturally hold only so long as cavitation does not take place.

Figure 131 shows some of the contour lines for P plotted against time T and distance

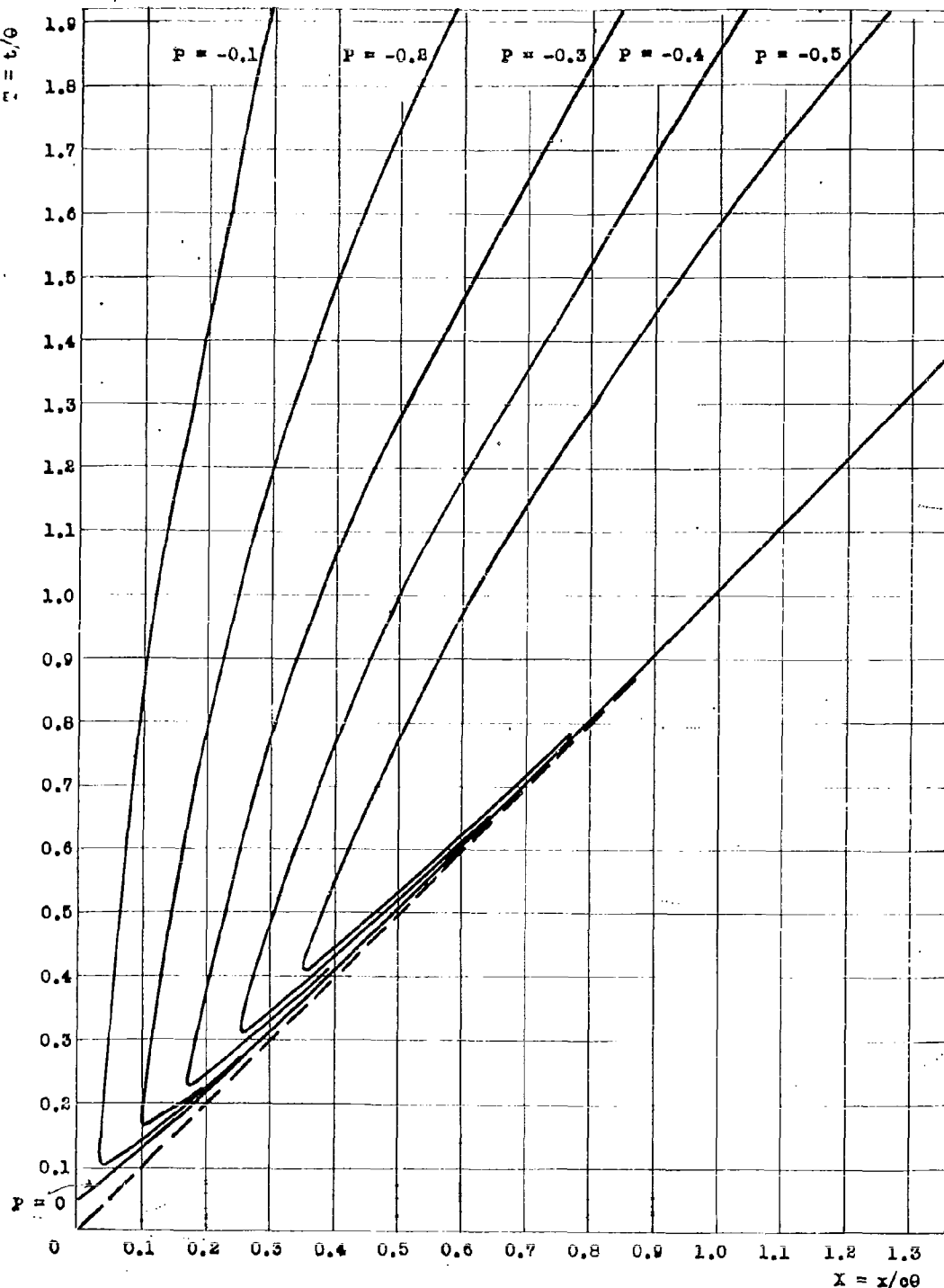


Fig. 131. Pressure before accelerated free plate.
 Contours for $P = p/p_0$ vs. time and distance ($\beta = 83 \text{ m/s}^2$).

15518

X , both in reduced units. $\beta = 83$ in this case, representing a very light plate, or a charge of great duration. The dashed line represents the front of the reflected wave. Below it the pressure is positive due to the original shock wave. Above it the pressure is at first positive and then falls steeply down into a valley of negative pressure. Except for the discontinuous rise and steep fall near the front of the reflected wave ($X = T$) the contours for this case closely approximate the case of a free surface.

Figure 132 shows similar contours for $\beta = 4$, a heavier plate (or smaller duration). In both cases it will be seen that the pressure falls to zero first at the plate, in a finite time $T = [1/(\beta-1)] \ln \beta$. It reaches negative values first out in the water and below a certain limiting negative value the given contour never reaches the plate at all.

Assuming that the theory applies between the shock wave and the cavitation front, and that cavitation occurs at $p = 0$ we get, on solving Equation (I-5) for the time at which the pressure falls to 0 at reduced distance X ,

$$T = t/\theta = \frac{1}{\beta-1} \ln \frac{2\beta e^{\beta X}}{(\beta+1) e^X - (\beta-1) e^X} \quad (I-6)$$

In Table II, the measured values of x_c (farthest distance of cavitation from plate) are substituted in Eq. (I-6) and the calculated values of T are compared with the times computed from the position of the shock wave.

In order to determine the radius of the cavitating region at the plate, it is necessary to take account of diffraction.

A very rough treatment of the effect of the diffraction wave is as follows. The same basic Eq. (I-1) can be used to compute the time T at which the pressure in front of the plate has fallen from $2p_0$ to a value equal to that outside the plate, $p(T)$. For this purpose $X = 0$ (surface of plate) and $p/p_0 = e^{-T}$ so

$$T = \frac{\theta}{\beta-1} \ln \frac{2\beta}{\beta+1} \quad (I-7)$$

Beginning at time T a pressure wave will spread inward from the edges because the pressure in front of the plate is being lowered by its motion. This pressure wave will reach a radius R at time $[T + (R-r)/c]$. If the pressure at R has fallen to zero before this time, it is postulated that cavitation will extend out to R , but if the diffraction wave reached R first then cavitation will not extend to R . Consequently, this theory predicts that the maximum radius of cavitation R_c will be determined by the equation

$$T + \frac{(R - R_c)}{c} = \theta_c \quad (I-8)$$

where θ_c is the so-called cavitation time, i.e., time for p to fall to zero at the front of the plate. If $X = 0$ in Eq. (I-6) $t = \theta_c$ so

$$\theta_c = \frac{\theta}{\beta-1} \ln \beta \quad (I-9)$$

Combining Eqs. (I-7), (I-8), and (I-9),

$$R_c = R - \frac{c\theta}{\beta-1} \ln \frac{\beta+1}{2} \quad (I-10)$$

or

$$\frac{R - R_c}{c\theta} = \frac{1}{\beta-1} \ln \frac{\beta+1}{2} \quad (I-10)$$

The latter equation expresses the result in a dimensionless form, in which the distance in from the edge of the disk, $R - R_c$, is measured in terms of the length unit $c\theta$. In the case of a plate surrounded by an infinite rigid baffle, $T = 0$ and Eq. (I-10) becomes:

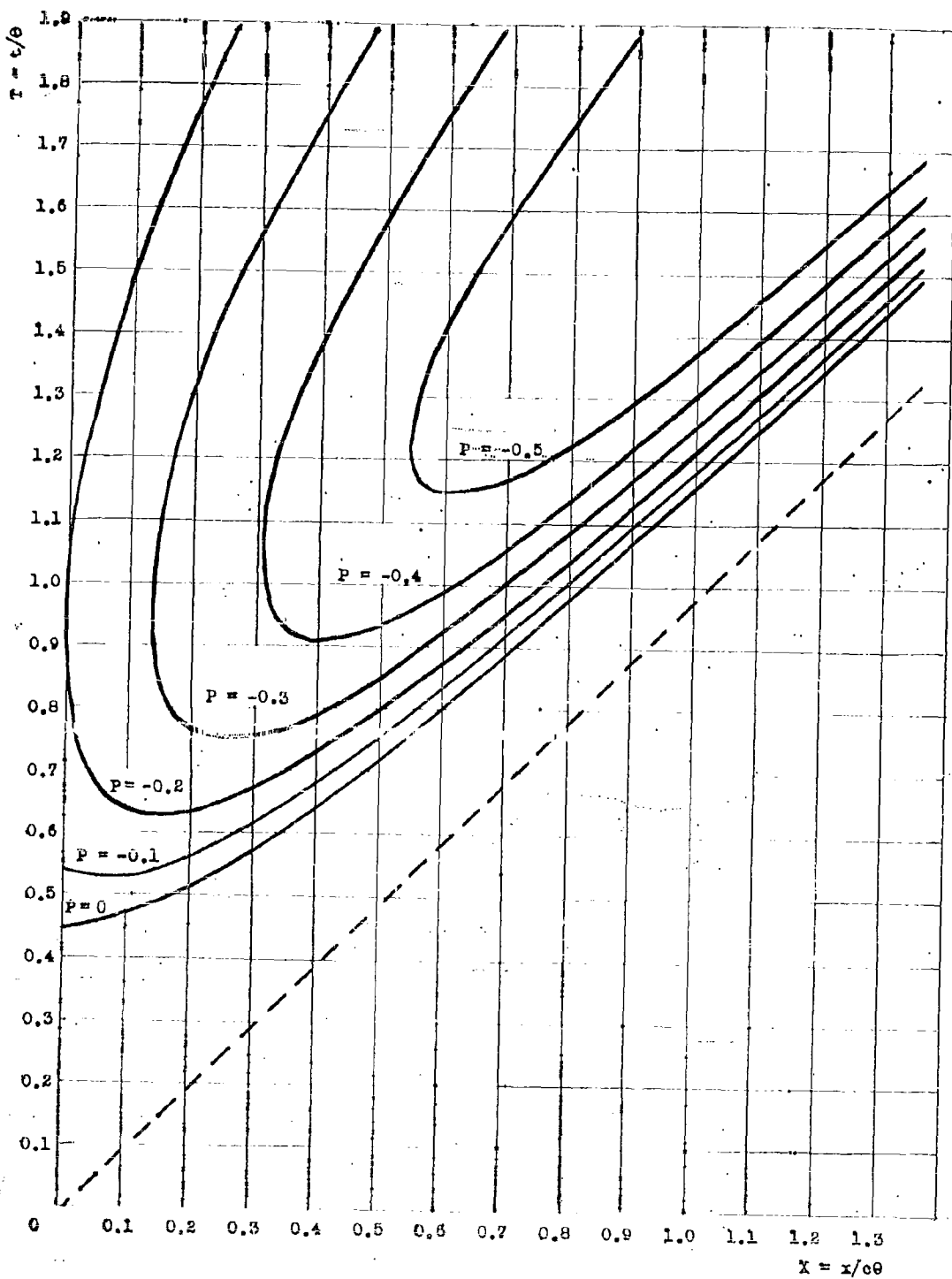


Fig. 132. Pressure before accelerated free plate.
 Contours for $P' = p/p_0$ vs. time and distance ($\beta = 4 = 1000/m$).

$$\frac{R - R_c}{\alpha \theta} = \frac{1}{\beta - 1} \ln \beta \quad (I-11)$$

This is the equation previously used as a cavitation criterion in connection with the photographs of the UERL diaphragm gage which is a baffled gage.

APPENDIX II

THEORY OF PEAK PRESSURE AND TIME CONSTANT DETERMINATION FOR SHOCK WAVES
BY THE METHOD OF OPTICAL DISTORTION

A theory has been developed for several sets of experimental conditions designed to measure the peak pressure of shock waves by the method of optical distortion. For one of these experimental arrangements (1 below), a method has also been developed for calculating the time constant. Since this arrangement has had considerable success experimentally, it will be discussed in detail.

1. Grid in plane of center of charge; charge off to the side; spherical shock wave

To study the distortion of light rays passing through the high pressure region behind the shock, an experimental arrangement as diagrammed in Figure 133 was used and the theory developed is based on these experimental conditions. E is the charge producing the shock wave S to be studied, C is the camera lens, F is a flash charge and G is a lucite sheet marked off in a uniform grid of $1/4$ in. spacing. The grid is so placed that the grid lines intersect the shock wave S diagonally in the portion of the shock studied. Two typical intersecting lines are shown in the front view in Figure 133. The charge was placed in the plane of the grid, and the line perpendicular to the grid passing through the center of the camera lens intersected the grid a short distance behind the shock, approximately 5% of the radius.

In the system of Cartesian coordinates shown in Figure 133 the position of the center of the camera lens is defined at (x_0, y_0, z_0) . On the assumption that the grid acts as a source of diffuse illumination, a ray whose reverse path is the vector \bar{M} from the camera to the shock front is considered. The intersection of this ray with the shock front is defined as (x, y, z) . If there were no distortion, the ray would continue along the line \bar{M} and strike the grid at $(x'', 0, z'')$, but actually the ray follows some curved path \bar{P} determined by the decay characteristics of the shock and strikes the grid at the point $(x', 0, z')$. Knowing the actual distance from the charge to a uniquely defined point on the grid, one obtains the radius of the shock wave from the photographic print by reference to this point after the scale factor of the print is determined from the undistorted part of the grid. The coordinates of the camera are also obtained by reference to this point. On the photographic print, the points $(x'', 0, z'')$, and $(x', 0, z')$ may be located, the latter being obtained by extending lines from the undistorted part of the grid until they intersect behind the shock.

(a) Peak pressure determination. -- As a first approximation, an average pressure may be calculated by assuming a step shock wave, that is, a constant pressure behind the front. With this approximation the curve \bar{P} is replaced by the vector \bar{N} (Figure 133) from (x, y, z) to $(x', 0, z')$, and the step pressure calculated is, to this approximation, the pressure in the decaying wave on the spherical surface centered at E and passing through a point on \bar{P} at which the tangent of \bar{P} is parallel to \bar{N} . We define this index of refraction or pressure for a given intersection of grid lines as n_{av} or p_{av} , respectively.

A very simple derivation of the index of refraction corresponding to this average pressure as a function of the distortion vector \bar{D} , (the vector from $(x'', 0, z'')$ to $(x', 0, z')$ for the given ray \bar{M}), and the geometry of the experiment can be given in the system of coordinates discussed above. We are given (x_0, y_0, z_0) , $(x'', 0, z'')$, $(x', 0, z')$ and R , the radius of the shock wave. The point (x, y, z) is readily obtained as the intersection of the line joining (x_0, y_0, z_0) and $(x'', 0, z'')$ with the sphere of radius $|R|$.

The following vectors are defined.

$$\bar{p} = xi + yj + zk,$$

$$\bar{M} = (x-x_0)i + (y-y_0)j + (z-z_0)k,$$

$$\bar{M} = (x''-x)i + (0-y)j + (z''-z)k,$$

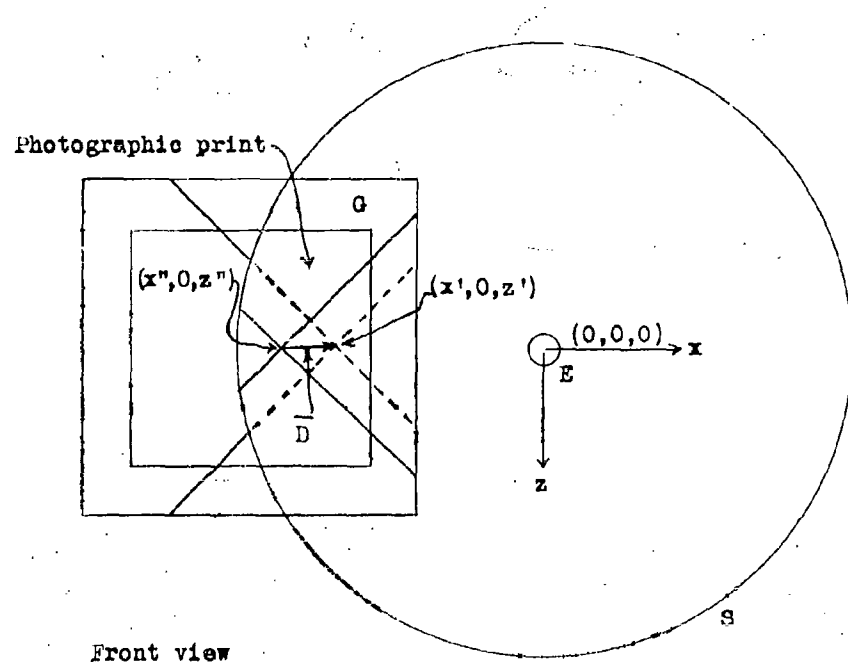
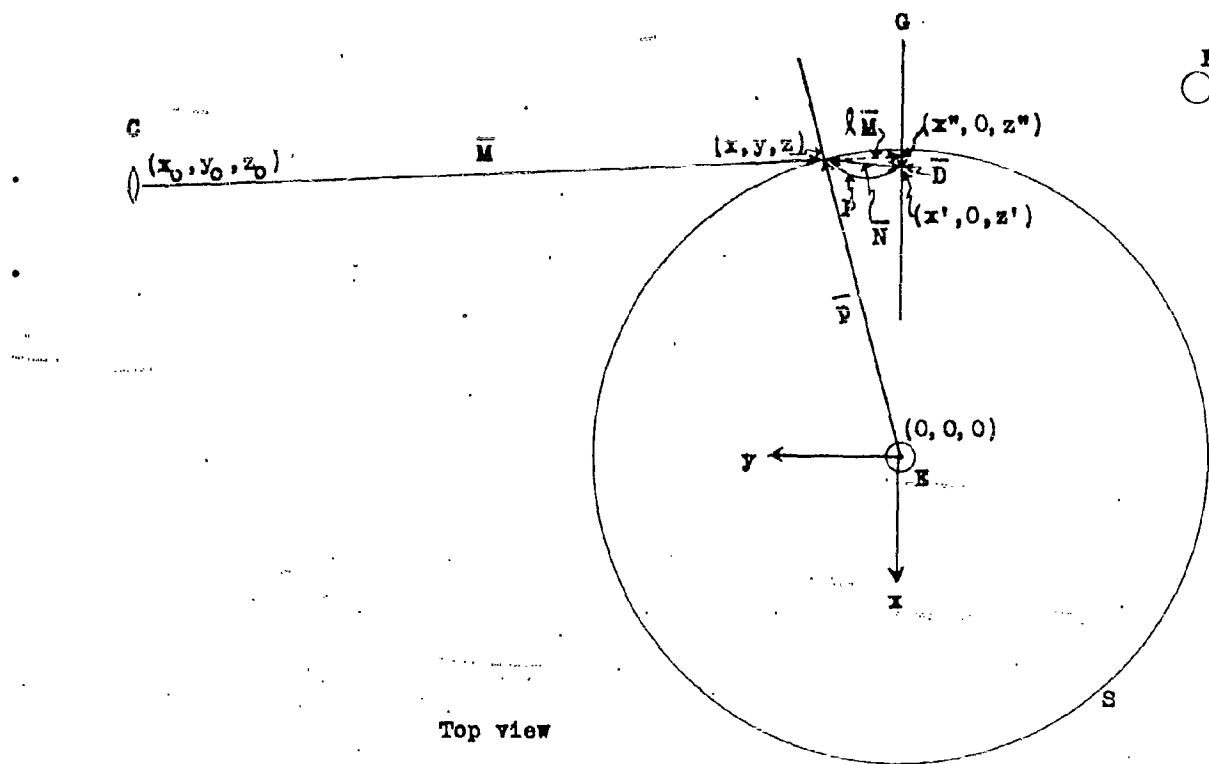


Fig. 133. Experimental arrangement for optical distortion study.

$$\bar{N} = (x' - x)i + (0 - y)j + (z' - z)k, \quad (II-1)$$

$$\bar{D} = \bar{N} - \bar{M} = (x' - x'')i + (z' - z'')k$$

$$= D_x i + D_z k.$$

The magnitude of all vectors and distances is to be taken in units of $|R|$, i.e., $|p| = 1$.

Consider the following cross-product relations.

$$\left. \begin{aligned} \frac{M \times P}{|M|} &= \bar{q} \sin \theta, \\ \frac{N \times P}{|N|} &= \bar{q} \sin \theta', \end{aligned} \right\} \quad (II-2)$$

where \bar{q} is a unit vector perpendicular to the plane which contains \bar{M} , \bar{P} , \bar{N} and \bar{D} and θ and θ' are the angles of incidence and refraction respectively in this plane. This is not necessarily the plane shown in the top view in Figure 133. Applying Snell's Law,

$$\frac{\sin \theta}{\sin \theta'} = \frac{n_{av}}{n_0} = \nu,$$

where n_{av} is the index of refraction corresponding to the average pressure p_{av} , and n_0 is the index of refraction of sea water at zero pressure, we obtain the relation,

$$\frac{M \times P}{|M|\nu} = \frac{N \times P}{|N|}, \quad (II-3)$$

From the last of (Eqs. II-1),

$$\frac{D \times P}{|D|} = \frac{N \times P}{|N|} - \frac{(M \times P)}{|M|}, \quad (II-4)$$

or using (Eq. II-3),

$$D \times P = \frac{|N|}{|M|} \left(\frac{1}{\nu} - \frac{\ell |M|}{|N|} \right) M \times P, \quad (II-5)$$

which may be written,

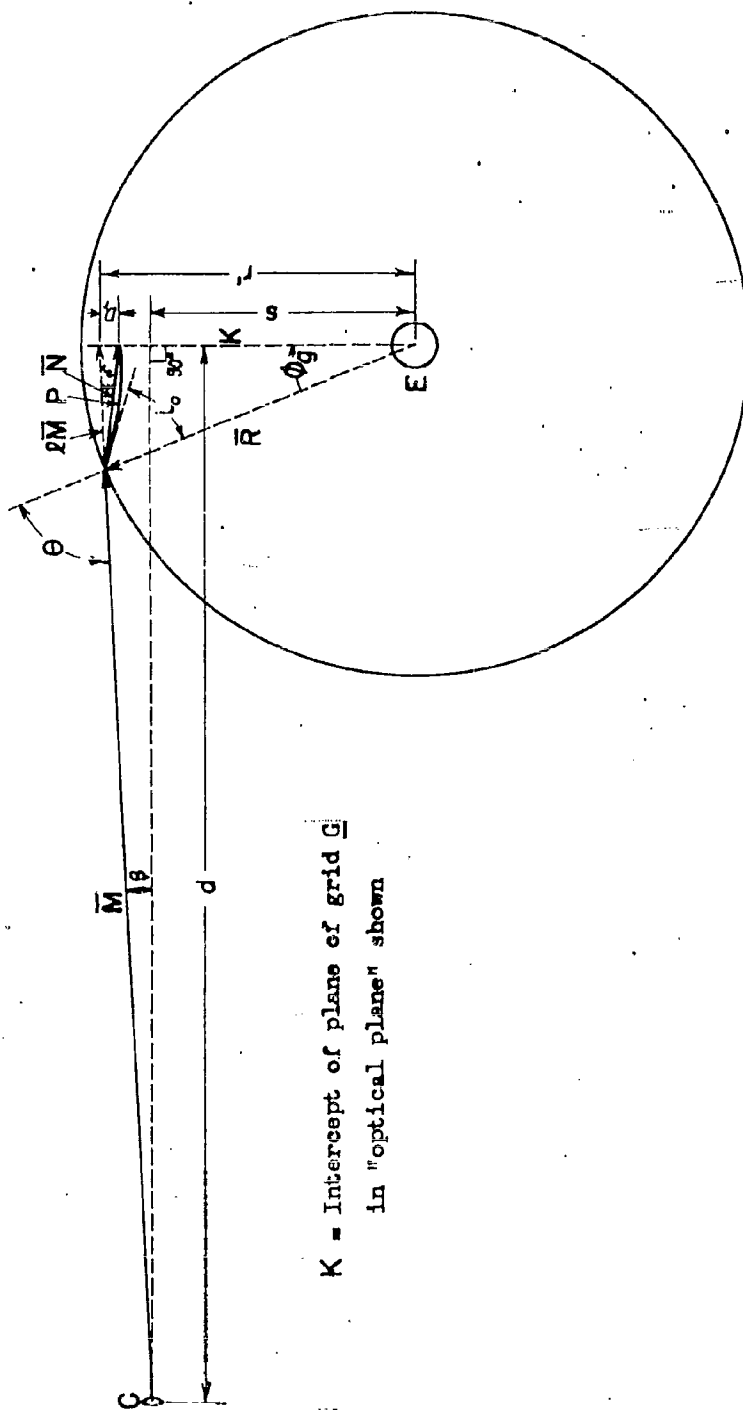
$$\left. \begin{aligned} \frac{|N|}{|M|} \left(\frac{1}{\nu} - \frac{\ell |M|}{|N|} \right) (z_0 y - y_0 z) &= -D_z y, \\ \frac{|N|}{|M|} \left(\frac{1}{\nu} - \frac{\ell |M|}{|N|} \right) (y_0 x - x_0 y) &= D_x y, \end{aligned} \right\} \quad (II-5')$$

or,

$$\left. \begin{aligned} \frac{1}{\nu} &= -\frac{|M|}{|N|} \frac{D_z y}{(z_0 y - y_0 z)} + \frac{\ell |M|}{|N|} \\ \frac{1}{\nu} &= \frac{|M|}{|N|} \frac{D_x y}{(y_0 x - x_0 y)} + \frac{\ell |M|}{|N|} \end{aligned} \right\} \quad (II-5'')$$

The distances $|M|$, $|N|$ and $\ell |M|$ can be readily obtained from the coordinates (x, y, z) , (x_0, y_0, z_0) , $(x', 0, z')$, and $(x'', 0, z'')$. Although two values of the index of refraction can be obtained from each distortion, they are not independent, and in general because of the coordinates chosen and the experimental arrangement used D_z was too small to be measured.

Given ν from the above and n_0 for sea water, P_{av} can be obtained by applying the relationship between the index of refraction and pressure for water. This relationship is discussed later.



K = Intercept of plane of grid G in "optical plane" shown

Fig. 134. Plan view of "optical plane".

Since the computational method outlined above is somewhat lengthy, a more direct method, again assuming a step shock but taking advantage of the planar nature of the problem, was used in the actual calculations. The determination of the "optical plane", that containing \bar{M} , \bar{p} , \bar{N} , \bar{D} , E and C , is very simple when the charge is in the plane of the grid, for, in this case, the intercept of the optical plane in the plane of the grid contains \bar{D} and E . Knowing the projection of the camera on the line containing \bar{D} and E , and the perpendicular distance d of the camera from it, the optical plane is determined and can be represented as in Figure 134. The distance $|R|$ to which all other dimensions are referred is obtained as described above. r' and D_r are obtained directly from the print as above, whereas d and s are obtained from the known position of the camera relative to the grid. To derive the index of refraction from the distortion of the ray \bar{M} in terms of these measurements using the symbols shown in Figure 134 the following relations are used.

$$\tan \beta = \frac{r' - s}{d}, \quad (II-6)$$

where β may be positive or negative, and since $|R| = 1$,

$$\cos(\beta_g - \beta) = r' \cos \beta. \quad (II-7)$$

Then using the law of cosines,

$$|\bar{M}| = \sqrt{1+r'^2-2r' \cos \beta_g}. \quad (II-8)$$

It can be shown, using the law of sines, that

$$\tan \delta = \frac{D_r \cos \beta}{1 - \frac{D_r}{|\bar{M}|} \sin \beta}. \quad (II-9)$$

On applying Snell's Law,

$$\nu = \frac{\sin \theta}{\sin \theta'} = \frac{\sin \theta}{\sin(\theta - \delta)}, \quad (II-10)$$

$$\nu - 1 = \frac{n_{av} - n_0}{n_0} = \frac{\sin \theta}{\sin \theta - \cos \theta \tan \delta} \left[\frac{1}{\cos \delta} - 1 \right] + \cos \theta \tan \delta \quad (II-11)$$

where $\theta = 90^\circ - (\beta_g - \beta)$

In order to convert n_{av} to p_{av} , data on the pressure coefficients of index of refraction for water are required.

Data were available for fresh water, and were assumed to hold for salt water as well. This assumption is felt to be valid to within a few percent as is indicated by some preliminary calculations. In Table VII the available data on the coefficients a and b in the equation,

$$n(p) - n_0 = ap - bp^2, \quad (II-12)$$

are given together with the source of the data. For the calculations of p_{av} concerning a specific point, Eq. (II-12), of course, becomes

$$n_{av} - n_0 = a p_{av} - b p_{av}^2.$$

The type of film used in the experiments studied was Contrast Process Ortho, which is sensitive in a narrow range of wave length centered around ca. 4800 A.U. In order, then, to correct n_{av} to p_{av} it is necessary to obtain adiabatic values of a and b for a wave length of 4800 A.U. and for the proper temperature. The isothermal value of a was taken from the data Rontgen and Zehnder for a wave length of 5890 A.U. and the proper temperature for the given experiment. It was then

corrected for wave length from the data for various wave lengths of Röntgen and Zehnder, assuming the difference due to wave length is independent of temperature. It was then corrected to the adiabatic coefficient from the data of Raman and Venkataraman, assuming again that the difference between the isothermal and adiabatic α is independent of temperature. The value of b was taken directly from the isothermal data of Peindexter and Rosen by interpolating for the proper wave length. It was assumed independent of temperature. The error in b can be of the order of 30% and still make an error of only ca. 3% in the calculation of the pressure in the range of pressure studied (ca. 17,000 lb/in.²).

Table VII Coefficients a and b in
 $n(p) - n_0 = ap - bp^2$ for Pure Water

t (°C)	Wave Length (A.U.)	$a \times 10^6$ (per atm.)	$b \times 10^6$ (per atm. ²)	Type of Pressure Change	Source of Data*
-0.78	5890	16.91	-	Isothermal	R and Z
0.06	"	16.87	-	"	"
0.42	"	16.78	-	"	"
1.05	"	16.68	-	"	"
2.62	"	16.51	-	"	"
2.67	"	16.52	-	"	"
2.92	"	16.48	-	"	"
3.10	"	16.44	-	"	"
4.95	"	16.26	-	"	"
8.95	"	15.87	-	"	"
9.00	"	15.91	-	"	"
13.05	"	15.56	-	"	"
13.28	"	15.56	-	"	"
17.83	"	15.26	-	"	"
18.01	"	15.26	-	"	"
18.03	"	15.25	-	"	"
23.27	"	14.97	-	"	"
23.1	"	14.98	-	"	R and V
18.0	4861	15.40	-	"	R and Z
18.0	6807	15.16	-	"	"
25.0	4060	15.02	.003182	"	P and R
25.0	4360	14.65	.002700 **	"	"
25.0	5460	14.75	.003132	"	"
25.0	5790	14.56	.002990	"	"
23.1	5890	14.66	-	Adiabatic	R and V

* R and Z - W. C. Röntgen, and L. Zehnder, Ann.d. Physik (Wied.) 44, 24-51 (1891) (low pressure study).

R and V - Sir Venkata Raman, F.R.S., and K.S. Venkataraman, Proc. Roy. Soc. (London), 171A, 137 (1939) (low pressure study).

P and R - F. E. Peindexter and J. S. Rosen, Phys. Rev. (2), 45, 760(A) (1934) (pressures up to 1800 kg/cm²).

** This datum seems out of line with the rest.

The peak-pressure of the shock wave was then calculated from several values of p_{av} in the following manner. The assumption was made that p_{av} calculated from a given intersection of grid lines with a given value of r' was the pressure existing in the decaying spherical shock on a spherical surface of radius

$$r_{av} = \frac{|R| + (r' - D_p)}{2}$$

the average radius vector for the vector \bar{M} was then plotted against $|R| - r_{av}$ (see Figures 108, 109, 110 and 111) on semi-log paper. Within experimental scatter the points fall on a straight line which was extrapolated to $|R| - r_{av} = 0$, that is, to the shock front. The pressure at this point was taken to be the peak pressure of the shock wave. The error in the assumption as to what value of r_{av} the value of P_{av} applies should go to zero in the limit, $|R| - r_{av} = 0$.

(i) Technique of Measurement. Before the shot, the perpendicular distance from the camera lens to the grid was measured. A cross was marked on the lucite grid at the foot of this perpendicular, and the distance s (Figure 134) was measured from the center of the charge to the cross. An additional cross ^{10/} was marked on the lucite grid on the extension of the line joining the charge and the first cross about 4 in. (measured accurately) beyond the first cross. This second cross was placed so as to be ahead of the shock wave, and thus to appear undistorted in the final picture. It was from this measurement from the charge to the second cross that the radius of the shock wave was determined on the final photograph. The illumination was provided by a flash charge for which the firing was delayed by means of primacord from the firing of the charge which produced the shock wave to be studied.

The measurements were taken from prints of the original photograph. With a scale factor for the print determined from the undistorted part of the grid, the charge position was determined from the experimental measurements referred to the crosses marked on the grid. By use of this as a center, the shock front was drawn in on the print as a circle whose radius was such that it passed through the breaks in the lines of the undistorted and distorted parts of the grid. Several of the undistorted lines were extended behind the shock front giving intersections which are called "actual" intersections to which correspond the "apparent" intersections seen behind the shock. There was no difficulty in assigning any given actual intersection to an apparent intersection. Through each pair of intersections a radial line was drawn from the charge position, and was extended to intersect the shock front. This is the intercept of the optical plane in the plane of the grid. The distances r' and R' (Figure 134) can be measured directly on this line. R' , the radius of the shock front, was obtained on the print by reference to the crosses marked on the lucite grid. The distance d is obtained by measuring the perpendicular distance from the cross to the intercept line and using this measurement together with the experimental measurement of the distance from the camera lens to the lucite grid.

(b) Calculation Procedure for Time Constant (Exponential Decay Constant with Distance Behind Front). The path of a ray of light in a non-homogeneous medium has been treated very thoroughly by Richard Gans (see e.g. Handbuch der Experimental Physik, Volume 19, p. 341 ff. and Ann d Physik (4), 47, 709 (1915)). From his derivation based on Snell's law (see reference to Handbuch der Experimental Physik) for a medium in which the index of refraction is a function only of r , the radius in plane polar coordinates, the following differential equation is obtained for the path of a ray of light:

$$\frac{dp}{dr} = \frac{n_R |R| \sin i_0 dr}{r \sqrt{n^2 r^2 - n_R^2 |R|^2 \sin^2 i_0}} , \quad (11-13)$$

where ϕ is the polar angle, $|R|$ is the radius of the shock front, r is the length of the radius vector to any point on the path, i_0 is the angle made by the ray of light and the radius vector to the point, $r = |R|$, $\phi = 0$ (see Fig. 134). ϕ is measured clockwise from the point of entry into the shock wave of the reverse vector \bar{M} (Fig. 134) for the ray of light studied. In Fig. 134 ϕ_g , the polar angle at the grid, is shown. n_R is the index of refraction at $r = |R|$, and n is the index of refraction at r .

^{10/} The second cross is not necessary if the position of the first cross is corrected for optical distortion.

The method used in determining the time constant of the shock wave was to express n as a function of r in terms of the parameters of an assumed exponential shock wave (exponential with distance behind the front), the peak pressure and time constant. This may be done by writing p in Eq. (II-12) as a function of r ,

$$p = p_{\max} e^{-\frac{(|R| - r)}{\theta_r}}, \quad (II-14)$$

where θ_r is expressed in units of length.

Substituting p from Eq. (II-14) into Eq. (II-12) gives

$$n(p) = n_0 + ap_{\max} e^{-\frac{(|R| - r)}{\theta_r}} - bp_{\max}^2 e^{-\frac{2(|R| - r)}{\theta_r}}, \quad (II-15)$$

where n_0 (the index of refraction at zero pressure), a , and b are functions of the temperature for a given type of film, and p_{\max} is the peak pressure for the given shot as determined by the method outlined in this Appendix I (a).

This function of r is then substituted for n in Eq. (II-13). In Eq. (II-13) n_R is obtained from Eq. (II-15) by putting $r = |R|$.

Eq. (II-13) is a function of the given ray of light on a given film, that is, of the pair of intersections (apparent and actual) of the pair of grid lines studied, because of the explicit presence of the angle i_0 . This is obtained for each pair of intersections by the following equation:

$$\frac{\sin i_0}{\sin \theta} = \frac{n_0}{n_R}, \quad (II-16)$$

where the angle θ (Fig. 134) is obtained for the given point (that is, for the given pair of intersections) in the calculation procedure for p_{av} for that point.

Thus all the parameters of Eq. (II-13) are determined except θ_r . Some general discussion of this equation is felt to be necessary. A statement of Snell's Law for spherical symmetry, in which case the path of a given ray of light, as was discussed previously, lies in a great circle, is given by the following:

$$n_R |R| \sin i_0 = n r \sin i = C, \quad (II-17)$$

where i is the angle made by the path of light and the radius vector r to a given point on the path, and n is the index of refraction at r for some given θ_r in Eq. (II-15). Then in Eq. (II-13) the denominator vanishes at the point of total reflection, that is, at the point where $\sin i = 1$.

The right hand side of Eq. (II-13), from physical arguments, has a finite integral from $r = |R|$ to $r = r_{\min} - \epsilon$ where,

$$r_{\min} n(r_{\min}, \theta_r) = n_R |R| \sin i_0. \quad (II-18)$$

By making ϵ sufficiently small, the integration can be carried up to within an infinitesimal distance from r_{\min} . Then since the path of light is symmetrical about the radius vector of length r_{\min} , the whole path is known from the point of entry into the shock wave to the point of exit from the shock wave.

The first step in the calculation of θ_r is to determine $\theta_{r,\min}$ where

$$(r' - D_r) n(r' - D_r, \theta_{r,\min}) = n_R |R| \sin i_0. \quad (II-19)$$

Physically $\theta_{r,\min}$ is the lowest value of the exponential decay constant which will allow the given ray of light studied to get as far into the shock wave as the point at which it is observed to strike the lucite grid, that is, at $r = r' - D_r$ (Fig. 134).

The procedure, then, for determining θ_t for a given point on a given film is to choose several values of θ_r , $\theta_{r,\min}$ and to calculate $\phi(r' - D_r, \theta_r)$ by numerical integration.

$$\phi(r' - D_r, \theta_r) = \int_{|R|}^{r' - D_r} \frac{n_R |R| \sin i_o dr}{r \sqrt{n^2 r^2 - n_R^2 |R|^2 \sin^2 i_o}} , \quad (II-13a)$$

where n is given as a function of θ_r and r in Eq. (II-15). ϕ is then plotted against θ_r and r in Eq. (II-15). ϕ is then plotted against θ_r at the value of $r' - D_r$ determined by the point studied. ϕ can easily be shown by physical arguments or by mathematical considerations to be a monotonically decreasing function of θ_r . The value of θ giving a value of $\phi = \phi_g$ (Fig. 134), that is, that value of ϕ obtained in the course of the calculation of p_{av} for the given point, is taken as the correct value of θ_r for the shock wave as determined by that point. If no value of θ_r , $\theta_{r,\min}$ gives a value of ϕ as large as ϕ_g , the ray of light studied is assumed to have passed through the point of total reflection after it left the diffuse light source, the lucite grid. In this case (Eq. II-13a) must be replaced by

$$\phi(r' - D_r, \theta_r) = \int_{|R|}^{r_{\min} +} \frac{n_R |R| \sin i_o dr}{r \sqrt{n^2 r^2 - n_R^2 |R|^2 \sin^2 i_o}} + \int_{r_{\min} +}^{r' - D_r} \frac{n_R |R| \sin i_o dr}{\sqrt{n^2 r^2 - n_R^2 |R|^2 \sin^2 i_o}} \quad (II-13b)$$

Again the integration is carried out numerically. In the numerical integration near $r_{\min} +$, the intervals chosen must, of course, be very small. Again a plot of ϕ vs. θ_r is made, and θ_r is then determined for the given point as that value which gives a $\phi = \phi_g$ for that point.

Values of θ_r are calculated for several points on a given film. The tacit assumption has been made that θ_r can be a function of the value of $r' - D_r$ for the point for which it is calculated. The conversion of this exponential decay constant with distance behind the shock front to an exponential decay constant with time behind the front is discussed below.

(c) Calculation Procedure for Time Constant (Exponential Decay Constant with Time Behind Front). In the conversion of θ_r to θ_t , the exponential parameter in

$$p_{p.E.}(t) = p_{\max} e^{-\frac{t}{\theta_t}} , \quad (II-20)$$

θ_t is assumed constant, but the possibility is admitted of dependence of θ_r on the value of $r' - D_r$ for the point for which θ_r is calculated. $p_{p.E.}(t)$ is the pressure that would have been recorded by a piezoelectric gage at time t after the passing of the shock front of peak pressure p_{\max} . $p_{O.D.}(r)$ is the pressure at $t = 0$ and at a distance ($|R| - r$) behind the shock front of pressure p_{\max} and radius $|R|$. That is,

$$p_{O.D.}(r) = p_{\max} e^{-\frac{(|R| - r)}{\theta_r}} \quad (II-21)$$

θ_r can be a function of r if it is necessary to make Eqs. (II-20) and (II-21) compatible.

The assumption is made that θ_t changes very little with $|R|$ over distances of length of the order of θ_r . Under this assumption, the decay of p_{\max} with $|R|$ will follow the same law as the decay of $p(r)$ (where $r = |R| - C$ and where C is a constant distance of the order of magnitude of θ_r) with R . That is, since for a given weight of some explosive,

$$\frac{p_{\max}(|R|_1)}{p_{\max}(|R|_2)} = \left(\frac{|R|_2}{|R|_1} \right)^\alpha, \quad (II-22)$$

where $\alpha \sim 1$ is a function of the kind of explosive, then

$$\frac{p_{p.E.}(t)}{p_{O.D.}(r)} = \left(\frac{r}{|R|} \right)^\alpha, \quad (II-23)$$

where the relation $|R| - r = ct$ exists, in which c is assumed to be a constant, ca. 0.0645 in./usec, for the pressures studied.

Elimination of $p_{p.E.}(t)$ and $p_{O.D.}(r)$ among Eqs. (II-20), (II-21) and (II-22) and rearranging leads to

$$\theta_t = \frac{1}{c} \left[\frac{1}{\frac{1}{\theta_r} + \frac{1}{|R| - r} \ln \frac{|R|}{r}} \right] \quad (II-24)$$

The value of r in $p_{O.D.}(r)$ is taken for a given point which resulted in a given θ_r as $r = D_r$ for that point. The value of α is obtained from piezoelectric measurements at various values of $|R|$ and W (weight of explosive), that is, from a peak-pressure similarity curve for a given explosive. It can be taken as unity with little resulting error in θ_t . It is found by solving Eq. (II-23) for θ_r that the dependence of θ_r on r for a given θ_t is not great.

An alternative method of deriving an equation to convert θ_r into θ_t which is in essential numerical agreement with Eq. (II-24) has been suggested by Professor J. G. Kirkwood. Here θ_r and θ_t are defined only at the shock front as

$$\frac{1}{\theta_r} = \left(\frac{\partial \log p}{\partial r} \right)_t \quad \text{for } r = |R| \quad (II-25)$$

and

$$\frac{1}{\theta_t} = - \left(\frac{\partial \log p}{\partial t} \right)_r \quad \text{for } r = |R| \text{ at } t = 0. \quad (II-26)$$

If the logarithmic peak pressure vs. distance curve has a derivative $\frac{d \log p_{\max}}{d R}$, then, exactly,

$$\frac{d \log p_{\max}}{d |R|} = \left[\left(\frac{\partial \log p}{\partial r} \right)_t \right]_{r=|R|} + \frac{1}{c} \left[\left(\frac{\partial \log p}{\partial t} \right)_r \right]_{r=|R|} \quad (II-27)$$

where c is the shock-front velocity at peak pressure p_{\max} . By using Eqs. (II-25) and (II-26) and rearranging, Eq. (II-27) becomes

$$\theta_t = \frac{1}{c} \frac{1}{\frac{1}{\theta_r} - \frac{1}{d \log p_{\max}}} \quad (II-28)$$

For a given weight of explosive,

$$p_{\max} = \frac{P}{|R|^\alpha} \quad (II-29)$$

where P is a constant depending on the weight and kind of explosive. Then,

$$\frac{d \log P_{\max}}{d |R|} = - \frac{\alpha}{R} \quad (II-30)$$

and thus,

$$\theta_t = \frac{1}{c} \frac{1}{\frac{1}{\theta_t} + \frac{\alpha}{|R|}} \quad (II-31)$$

This latter treatment is a more direct approach, but in neither case is the variation of θ_t with $|R|$ stated. This is not an important factor however. Eqs. (II-24) and (II-31) are very nearly equivalent numerically, and in the applications Eq. (II-24) will be used.

(d) Possible Errors. The most apparent source of error in this method of measuring peak pressure and time constant is the possibility of mechanical distortion of the lucite grid by the impact of the shock wave. Preliminary measurements on the velocity of sound in lucite indicate a value of approximately 6.0 ft./msec. Thus the shock wave started at the center of the edge of the lucite grid travels faster in the lucite than the shock wave in the water, and the possibility for mechanical distortion of the lucite grid at the time of the photograph is increased.

Measurements on the photographs of the two shots reported in Sec. III, 3, indicate that such mechanical distortion as well as lens distortion is very small, however. If the grid lines ahead of the shock are extended far behind the shock front, they coincide within drawing errors, with the apparent position of the grid lines in this region of "zero" optical distortion. Since the "direction" of the displacement due to optical distortion is the same as that due to mechanical distortion, that is, away from the charge, this result indicates a very small mechanical distortion. Also the fact that the edge of the lucite grid towards the charge appears as a straight line in the shot photographs indicates no mechanical distortion of the lucite grid in the interval between the time of impact of the edge of the grid and the time of the photograph. It should be mentioned that the curved contour at the left of the grid photograph (Fig. 107) is not the edge of the grid, but rather the edge of a paper diffusion screen behind the grid. The edge of the grid is the line in which the diagonal grid lines terminate. Although there may be some slight curvature to this line in the photograph published, the line on the original print from which this print was made is as close to a straight line as is measurable. Thus mechanical or lens distortion is felt to have little effect on the results obtained by the optical-distortion method.

Another source of error is in using the index of refraction-pressure coefficient measured in fresh water for the studies of pressure and time constant in salt water. Preliminary calculations based on the assumption that the difference in the index of refraction between fresh and salt water at high pressure is the same as it would be at zero pressure but at the concentration of salt per unit volume that the water would have at the high pressure have been made. These calculations indicate that the error involved in the assumption that the index of refraction-pressure coefficient is independent of the salinity is of the order of 2.5%. The direction of this error is such as to make the calculated pressure too great. The data necessary for these calculations on the effect of salinity are from a report by E. A. Brodsky and J. M. Scherschewer (Z. Phys. Chem., B, 22, 412 (1933)).

The possibility of error in the assumption that Snell's Law of Refraction holds in a non-homogeneous medium also deserves some consideration. Gans (Ann. d. Phys. 4, 47, 709 (1915)) studies in detail the case of refraction of a linearly-polarized light wave in a non-homogeneous medium by use of the electromagnetic-field equations. He assumes that $n = \sqrt{\epsilon}$, where n is the index of refraction of the medium and ϵ is the dielectric constant. This relation, of course, does not hold for water. He shows that under these assumptions Snell's Law holds over most of the light path, but very near the point of total reflection the ray of light deviates from the path predicted by Snell's Law and undergoes an angular discontinuity, "knick", at the point of total reflection. A short distance beyond the point of total reflection, the path again coincides with the path predicted by Snell's Law.

It is felt that this deviation from Snell's Law is not important for the case of non-polarized light in water. However, in order to make a quantitative statement as to the amount of possible error, a further analysis would have to be made.

An experimental argument for the assumption that this deviation from Snell's Law is not important for the case of the shock-wave study in water is that, in several calculations of the time constant based on rays of light which are observed to strike the lucite grid at varying distances from the point of total reflection, no systematic trend can be detected with the distance of the point of observation from the point of total reflection.

(e) Sample calculation of time-constant. --- As an example of the time-constant calculation, the data for Point 22, Film 536 (Fig. 111) will be developed.

The first step is to obtain n as a function of ψ for a given film. The data necessary for this are given in Table VIII which shows data from film No.'s 536 and 537 for comparison.

Table VIII Constants Necessary for Eq. (II-15)

Kind of Film	Contrast Process Ortho	Contrast Process Ortho
Temperature	21.3° C.	17.1° C.
a	14.94×10^{-6} per atmosphere	15.18×10^{-6} per atmosphere
b	$.001578 \times 10^{-6}$ per atm. ²	$.001578 \times 10^{-6}$ per atm. ²
n_0	1.3435	1.3444
$ R $	15.97 in.	15.99 in.
p_{max}	$17,050 \text{ lb/in}^2 = 1,160 \text{ atm.}$	$17,050 \text{ lb/in}^2 = 1,160 \text{ atm}$

When the proper values of n_0 , a, b, and p_{max} from Table VIII for Film 536 are substituted in Eq. (II-15) it becomes

$$n = 1.3435 + .0173284 e^{-\frac{(1-x)}{\psi}} - .00212286 e^{-2 \frac{(1-x)}{\psi}} \quad (\text{II-32})$$

where

$$x = \frac{r}{|R|} \quad \text{and} \quad \psi = \frac{\theta_r}{|R|}$$

since throughout all calculations, measurements in units of $|R|$ were used.

Then, since for any pair of intersections,

$$\frac{\sin i_0}{\sin \theta} = \frac{n_0}{n_R}$$

from Eq. (II-16) $n_R \sin i_0 = n_0 \sin \theta$. The value of n_0 is known for a given film (Table VIII) and $\sin \theta$ was found for each point in the calculation for p_{av} . Thus, for Film 536, Pt. 22, $n_R \sin i_0 = n_0 \sin \theta = (1.3435)(.93154) = 1.25152$.

Substituting for n and for $n_R \sin i_0$ the values obtained in the preceding paragraphs, one obtains the differential equation of the path of the ray of light considered at point 22,

$$d\phi = \frac{1.25124}{\sqrt{x^2 \left[1.3435 - 0.0173284x - 0.00212286 \right] - (1.25124)^2}} \frac{dx}{x} \quad (II-33)$$

This equation is then integrated numerically by use of Gregory's formula (see e.g. the Mathematics of Physics and Chemistry by Margenau and Murphy, D. van Nostrand Co., 1943, p. 459) from

$$x = 1 \text{ to } x = \frac{r' - D_r}{|R|} = 0.92429$$

(for the point) for several values of ψ greater than

$$\frac{r_{\min}}{|R|} = 0.1835.$$

The results of these integrations are given in Table IX.

Table IX Results of Integration for ϕ as a Function of Value of ψ as Obtained in Calculation for ϕ_g is 0.4078 Radians (Point 22, Film 536).

ψ	ϕ (radians)
0.184	0.3813
.195	.3671
.230	.3528

The data in this table indicate that there is no value of ψ that will give a value of ϕ as great as ϕ_g . Thus, it is assumed that the ray of light considered for this point has gone through the point of total reflection after leaving the diffuse source of light, the lucite grid. For each of the three values of ψ , then, the value of r_{\min} was calculated (Eq. (II-18)), and the numerical integration of Eq. (II-33) was carried out in two steps, first, from $x = 1$ up to $x = \frac{r_{\min}}{|R|} + \epsilon$ and then up to $x = 0.92429$. The results of these integrations beyond the point of total reflection are given as a function of ψ in Table X.

Table X Results of Integration for ϕ Beyond Point of Total Reflection. Value of ϕ_g as Obtained in Calculation for ϕ_g is 0.4078 radians (Point 22, Film 536).

ψ	ϕ (radians)
0.184	0.3907
.195	.4061
.230	.4232

A plot of these results is given in Fig. 135, from which the value of ψ to give a $\phi = \phi_g = 0.4078$ radian is found to be 0.197.

Since the value of $|R|$ for this shot, Film 536, was 15.97 in., θ_r is obtained as $0.197 \times 15.97 = 3.15$ in.

To convert this to a value of θ_t , use is made of Eq. (II-24), where c is taken as 0.0645 in./ μ sec., α is taken as 1.23, $|R|$ is taken as 15.97 in., and r is the value of $r' - D_r$ for Point 22, Film 536 ($= 0.92429 \times 15.97 = 14.76$ in.). This leads to a value of $\theta_t = 39.1 \mu$ sec.

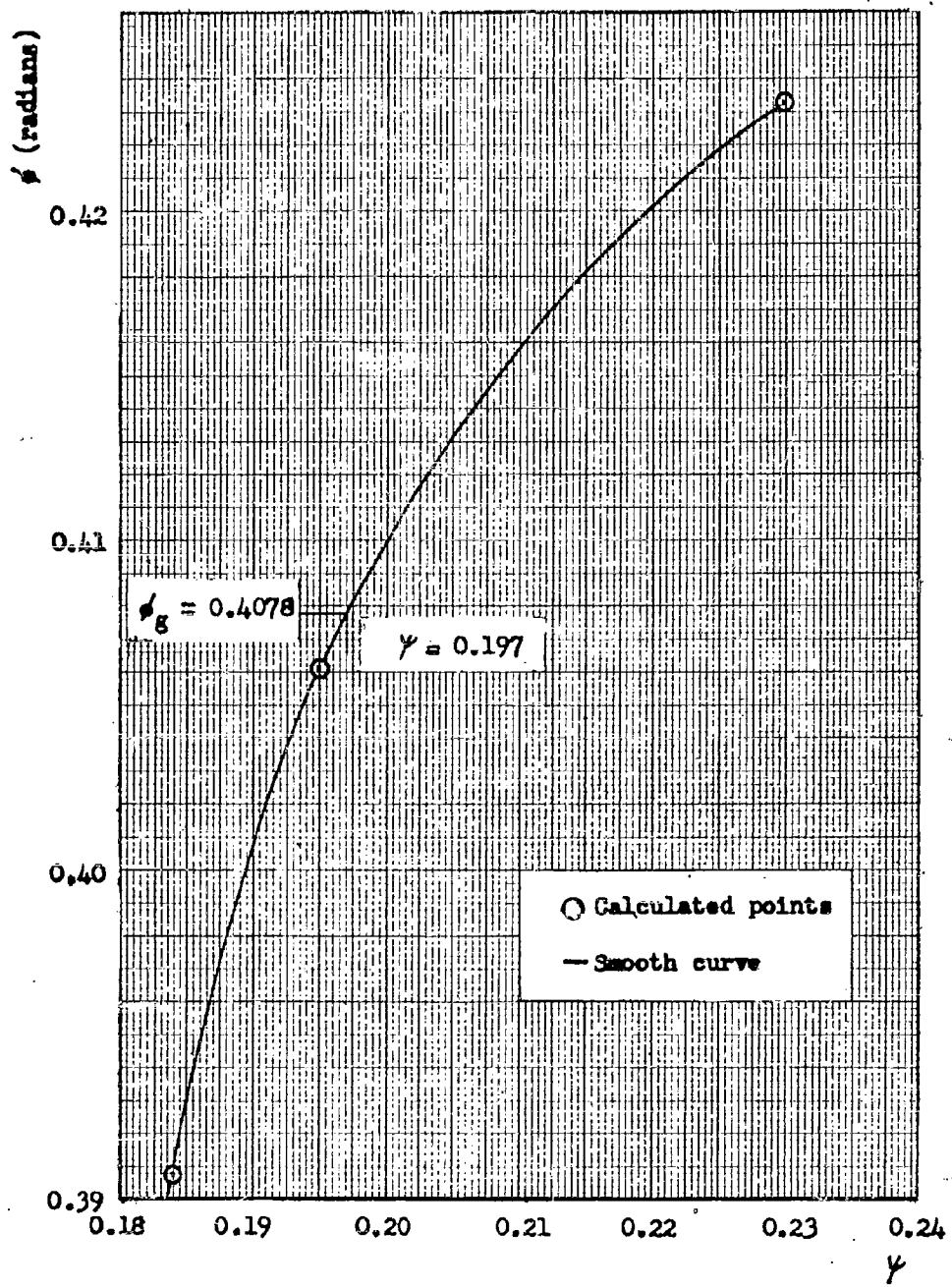


Fig. 135. ϕ vs. γ obtained by integration beyond the point of total reflection. ($\phi_g = 0.4078$ radians, point 22, film 536)

Table XI Results in the evaluation of time constant

Film No.	Point No.	$ R - r_{av}$ (in.)	θ_r (in.)	$r' - R_r$ (in.)	θ_t (μ sec)
536	22	0.61	3.15	14.76	39.1
537	5a	0.63	3.39	14.72	41.3
537	12	0.94	3.23	14.11	39.6
536	8	0.97	3.68	14.03	43.8
537	18	1.13	3.09	13.71	38.1

Av. $\theta_t = 40.4 \mu$ sec, average deviation from mean = $\pm 1.7 \mu$ sec.

It will be noted that there is no systematic trend of θ_t with distance of the point selected for calculation behind the shock front ($|R| - r_{av}$).

2. Grid in same plane with charge; charge directly in front of camera; spherical shock wave

If the experimental set-up is such that the plane of the grid is perpendicular to the optical axis of the camera with the center of the charge at this point of intersection, then the peak pressure of the shock wave may be calculated as follows: Referring to Fig. 136, C is the position of the camera; S is the shock wave; Q is the charge; CG is the grid (perpendicular to the plane of the paper); R is the point at which the given light ray passes through the shock front; r and r' are the true and apparent points of intersection of a pair of grid lines, respectively. A construction line is drawn from Q perpendicular to Rr' . As in Sec. 1, (a), the assumption is made that the pressure from R to r is constant. ν is the ratio of the index of refraction over this range to the index of refraction outside the shock wave.

The quantities β , δ , θ , Rr' , Rr , S , and δ are successively determined by the following equations:

$$\tan \beta = \frac{Or'}{CQ} \quad (II-34)$$

$$Or \cos (\delta - \beta) = Or' \cos \beta \quad (II-35)$$

$$\theta = 180^\circ - (90^\circ + \delta - \beta) = 90^\circ - \delta + \beta \quad (II-36)$$

By the law of sines,

$$\frac{\sin \delta}{Rr'} = \frac{\sin (90^\circ - \beta)}{Or} \quad (II-37)$$

By the law of cosines,

$$Rr = \sqrt{(Rr')^2 + (rr')^2 - 2(Rr)(rr') \cos (90^\circ - \beta)} \quad (II-38)$$

Again by the law of sines,

$$\frac{\sin \delta}{rr'} = \frac{\sin (90^\circ - \beta)}{Rr} \quad (II-39)$$

By Snell's law,

$$\nu = \frac{\sin \theta}{\sin \theta'} = \frac{\sin \theta}{\sin (\theta - \delta)} \quad (II-40)$$

The corresponding pressure is then obtained from Table X. After calculations have been made for several grid line intersections, the peak pressure is determined by the method described in Section 1 of Appendix II; namely, by plotting the calculated pressures against corresponding distances of the mid-point of Rr from the shock front, and extrapolating to zero distance from the shock front.

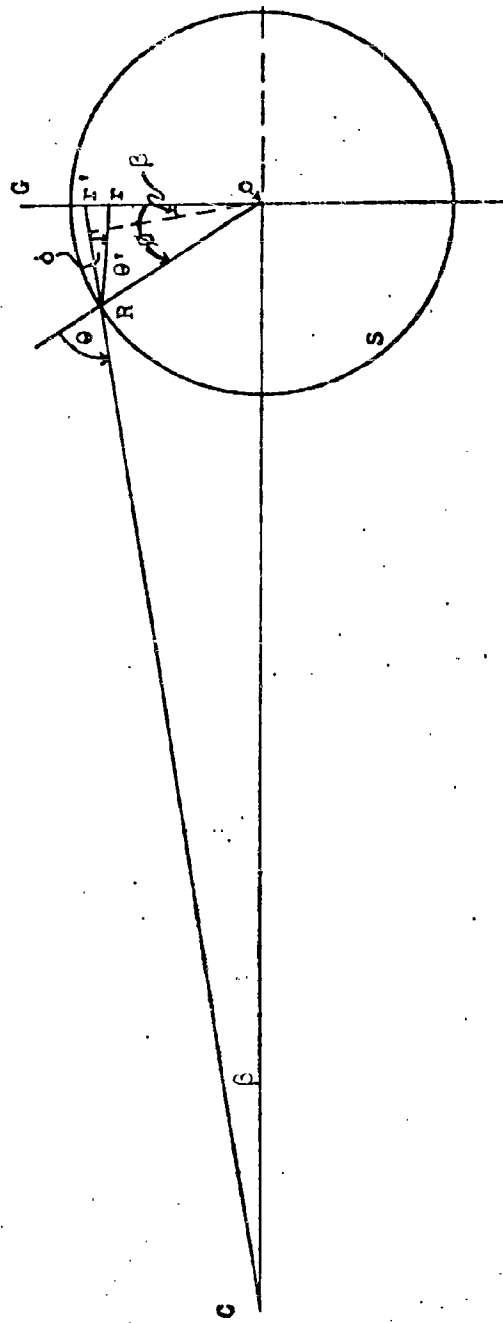


FIG. 136. Second experimental arrangement for determination of peak pressure by optical distortion.

It is to be noted that the shock wave photograph in this case probably does not show the intersection of the shock wave and the grid plane, but rather the intersection of the grid plane and a cone which has its apex at the camera lens and is tangent to the shock wave sphere. Thus, in determining the shock wave radius from the photograph, a corresponding correction should be applied to the apparent radius.

3. Grid in same plane with charge; charge directly in front of camera; non-spherical shock wave

If the experimental conditions meet the above requirements, the peak pressure of the shock wave may be calculated as follows: Referring to Fig. 137, C is the position of the camera; S is the shock wave; Q is the charge; \overline{CQ} is the grid (perpendicular to the plane of the paper); R is the point at which the given light ray passes through the shock front; r and r' are the true and apparent points of intersection of a pair of grid lines, respectively; \overline{RQ} is the normal to the shock wave surface at R . As in section 1 of this Appendix, the assumption is made that the pressure from R to r is constant. ν is the ratio of the index of refraction over this range to the index of refraction outside the shock wave. Although the shock wave is not assumed spherical, it is assumed that the shock wave surface can be represented by some equation $f(x, y, z) = 0$, the exact form being determined from the photograph of the shock wave.

The solution proceeds according to the methods of analytic geometry. The charge is taken as the origin of the coordinate axes, x , y , z , and the various points in the experimental arrangement are assigned the coordinates given in Fig. 137.

The equation of line \overline{CR} is

$$\frac{x - 0}{x_4 - 0} = \frac{y - y_3}{0 - y_3} = \frac{z - z_3}{0 - z_3}, \quad (\text{II-41})$$

which simplifies to

$$\frac{x}{x_4} = \frac{y - y_3}{y_3} = - \frac{z - z_3}{z_3} \quad (\text{II-41'})$$

These equations are combined with $f(x, y, z) = 0$ to obtain x_1 , y_1 , z_1 . The direction components of \overline{QR} are

$$\frac{\partial f}{\partial x_1}, \frac{\partial f}{\partial y_1}, \frac{\partial f}{\partial z_1}.$$

The direction components of \overline{CR} are

$$x_4, -y_3, -z_3$$

$$\cos \theta_1 = \frac{x_4 \frac{\partial f}{\partial x_1} - y_3 \frac{\partial f}{\partial y_1} - z_3 \frac{\partial f}{\partial z_1}}{(x_4^2 + y_3^2 + z_3^2)^{1/2} \left[\left(\frac{\partial f}{\partial x_1} \right)^2 + \left(\frac{\partial f}{\partial y_1} \right)^2 + \left(\frac{\partial f}{\partial z_1} \right)^2 \right]^{1/2}} \quad (\text{II-42})$$

The equation of line \overline{Rr} is

$$\frac{x - x_1}{0 - x_1} = \frac{y - y_1}{y_5 - y_1} = \frac{z - z_1}{z_5 - z_1}. \quad (\text{II-43})$$

The direction components of this line are

$$-x_1, y_5 - y_1, z_5 - z_1.$$

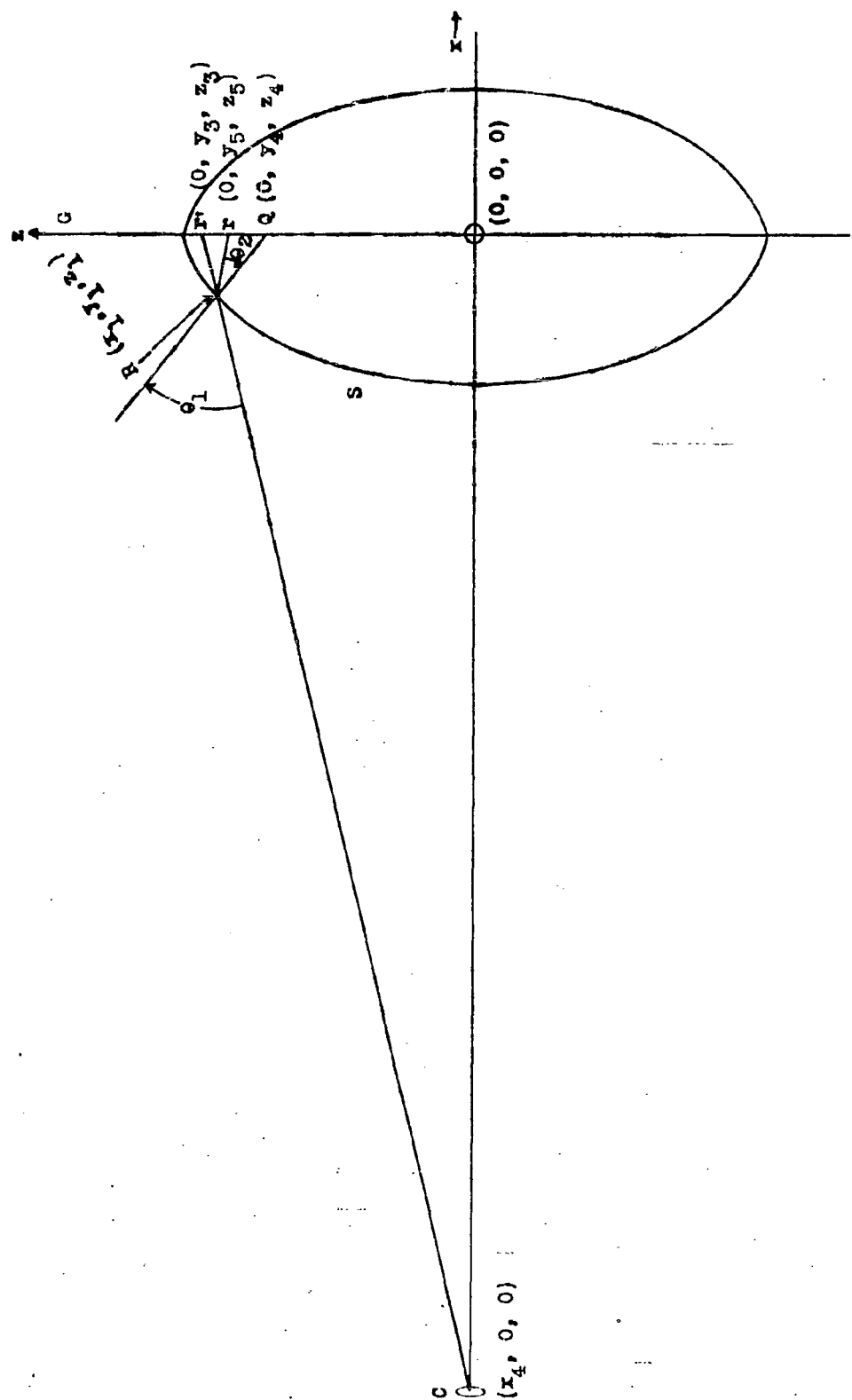


FIG. 137. Third experimental arrangement for determination of peak pressure by optical distortion.

$$\cos \theta_2 = \frac{-x_1 \frac{\partial f}{\partial x_1} + (y_5 - y_1) \frac{\partial f}{\partial y_1} + (z_5 - z_1) \frac{\partial f}{\partial z_1}}{\left[x_1^2 + (y_5 - y_1)^2 + (z_5 - z_1)^2 \right]^{1/2} \left[\frac{\partial f}{\partial x_1}^2 + \frac{\partial f}{\partial y_1}^2 + \frac{\partial f}{\partial z_1}^2 \right]^{1/2}} \quad (II-44)$$

Having values now for θ_1 and θ_2 , by Snell's law,

$$V = \frac{\sin \theta_1}{\sin \theta_2} \quad . \quad (II-45)$$

The corresponding pressure is then obtained from Table VII.

After calculations have been made for several grid line intersections, the peak pressure is determined by the method described in Section 1; namely, by plotting the calculated pressures against corresponding distances of the mid-point of Rr from the shock front, and extrapolating to zero distance from the shock front. Since the shock wave is not spherically symmetric, the other grid line intersections must be chosen in the same general region behind the shock wave to obtain the peak pressure for that region.

Attention is called also to the last paragraph in Section 2 of this Appendix, which is applicable here.

4. Grid behind shock wave; charge directly in front of camera; spherical shock wave

If the experimental set-up meets the above requirements, the peak pressure of the shock wave may be calculated as follows: Referring to Fig. 138, G is the position of the camera; S is the shock wave; Q is the charge; GH is the grid (perpendicular to the plane of the paper); R and Q are the points at which the given light ray passes through the shock front; r and r' are the true and apparent points of intersection of a pair of grid lines, respectively; OR and OQ are the normals to the shock wave surface at R and Q respectively. As in Section 1 of this Appendix, the assumption is made that the pressure from R to Q is constant. V is the ratio of the index of refraction over this range to the index of refraction outside the shock wave.

The solution proceeds according to the methods of analytic geometry. The charge is taken as the origin of the coordinate axes x and y , and the various points in the experimental arrangements are assigned the coordinates given in Fig. 138. Due to the symmetry of the shock wave, the problem becomes planar for any single grid line intersection. x_3 and x_4 are obtained before the shot; and the radius of the shock wave OR , y_3 and y_4 are determined from the photograph.

The two equations

$$x_1^2 + y_1^2 = (OR)^2 \quad (II-46)$$

and

$$\frac{y_1}{x_1 - x_4} = \frac{y_3}{x_3 - x_4} \quad (II-47)$$

are solved simultaneously for x_1 and y_1 , the roots x_2 and y_2 being discarded. Due to the circular symmetry of the shock wave in the $x-y$ plane,

$$\tan \angle rQO = \tan \angle ORC \quad (II-48)$$

If, now, the slope of any line AB is designated λ_{AB} , from Eq. (II-48),

$$\frac{\lambda_{qr} - \lambda_{oq}}{1 + \lambda_{qr} \lambda_{oq}} = \frac{\lambda_{or} - \lambda_{cr}}{1 + \lambda_{or} \lambda_{cr}} \quad (II-49)$$

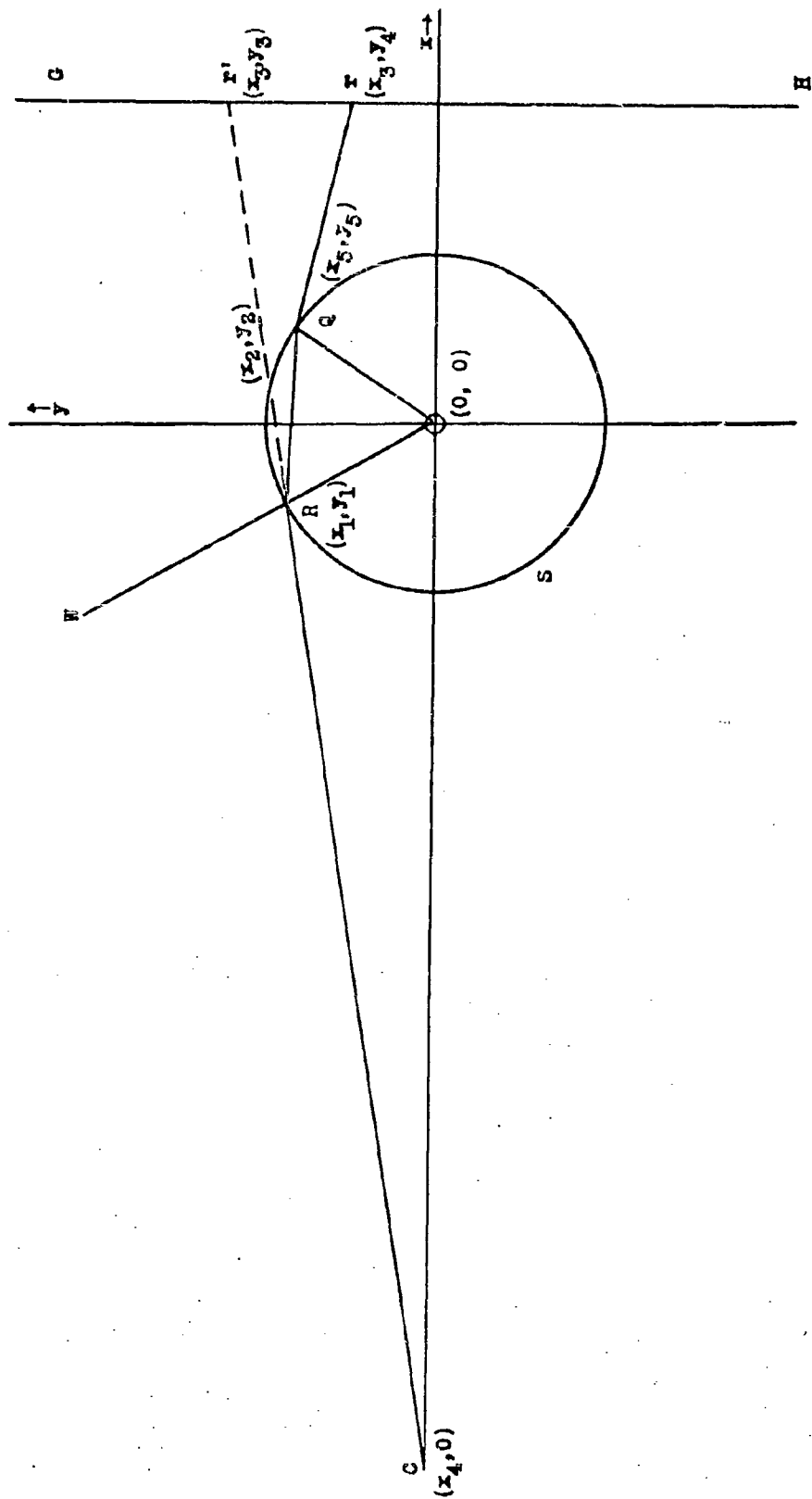


FIG. 138. Fourth experimental arrangement for determination of peak pressure by optical distortion.

But

$$\lambda_{QR} = \frac{y_4 - y_5}{x_3 - x_5} \quad (II-50)$$

$$\lambda_{OR} = \frac{y_1}{x_1} \quad (II-51)$$

$$\lambda_{OQ} = \frac{y_5}{x_5} \quad (II-52)$$

$$\lambda_{CR} = \frac{y_3}{x_3 - x_4} \quad (II-53)$$

Combining Eqs. (II-50), (II-51), (II-52), (II-53) with Eq. (II-49) results in an equation which reduces to

$$\frac{y_4 x_5 - x_5 y_5 - x_3 y_5 + x_5 y_3}{x_3 x_5 - x_5^2 + y_4 y_5 - y_5^2} = \frac{x_3 y_1 - x_4 y_1 - x_1 y_3}{x_1 x_3 - x_1 x_4 + y_1 y_3} = k \quad (II-54)$$

where k is a constant for a given grid line intersection. Eq. (II-54) is combined with

$$x_5^2 + y_5^2 = (OQ)^2 = (OR)^2 \quad (II-55)$$

to obtain values for x_5 and y_5 , the extraneous roots being discarded.

$$\angle WRC = \tan^{-1} \left[\frac{\lambda_{CR} - \lambda_{RO}}{1 + \lambda_{CR} \lambda_{RO}} \right] \quad (II-56)$$

and

$$\angle ORQ = \tan^{-1} \left[\frac{\lambda_{RQ} - \lambda_{RO}}{1 + \lambda_{RQ} \lambda_{RO}} \right] \quad (II-57)$$

Combining

$$\lambda_{RQ} = \frac{y_5 - y_1}{x_5 - x_1} \quad (II-58)$$

and Eqs. (II-50), (II-51), (II-52), (II-53), with Eqs. (II-56) and (II-57) results in the following equations:

$$\angle WRC = \tan^{-1} (-k) \quad (II-59)$$

$$\angle ORQ = \tan^{-1} \left[\frac{x_1 x_5 - x_5 y_1}{x_1 x_5 - x_1^2 + y_1 y_5 - y_1^2} \right] \quad (II-60)$$

Finally,

$$V = \frac{\sin \angle WRC}{\sin \angle ORQ} \quad , \quad (\text{Snell's law}), \quad (II-61)$$

and the corresponding pressure is then obtained from Table VII.

After calculations have been made for several grid line intersections, the peak pressure is determined by the method described in Section 1 of the Appendix; namely by plotting the calculated pressures against corresponding distances of the mid-point of RQ from the shock front, and extrapolating to zero distance from the shock front.

Attention is again called to the fact that the apparent intersection of the shock wave and grid on the photograph is the projection on the grid of a cone with its apex at the camera lens and tangent to the shock wave sphere, and the shock wave radius must be calculated accordingly.

APPENDIX III
CIRCUIT DIAGRAMS OF CAMERA TIMERS

1. Timer for high speed camera 11

Timing of the film speed of the Eastman High Speed Camera Model III is accomplished by photographing periodic light flashes from a small neon bulb synchronized with an oscillator. The bulb is mounted close to the film on the inside of the camera. The timing marks appear along the edge of the film and are photographed simultaneously with the recording of the phenomena under observation. Operating at 3000 frames per second, the maximum speed of the camera, the circuit shown schematically in Fig. 139 produces one mark on the film every third frame. Under these conditions the distance between two adjacent marks can be measured to one tenth of one per cent (i.e. to one μ sec) by the use of an optical comparator.

The circuit was designed to operate from the output of a 1000 cycle per second tuning fork (General Radio Type 813A) although it can be used with other sinusoidal oscillators operating at different frequencies if slight changes are made in some of the circuit constants. The accuracy of the film speed determination depends on the accuracy of the oscillator frequency.

The essential parts of the circuit are a clipper (tubes T_2 and T_3) which converts the input sine wave into a square wave; a counter circuit (T_5 and T_6) which divides the input frequency by two; a short duration pulse generator (T_7 and T_8); a power output tube (T_9) to drive the neon flasher, and a tuning eye (T_1) to indicate the voltage of the sine wave from the oscillator.

The neon bulb operates satisfactorily when cables as long as 1000 ft. are used between the timer and the bulb; this is the greatest length of cable which has been employed. The current in the neon bulb is adjusted by the potentiometer in the cathode circuit of T_9 in order to control the intensity of the bulb; about 5 mamp is used at 1000 cps and 3 mamp at 500 cps.

This circuit can be used with an external power supply operating from a power line and delivering 300-500 volts at 40 mamp, in addition to current for tube heaters, or from a 6-volt storage battery if other power is not available. It is desirable to use a different source of power for operating the circuit than that used for operating the camera because, when the camera starts, a very large surge is introduced which may affect the operation of the electronic circuit, particularly if the power is obtained from a small generator. A Mallory Type VP-552 vibrapack and a filter section are built into the unit for operation from a 6-volt battery and a Mallory Type 107 battery charger is included for charging the storage battery from a power line. The 1000 cps tuning fork, the vibrapack and the battery charger are included in a portable wooden carrying case which houses the electronic circuit.

2. Timer for Jerome camera

Inasmuch as the requirements for the Jerome camera were much less severe than those for the Eastman High Speed Camera because of the lower speed required, a simpler circuit shown in Fig. 140 was used to drive a neon lamp. A 50 cycle, single contact electrical tuning fork excites this unit. The signal from the fork is amplified and sharpened into short duration pulses in the first two stages and then applied to the grid of a Strobotron tube (SN4). The SN4 fires on each pulse, discharging the 4μ f condenser through the transformer in its plate circuit. The output of this transformer drives a 1/4 watt neon bulb mounted in the camera and connected to the timer unit through a cable. The short discharge time of the 4μ f condenser insures short duration light pulses from the neon bulb suitable for dotting the film.

11 This is discussed in more detail by G. K. Fraenkel, Apparatus for the measurement of air burst pressures by means of piezoelectric gages, NDRC No. A-373, OSRD No. 6251, Chapter 9.3.

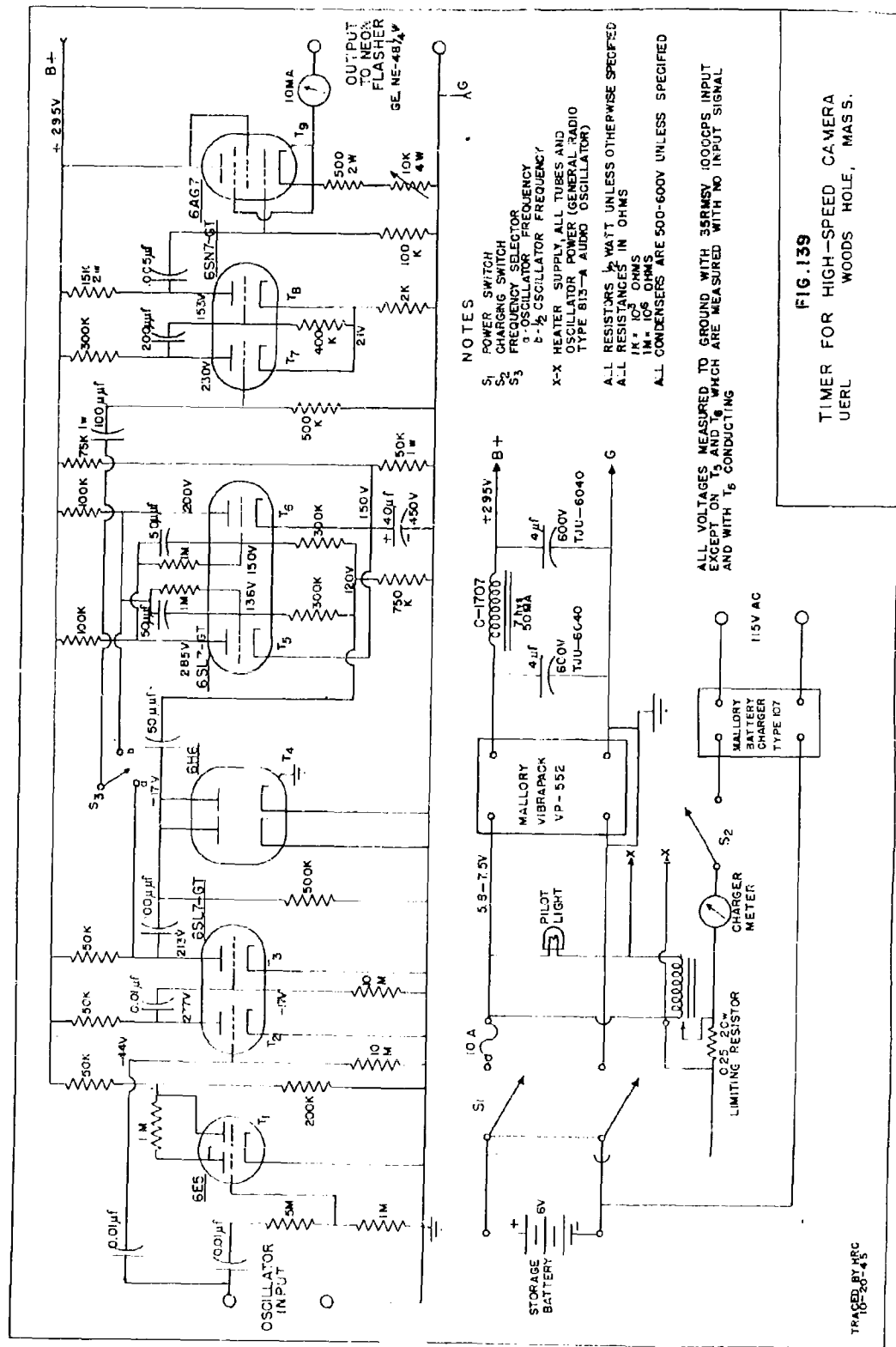
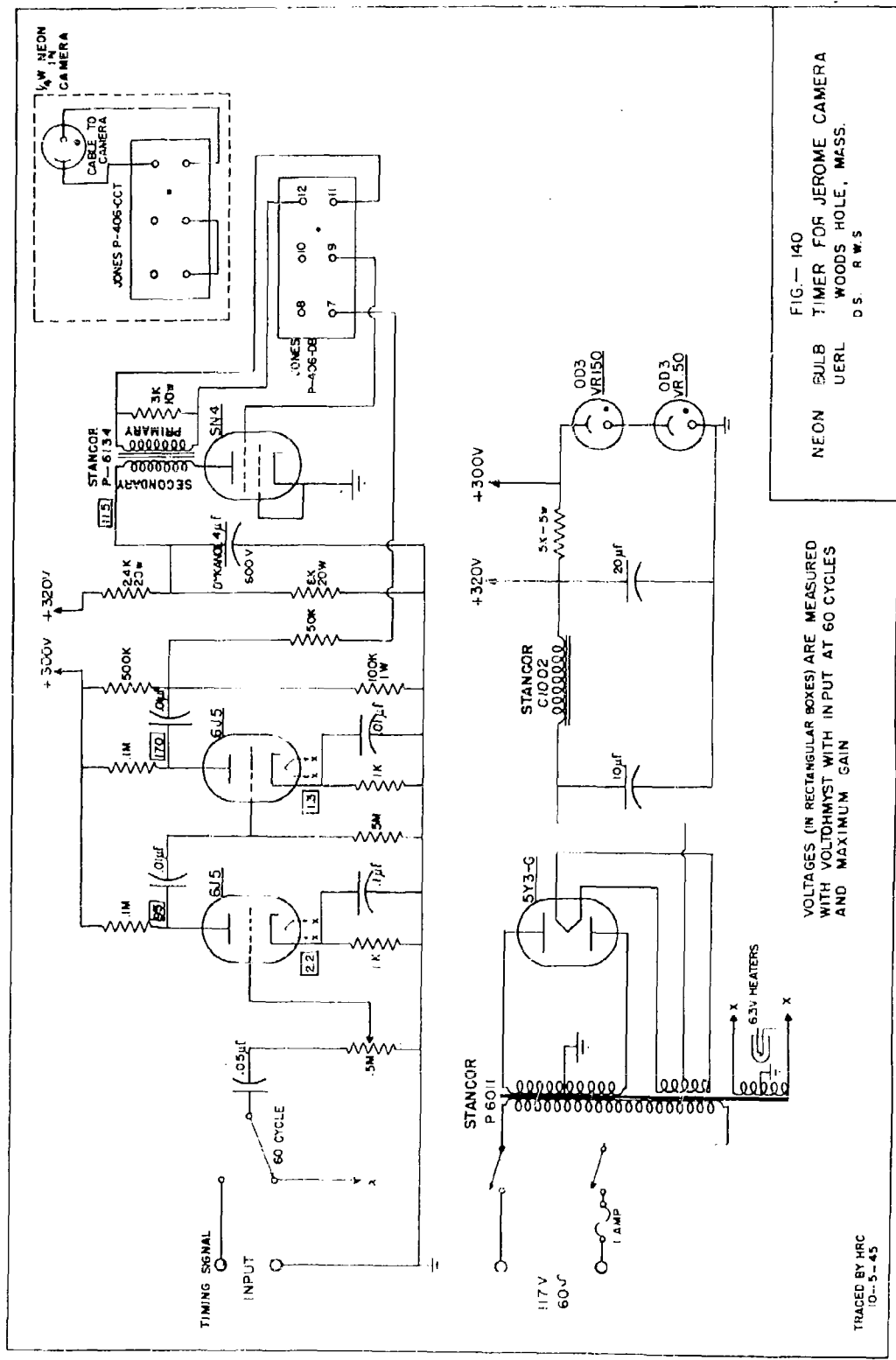


FIG. 139
TIMER FOR HIGH-SPEED CAMERA
UERL WOODS HOLE, MASS.

TRACED BY MRC
10-20-45



VOLTAGES (IN RECTANGULAR BOXES) ARE MEASURED WITH VOLTOHMETERS WITH INPUT AT 60 CYCLES AND MAXIMUM GAIN

TRACED BY HRC
10-5-45

15518

GASKETS AND STUFFING BOXES FOR CAMERA CASES

We have found that gasket and stuffing box design for our camera cases is not very critical. No special effort is made to achieve very close tolerances on gasket surfaces. However, whenever practical we put the gasket in a tongue and groove type of joint. The only gasket failures we have had have been due to static and not dynamic pressure. At a depth of 600 feet, for example, we found that we could not use our ordinary $1/8$ to $1/16$ inch rubber gasket because it squeezed out. Thin Vellumoid was found satisfactory in this instance.

We have used two types of stuffing boxes for electrical leads with equal success. In the first type (see Fig. 141) the wire cable led through a hole in the case which was packed with compressed rubber. In the second type (Fig. 142), an insulated metal jack was put through the case and electrical connections were made on both sides of the jack. The second method is perhaps preferable in deep water because there is no chance of water leaking into the case through a hole in the cable insulation.

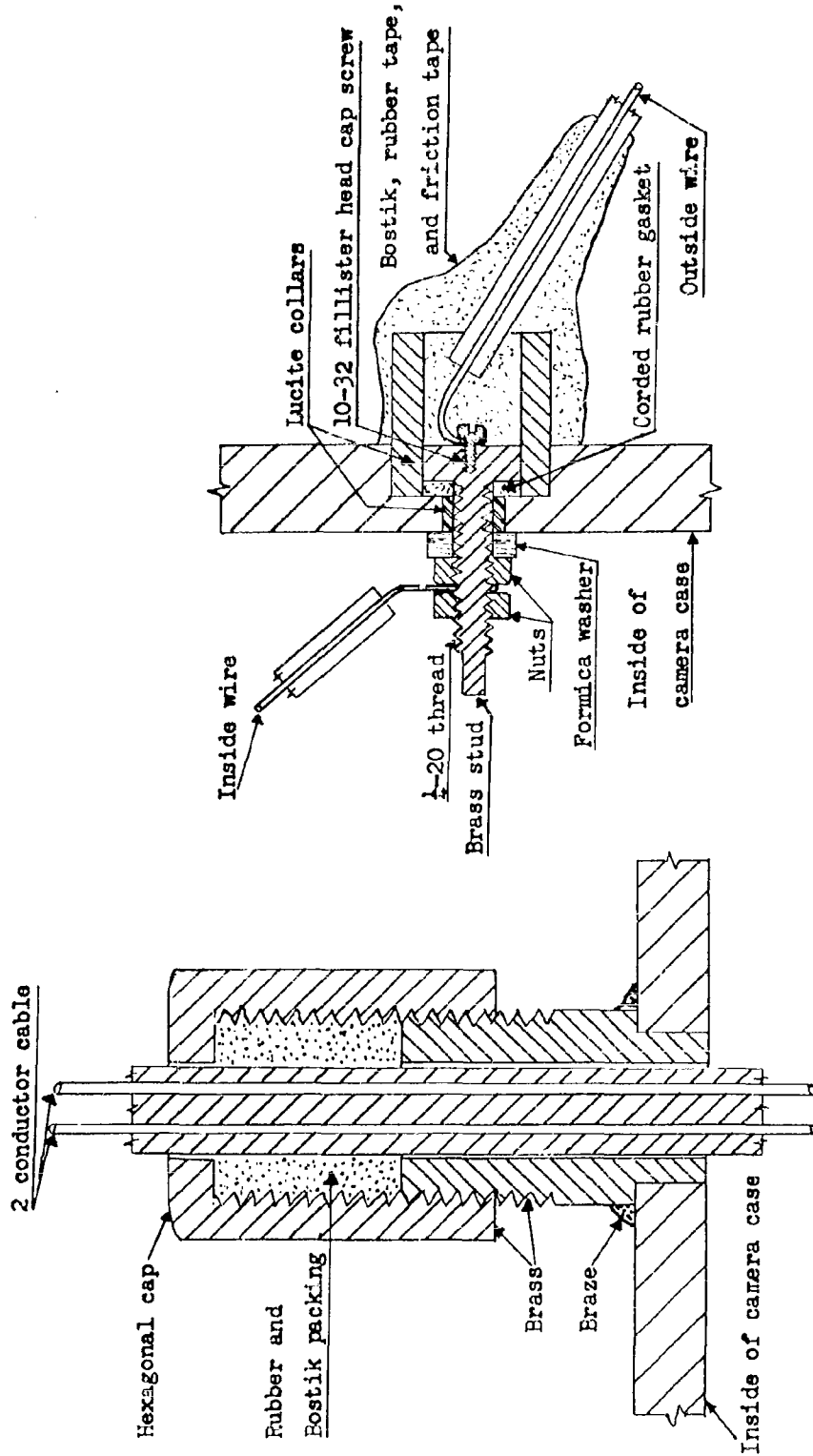


Fig. 141. Stuffing box for electric cable.

Fig. 142. Single wire lead-in connector.

Copy Number

TO

1 Office of the Executive Secretary, OSRD
Attn: Project Control Section
1424 - 16th Street, N.W.
Washington 25, D. C.

2 Division 2 Files, NDRC
Attn: Miss Lola Jaques
1424 - 16th Street, N. W.
Washington, 25, D.C.

3 & 4 Joint Research & Development Board Library
Attn: Miss Constance Rorke
Library of Congress Annex
Washington 25, D. C.

5 thru 17 British Commonwealth Scientific Office
1785 Massachusetts Avenue, N.W.
Washington, D.C.

18 & 19 Division 2, Library
Underwater Explosives Research Laboratory
Woods Hole Oceanographic Institution
Woods Hole, Massachusetts

20 Navy, Bureau of Aeronautics Contractor,
New York University, Applied Mathematics Group
Attn: Dr. R. Courant
New York, New York

(Send carbon copy of receipt to:
Head of Mathematical Section, ONR
ONR Planning Division, Navy Dept.
Washington, D.C.)

21 & 22 Col. E. A. Routheau
War Department Liaison Office w/NDRC
Research & Development Division
War Department General Staff
Room 4E-841, The Pentagon
Washington 25, D.C.

(One copy for distribution to:
M. F. Roy, P.O. Box 1663
Santa Fe, New Mexico)

23 thru 28 Army Air Forces Liaison Officer for NDRC
Attn: Brig. Gen. Alden R. Crawford
Washington 25, D.C.

(For distribution to:
Scientific Advisory Group (1 copy)
Operational Research Section, Continental Air Forces,
Bolling Field (1 copy)
President AAF Board, Orlando, Fla. (2 copies)
AAF School Library-Req. 265, AAF Center, Orlando, Fla. (1 copy)
Air Ordnance Officer, AAF (1 copy)

DISTRIBUTION LIST (continued)

**This Document
Reproduced From
Best Available Copy**

Copy Number

TO

29 thru 36

Ordnance Department Liaison Officer for NDRG
Attn: Col. G.F. Powell
Washington 25, D.C.

(For distribution to:

Col. G.F. Powell (2 copies)
L. R. Littleton, Ammunition Development Division (1 copy)
Ballistic Research Laboratory, Aberdeen Proving Ground (2 copies)
Ordnance Research and Development Center, Aberdeen Proving
Ground (1 copy)
Office of the Ordnance Officer, U.S. Military Academy (2 copies)

37 thru 77

Office of the Chief of Naval Research
ONR Planning Division
EXOS, Navy Department
Washington 25, D.C.

(For distribution to:

Research and Development Division (3 copies)
Research and Development Division, Bureau of Ordnance (2 copies)
Research and Development Division, Ammunition and Explosives
Sec., HES, Bureau of Ordnance (10 copies)
Technical Library, Adlf-2, Bureau of Ordnance (1 copy)
Bureau of Ships (Code 014K) (2 copies)
Capt. L. V. Honsinger, Bureau of Ships (1 copy)
Comdr. J. M. Fluke, Bureau of Ships (1 copy)
Comdr. C. H. Gerlach, Bureau of Ships (1 copy)
Bureau of Ships (Code 5815) (3 copies)
P.M. Morse, Op-34-H-2 (CNO) OEG, Room 4311 (1 copy)
David Taylor Model Basin (3 copies)
Mr. W. J. Sette, DTMB (1 copy)
Submarine Mine Depot, Fort Monroe, Va. (1 copy)
Lt. N. H. Bullard, U.S. Naval Mine Depot, Yorktown, Va. (1 copy)
U.S. Naval Ordnance Laboratory (1 copy)
D. P. MacDougall, U.S. Naval Ordnance Laboratory, Research
Division (3 copies)
U.S. Naval Ordnance Test Station, Inyokern, Calif. (1 copy)
Head of Dept. of Ordnance and Gunnery, U.S. Naval Academy (1 copy)
Commandant, Portsmouth Navy Yard, Attn: Preliminary Design
Branch (1 copy)
Bureau of Construction and Repair, Navy Department (1 copy)

78

U.S. Naval Research Laboratory
Attn: Dr. Ross Gunn
Washington 20, D.C.

79

Prof. Walker Bleakney, Princeton University, Princeton, New Jersey

80

Prof. C. O'D. Iselin,
Underwater Explosives Research Laboratory,
Woods Hole Oceanographic Institution, Woods Hole, Massachusetts

81

Explosives Research Laboratory, Attn: Mr. John C. Holtz
Bruceton, Pennsylvania

Any surplus copies should be sent to:

Library of Congress
Acquisitions Department
OSRD Project
Washington 25, D.C.